2013

Progress toward a model based approach to the robust design of welded structures

Eric Johnson
Iowa State University

Progress toward a model based approach to the robust design of welded structures

by

Eric M. Johnson

A dissertation submitted to the graduate faculty

in partial fulfillment of the requirements for the degree of

DOCTOR OF PHILOSOPHY

Major: Materials Science and Engineering

Program of Study Committee:
Scott Chumbley, Major Professor
Alan Russell
Ralph Napolitano
Frank Peters
Pal Molian

Iowa State University

Ames, Iowa

2013

TABLE OF CONTENTS

ABSTRACT

Civilization has relied on welded structures to facilitate fabrication and improve our quality of living for the past century. Welds are used in our production of energy, to create infrastructure that we rely upon such as bridges and building, and to fabricate the equipment that makes all of this happen. In short, the joining of two metals through welding has contributed immensely to our society.

One problem that has plagued welds is their susceptibility to fatigue failure due to cyclic loading. Fatigue in welded joints is a complicated phenomenon and the subject of fatigue of welded structures been the subject of great study. The goal of the research presented in this dissertation is to improve fatigue life prediction capability by incorporating the effect of the welding process prior to making the structure.

The first area examined in this study is the residual stress that is induced during the welding process. If the goal of virtual design and verification of welded structures is to become a reality the residual stress state needs to be known prior to making a product. Computational welding simulation can be used to predict the residual stress state of the welded structure prior to the manufacturing of any part. In order to use computational welding simulation in fatigue life predictions the validity of the results need to be confirmed. This was done in the following dissertation work in two steps, initially by using 3D image correlation to measure the full field displacement of a structure as compared to simulation, and secondly by using neutron diffraction to measure the residual stress after welding as compared to the computational welding simulation results. The results showed that the residual stress state could be predicted with enough accuracy to be used in fatigue life predictions.

It is known that the residual stresses redistribute during cyclic loading which can have an impact on their effect on the fatigue life of the structure. The third area this dissertation looks at is the redistribution of the residual stresses during cyclic loading, where residual stress is measured as a function of cycles, again using neutron diffraction. This analysis provides an understanding of how much of an effect the residual stress redistribution has on the residual stress state during the majority of the cycles experienced by a part undergoing cyclic loading.

The last section combines the results of these earlier studies to suggest a methodology to predict the distribution of the fatigue life for welded structures that accounts for the welding manufacturing process. This is achieved by accounting for distribution of the local geometry, the residual stress present, and the material properties. By using a Monte Carlo simulation a predicted distribution for fatigue life is obtained, which is then then compared to experimental fatigue test data to test the validity of the proposed methodology.

CHAPTER 1: INTRODUCTION

In recent years increasing demands to reduce design cycle times while decreasing development costs have driven the use of computer-based simulation tools. In product development these tools find two distinct applications: during the design / development phase and during the manufacturing phase.

One critical aspect of the design phase is to evaluate the potential durability of a proposed design. To identify potential durability problems in any design, four things are needed: knowledge of the material properties, the expected loads during use, the final part geometry that results from the design and manufacturing processes and the residual stress state of the part. Manufacturing processes such as stamping, casting, heat treating, welding, forming, machining, rolling etc., all induce changes in mechanical properties and introduce residual stresses. In any lifetime prediction model a firm knowledge of the mechanical properties and residual stresses present must be known if one is to predict the durability of structures.

When performing *critical to quality* activities in the Six Sigma process for durability analysis, the effects of manufacturing processes have a significant impact on the mean and distribution of the fatigue life of the product (1). Currently, design and manufacturing analyses using computer simulation models are conducted separately, so the effects of the manufacturing process are overlooked in the durability analysis of a structure during the design process. The distribution of the input variables also are not accounted for and, thus, the distribution of expected lives are not understood. This lapse, if not corrected, will always produce errors that drive costs upward and increase cycle time when it comes to design, fabrication and implementation of a new part.

When predicting product durability and life, welded structures are among the most troublesome of manufacturing processes. This is because the nature of the process itself introduces a wide range of factors that must be considered. Welding is a process that joins two materials together through melting, heating and applying pressure, or the combination of the two. During the process material properties change substantially, a new geometry is formed and residual stresses are introduced. Thus, a methodology that can successfully account for all variations in a complex welding process would be of tremendous benefit in the design / development stage, preventing problems that presently are only discovered during the time consuming and expensive pre-production physical testing of the proposed design. Such a methodology should be equally applicable to other manufacturing processes, which contain fewer variables.

Advancing the knowledge of the role the manufacturing processes play in the durability of components will result in optimization of the manufacturing processes during design, and should allow parts to reach their full potential for durability. Optimized designs and manufacturing in turn will result in lower material and energy costs due to use of thinner and lighter materials. Ideally, the desired goal is an all-encompassing model that accounts for the variation of input parameters such as part geometry, applied stress, residual stress, material properties, etc. and then predicts the reliability of the assembled structure based on these parameters. In practice, this would involve a consideration of all the processes that have been used to assemble the final structure, i.e. cast parts welded to rolled parts, bolted to supports which themselves are welded structures, etc. Clearly, this is an extremely complex question consisting of many different distinct parts where specific knowledge is required.

1.1 Problem statement

The Fatigue Design and Evaluation Sub-Committee of the Society of Automotive Engineers have demonstrated that fatigue life predictions have a high amount of variability (2). This is especially true when considering the life of welded structures, where a large amount of variability due to the complexities associated with the process is inherent. This investigation will look at how manufacturing process effects can be incorporated into fatigue life analysis, with a particular focus on welding. Since the fatigue life of a design has so much variability, a prediction method that accounts for this variability will be in the central goal of this dissertation. Specifically, this dissertation will answer the following questions:

1. Can welding simulation provide enough accuracy in residual stress predictions to be used to replace measurement of residual stresses in fatigue life predictions of welded structures?
2. Does cyclic loading change the residual stress state and negate the initial residual stresses used in fatigue life predictions?
3. Can the distribution of fatigue life be predicted by accounting for the variability of the input parameters like residual stress, material strength, local weld toe geometry, and material properties?

These three questions constitute the main objectives of this research.

This dissertation is organized in the following manner. Chapter 2 will provide the background information on fatigue life prediction methods in general and in particular as related to welded structures, residual stresses and their measurement, and welding process simulation. Chapter 3 will describe the experimental procedure used in this work. Chapters 4 through 7 will answer the expressed questions. To begin, the answer to Question 1, “Can welding simulation provide

enough accuracy ….” will be addressed in two parts. In Chapter 4 the distortion on a T-weld sample will be used as a first validation of welding simulation software since the distortion is related to residual stress and is much easier to measure. A novel approach using 3D image correlation to measure the distortion during the welding process and the comparison of the distortion measurement to weld simulation will be presented using in Chapter 4. Chapter 5 will then compare residual stress predictions to experimental residual stress measurements from neutron diffraction. The residual stress state that is present during operation is the residual stresses that will impact the fatigue life. Question 2, “Does cyclic loading change the residual stress state…” is addressed in Chapter 6, which contains an evaluation of the redistribution of the residual stress as a function of cyclic loading by measuring the residual stress with neutron diffraction in a weldment after it has been cycled. Finally, Question 3, “Can the distribution of fatigue life be predicted…” is dealt with in Chapter 7, where a methodology to predict the variation in fatigue life by incorporating the statistical distribution of the input parameters is discussed. A validation of the technique to predict the variation will be presented by comparing the fatigue life distribution of tested samples to the predicted fatigue life distribution. Chapters 4-7 will be presented as distinct papers, each containing its own experimental procedure specific to the chapter, discussion, and conclusions. A general summary and conclusion of the entire dissertation will be given in Chapter 8.

CHAPTER 2: BACKGROUND AND LITERATURE REVIEW

2.1 Welding

Background:

The first welding technique that was used for ferrous materials was “forge welding” which has done by blacksmiths for thousands of years. In modern times the industrial revolution of the 1800s started the advance of welding technology. In the 1880s electric arc and acetylene torches were used for some of the first fusion welds, but it was not until the 1920s that welding was fully adopted as a joining process for commercial use. Poor workmanship was common in the early days of the welding industry and the development of training and standards was the key driver in adoption of welding between 1920 and 1940 (3).

From the 1940s to the 1960s welding was being pushed to higher and higher limits. World War II provided a great need for ships to be produced faster at lower cost, so welding was used for the fabrication of the ship hulls. It was not long after these ships went into service that they began to develop cracks in the hulls. Approximately 20% of the 5000 ships that were made using welding methods developed cracks at or near welds in the hulls and main decks. The main causes of these cracks were the low fracture toughness of the steel and poor (or in many cases ignorant) construction techniques which led to high residual stresses in the weld. As the years progressed these issues were addressed through development of better welding techniques and better steels with higher fracture toughness. Industry standards were developed to and adopted to raise the level of the welding industry (4).

Welding technology also was advanced as it came to be used in more rigorous and critical applications, such as in pressure vessels for nuclear power plants, submarines, oil and gas pipelines, and rocket engines for the aerospace industry. These applications needed higher

strength, more corrosion resistance, and lighter weight materials. This pushed the development of welding techniques for the joining of a wider variety of materials, with an increasing demand for fewer defects.

The welding industry today has grown to have a huge effect on the global economy. It has been said that fifty percent of the United States economy is related to welding in one manner or another (3). Virtually every manufacturing industry today uses welding in one form or another, either in the equipment they employ to make their product or to repair the product. Welding has become a key manufacturing technique in producing durable products due to the high speed and low cost of most welding processes, making it an extremely cost effective and efficient process for joining two parts together.

Welding Methods:

A number of welding processes exist that have been developed over the years (3). The welding process that will be studied in this research is Gas Metal Arc Welding (GMAW), which is also called Metal Inert Gas (MIG) Welding. Pulsed GMAW welding is popular in industrial applications because the metal deposition transfer can be controlled by modulation of the current (5).

Gas Metal Arc Welding creates an electric potential between the work piece and the filler metal wire. This potential results in a flow of current, which generates a partially ionized gas that heats the work piece and the filler metal. The filler metal becomes molten and metal is deposited, joining the two parts together (6). A representation of the forces in the welding process is shown in Figure 1.

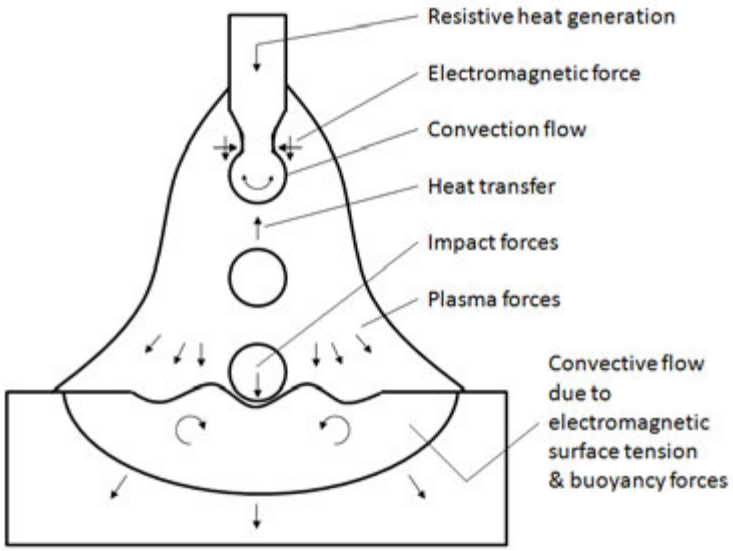

Figure 1) Graphical representation showing the forces in the welding arc (5).

There are four different modes in which the filler metal, in the form of weld wire, is deposited on the work piece, classified by the droplet shape and how the droplet is derived. These are:

Globular transfer is a method whereby a large molten globule of weld wire is formed on the tip of the weld wire. The size of the globule is several times larger than the weld wire itself. When the globule is large enough it is transferred to the surface of the work piece by gravity. Globular transfer is the least desirable due to large amounts of spatter and limited work piece orientation.

Short circuit transfer uses a lower current and smaller wire than the globular transfer method. This produces a smaller weld drop, which produces a short circuit between the weld wire and work piece. The lower heat input inherent in this method usually limits its applicability to the joining of thinner gage materials.

Spray transfer uses higher currents then the short circuit and globular transfer methods. The currents are so high that the weld metal does not form a drop, but vaporizes into a stream. This method reduces the weld splatter and is well suited for aluminum and stainless steel applications.

Pulsed spray transfer is currently the most common method used for GMAW industrial applications. This method pulses the current from a high to low value. On each pulse a droplet is formed and accelerated to the work piece in the plasma flow. The advantages of this method is that the transfer of material is similar to spray transfer, thus the amount of spatter is minimized, while the overall lower average heat input makes it suitable for used on thinner gage materials. The typical pulse duration is between 2 to 50 microseconds. A schematic illustrating the pulsing action is shown below in Figure 2.

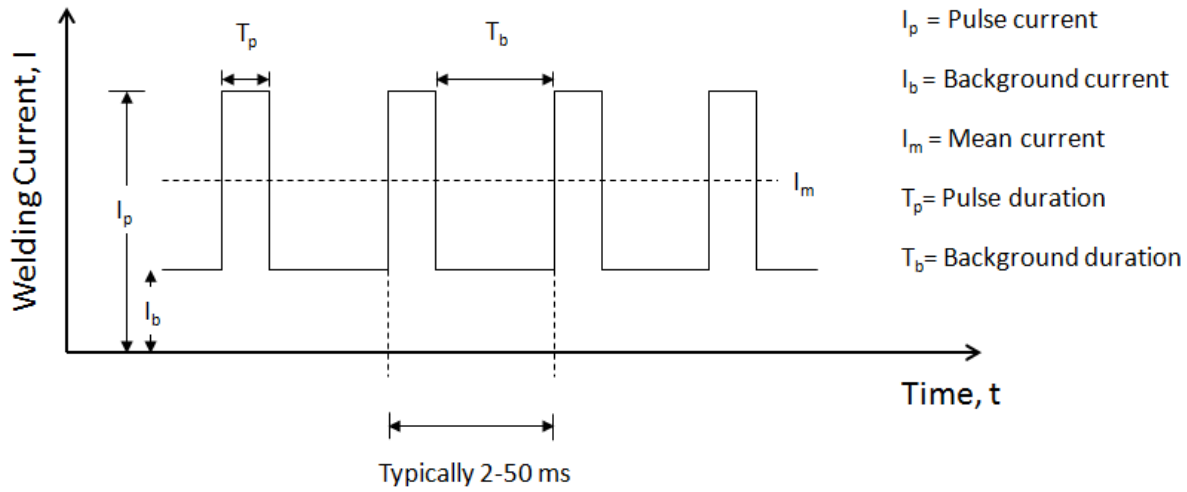

Figure 2) Graphical representation of the wave form for pulsed arc welding (6).

Welding Considerations in Product Design

When designing a product the design engineer sets the global geometry of the part by accounting for the function of the part and then designing the form necessary to carry the loads the structure will be subjected to during use. When the prototype design has been checked to ensure that the component will meet the design requirements for strength and durability the design is turned over to the manufacturing engineers for construction. The manufacturing engineers produce several prototype parts that meet the design and these prototypes are durability tested to ensure that the part does indeed meet the required life expectancy. Many times the component does not pass the durability testing and the part goes back to design to make corrections. The process is repeated until a workable design is finally produced. Once a workable design is decided upon the final step in bringing the component to market involves a consideration of the time and cost of manufacturing. Methods used in making the prototype may be deemed too expensive for production, causing less expensive methods to be substituted. For example, parts machined for the prototype may be cast for production, or of special importance in this dissertation, parts cast for the prototype may be welded.

It should be immediately apparent that this process is unnecessarily costly and time consuming. This methodology neglects the interaction between design and manufacturing and results in a very long time-to-market. Uncertainties associated with the process in general, as well as complications that may arise due to changing from one manufacturing method to another between prototype and production part (e.g. casting for a welding) often results in over-built products due to unnecessarily high design margins. This is particularly true in welding where variables such as exact part geometry and the presence of residual stresses are either unknown or difficult to predict. These unknown variables means that while welding as a production methods

has the potential to significantly reduce costs it often is discarded due to safety concerns. For example, due to durability concerns the use of welds in safety critical applications has been limited in aircraft construction. Similarly, in mature industries like ship building and off-highway construction equipment, while welding has the potential of lowering the weight of the vehicles it often is not used since accurate durability prediction methods are unavailable.

Clearly, methodologies that account for variables in welding during the design stage would be of immense value. Such methodologies would provide the opportunity for optimized designs for both function and manufacturability in the initial stages, eliminating many problems before they ever need arise. As regards welding, a methodology that successfully can predict weld life durability during initial design is of critical importance.

Welds are very susceptible to fatigue failure because they are used in applications where the welds are subjected to cyclic loading, they have a natural discontinuity at the weld toe that is ideal for stress concentration and crack initiation, and the manufacturing process associated with welding is complex, often resulting in residual stresses that can hasten the onset of fatigue. In order to understand clearly the information necessary to accurately predict durability in welds, a brief summary of fatigue failure is in order.

2.2 Fatigue

History of Fatigue

Metal fatigue was first recognized by Albert (7), in 1837 when he was investigating the failure of a metal chain used in a mining application. At that time he performed the first component testing to assess fatigue life. In 1842 Rankine, well known for the Rankine process in thermodynamics (8), made the first observation of fatigue cracks starting at notches that concentrate the stress (9). He suggested that the fillets used in railroad axles by made larger to

prevent failure (10). Coining of the term "fatigue" is credited to Baithwaite, an Englishman, in 1854 (11). He worked on various failures including brewery equipment, water pumps, propeller shafts, crankshafts, railway axles, levers, and cranes.

The next major contribution to the science of fatigue was by August Wohler. Wohler's work started with the first measurement of the service loads on rail road axles between 1858 and 1860 (12). In 1860 he published the results of fatigue testing on railroad axles and in 1870 Wohler presented his final report on the fatigue results of notched and un-notched specimens. In this work he laid the base of the so called Wohler law which he summed up by saying "Material can be induced to fail by many repetitions of stress, all of which are lower than the static strength. The stress amplitudes are decisive for the destruction of the cohesion of the material. The maximum stress is of influence only in so far as the higher it is the lower are the stress amplitude which leads to failure (12)." Here Wohler states that the life is dependent on both the peak stress and the stress amplitude which is the foundation of metal fatigue analysis. Wohler's work is the foundation upon which all other fatigue analysis has been built.

It took until 1936 until Spangenberg took the tablature data that Wohler had published and put it in a graphical format. The resulting curves were known as Wohler curves (12). In 1910, Basquin took the same data and plotted it as log stress vs. log number of cycles axes. The resultant graph could then be described by the simple power function (13).

$$\sigma_a = CR^n \qquad \text{Equation 1}$$

The equation presented by Basquin based on the Wohler data is still used as the basis of the stress life fatigue approach (14).

The next addition to the literature comes from Bauschinger, who described the effect named for him as the "the change of the elastic limit by often repeated stress cycles (12)." Bauschinger's contribution is a key idea in the strain life prediction method developed in the 1950s by Manson and Coffin (15), (16) (17).

In 1920 Griffith developed the ideas on fracture from the energy needed to fracture glass. Griffith's work is the basis of linear elastic fracture mechanics (LEFM) (18). Irwin further used Griffith's work to apply the energy release approach to brittle metals and developed the idea of the stress intensity factor (19). Paris built on Irwin's stress intensity work and applied it to fatigue to predict crack propagation (20).

Other contributions in the area of fatigue include the work of Palmgren and Miner, who contributed the methodology to sum the fatigue damage (21) (22). A method to handle mean stresses during loading for the stress life methodology was developed by Goodman (23), and later mean stress corrections for the strain life methodology were proposed by Smith, Watson and Topper, Morrow and Manson and Halford (24) (25) (26).

One thing that is clear from the historical literature is that fatigue research has been driven by high profile failures and common technical challenges, from the early work that was driven by the train crash on October 5th, 1842 near Versailles France that claimed the lives of 60 celebrities in that day (27), to the fuselage failures in the de Havilland DH 106 Comet (28), to our more modern problems with fatigue in composites for the next generation of aerospace applications (29). Fatigue has always captured the attention of the public and scientist due to society's reliance on mechanical and structural components that move our society forward.

Basics of Fatigue

Metal fatigue as defined by the American Society for Testing of Materials (ASTM) is: "The process of progressive, localized, permanent, structural change occurring in a material subjected to conditions that produce fluctuating stresses and strains at some point or point, that may culminate in cracks or complete fracture after sufficient number of fluctuations (30)." It is generally known that damage caused by the localized stresses and strains occurs in the material at the atomistic level. The induced stress causes slip to occur within the grain. Most of metallic materials are polycrystalline so there are many grains and likely many grain orientations. Within any given crystal structure there are slip planes that enable slip to occur most easily. The planes that allow slip the easiest are the close packed planes. Crystal structures with a high number of close packed planes have more planes for slip to occur (31).

As stress is applied the atoms move by dislocations along these slip planes. Dislocations are defects in the crystal structure which ease the movement of the atoms along the slip planes. At the surface of the material the movement of the atoms along the slip planes causes extrusion and intrusions of material on the surface (32). For fatigue initiating at the surface a fatigue crack will begin at the areas of extrusion and intrusions.

In order for the crack to continue to grow it has to overcome the energy associated with moving from one grain to the next across a grain boundary. The amount of energy needed to overcome the grain boundary depends on whether the next grain is oriented in a favorable direction for slip to occur. If the grain is not in a favorable orientation, the crack will stop growing. If it is in a favorable orientation then the crack will continue.

In the early stage of fatigue the crack moves along the direction of maximum shear stress since it is the shear stress that drives dislocation movement along the favorable slip directions. This stage in the fatigue process is called Stage I. Once the crack has grown through a few grains

the direction of crack growth will be perpendicular to the direction of the applied principle stress. This is called Stage II crack growth, Figure 3.

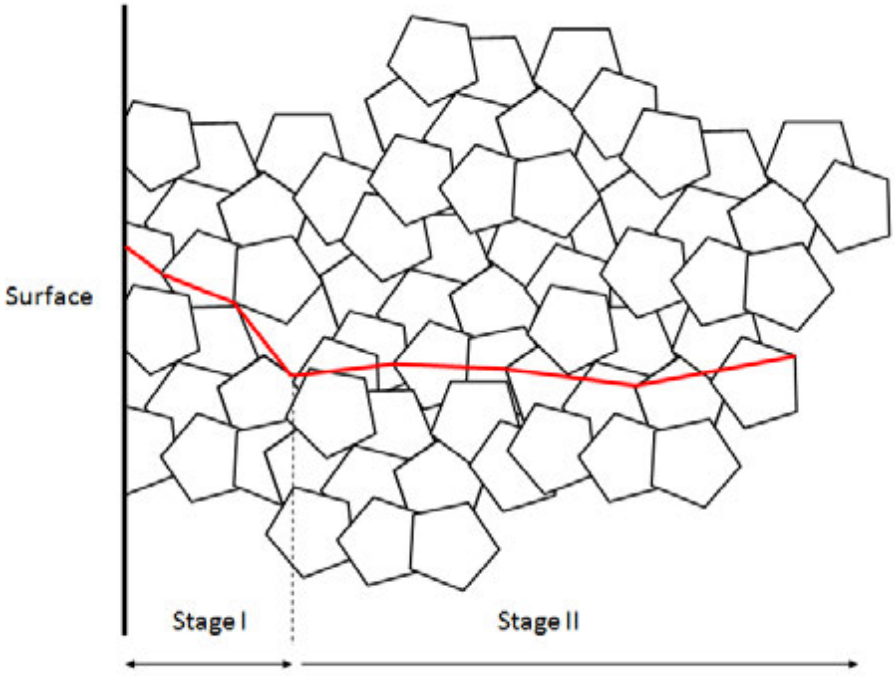

Figure 3) Schematic of the stages of the fatigue crack process.

In Stage I fatigue is examined on the microscopic level with analytic tools suitable for examining grains, dislocations and atomic planes. Physical metallurgist and physicist are involved in at this length scale. This is the area where improvement in fatigue life can be evaluated in the material as a function of atomic movement through the crystal structure, but at present it is impossible to predict quantitatively fatigue life of a macroscopic part based upon observations at this level. During Stage II the growing crack is examined through the use of continuum mechanics and the mechanical behavior of the material. This is the realm of the mechanical engineer and mechanical metallurgist. All current models for evaluating fatigue life

of a structure neglect the microscopic level and mechanical level of initiating an engineering size crack and growing the crack until failure or a predetermined size. In order to gain a true picture of fatigue both initiation and propagation need to be understood.

Fatigue Life Prediction

Historically, work concerning fatigue has been concentrated on developing fatigue life prediction methods for various applications. The area of study involving welded structures is no different. All fatigue life prediction methods start with a damage model, of which there are three basic approaches, those being the stress life, fracture mechanics and the strain life approaches. All three of these damage models need the stress/strain response of the material, which is dependent on the applied load (residual + external), the part geometry, and the material properties. The difference is in how the processing is accomplished to derive the needed information for the damage model. A sketch of this flow is shown in Figure 4. All four of the top level inputs are critical in analysis of welded joints. Each will be discussed in relevance to specific fatigue model used in subsequent chapters.

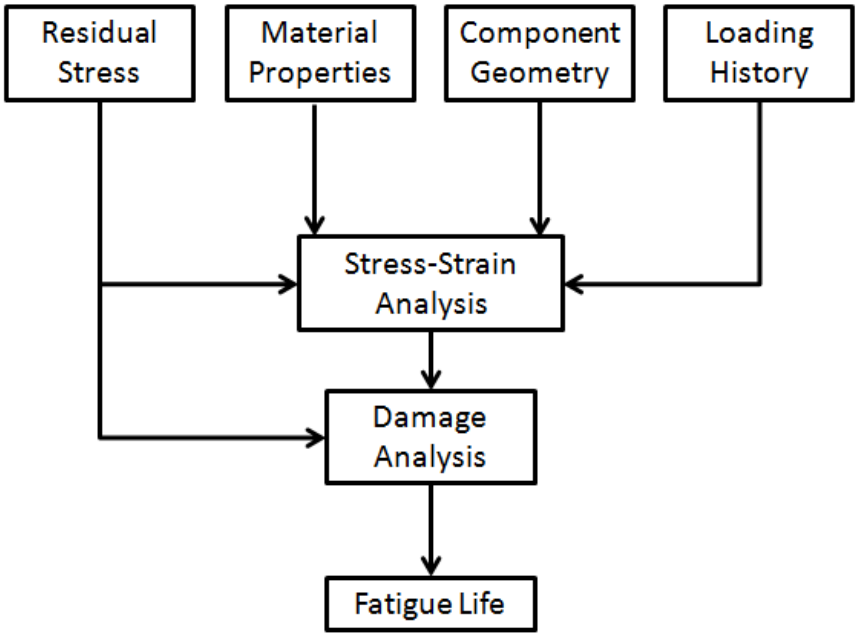

Figure 4) Information path for fatigue life prediction.

2.3 Fatigue Life Prediction Models

Common approaches to life prediction of welded structures

In life prediction of welded joints the literature provides six broad areas that fit within the three general methods for predicting the fatigue life of welded components. These are discussed in turn below.

Nominal Stress Approach: This method uses the standard stress life or *S-N* approach with detailed classification of weld structure geometries. The S-N approach plots the number of cycles, *N*, as a function of the stress, *S*. The frame work for this method was developed in the 1970s (33), and was later adopted by the International Institute of Welding (IIW) (34). Much of the recent work in the area of the nominal stress approach has been in developing methodologies to account for mean stresses, residual stresses, life improvement techniques and size effects (35).

The S-N approach is very simple and easy to apply in principle. In practice the method is very difficult to apply to complex joints and loading histories because the curves used in this method were developed from fatigue testing representative samples of specific geometries. In practice it is rare to have an exact match to one of the geometries that is in the standard. The other problem with the S-N curves is the failure criteria are not noted, so the analyst does not know how large the crack is at the end of the predicted life. The authors responsible for developing industry specifications understand this limitation and compensate by reducing the curves to have very conservative life predictions. This makes it impossible for the designer to optimize the design of the structure. All of the S-N based approaches have the same issues as described above.

Structural Stress or Hotspot Stress Approach: This improvement on the traditional nominal stress approach uses the stress at the critical location (in the case of this dissertation work the weld toe) and applies this stress to a specially developed S-N curve. The classification weld joint is still used to pick the corresponding S-N curve for the joint's geometry. There is much debate in the literature as to how best to determine the hot spot stress. (36).

Notch Stress Approach: This method uses linear elastic stress calculations at the critical location of crack initiation and propagation, in this case the weld toe. If the discontinuity of the weld is treated as a sharp notch the stress at the critical location is artificially high due to the singularity in the FEA solution. A singularity in a FEA analysis is where the calculation goes to infinity due to a "crack like" feature in the mesh. In the model there is no radius modeled and therefore the calculation is artificially high. Physically the stress does not reach infinity, due to plasticity and crack tip blunting. Debate in this approach is directed at how to account for the singularity. The most common method is to assign a radius to the notch. Three different methods for assigning the radius were suggested by Lawrence, Radaj and Seeger (37), (38), (39). The

notch stress approach uses the S-N weld curves, as described in the previous sections, to determine the life of the structure.

Notch Life Approach: This method uses the singularity of the sharp notch to calculate the elastic stress in front of the crack. Verreman and Nie used what they called the notch stress intensity factor, N-SIF, to correlate the N-SIF to the initiation life for welded structures (40). Atzori showed later, that the notch stress approach can be coupled with the crack propagation methods used in fracture mechanics (41).

Crack Propagation Approach: This method is the common fracture mechanics approach developed by Paris (42) to predict crack propagation. This approach is used in practice to determine the life of structures where crack tolerant designs are used, such as in the oil, and aerospace industries (43). Crack tolerant design is a design methodology that calculates the largest safe crack as the design criteria using fracture mechanics. First the critical crack size is calculated using the crack geometry and fracture toughness of the material. Then the life for the crack to propagate from a predetermined initial crack size to the critical crack size is calculated.

The difficult part in applying the crack propagation method to welded structures is in determining the stress intensity factor (SIF) for the weld. This is because weld geometries vary greatly, thus, handbook values specifying the SIF for any particular weld are rarely found. While determination is straight-forward as far as methodology, the process is time consuming. Finite element analysis can be used to determine the SIF, but again it can only be used in industries where safety concerns are high enough to make the time and financial commitment to determine the SIF worthwhile.

Notch Strain Approach: The final method, and the one that will be applied in this analysis, is the Notch Strain or Strain Life approach A detailed description of this approach is thus in order and is found in the next section.

Notch strain/strain life approach

One of the most widely used fatigue life prediction methods is the Notch Strain approach, otherwise commonly known as the Strain Life method. The Strain Life (ε-N) method uses the total strain present at the critical location most likely to fail in determining the predicted life. An overview of the complete ε-N method as it relates to a welded structure is outlined in the following steps and depicted in the graphic of Figure 5 (44). Briefly, these steps are:

Step 1: Determine the external loads on the structure and the boundary conditions (Figure 5a).

Step 2: Calculate the internal loads in the structure (Figure 5b).

Step 3: Determine the critical points in the structure (Figure 5c).

Step 4: Calculate the peak stress at the critical points (Figure 5 d, e).

Step 5: Define the peak stress history (Figure 5 f).

Step 6: Determine the elasto-plastic stress-strain response at the critical points (Figure 5 g).

Step 7: Obtain the Stress-Strain hysteresis loops (Figure 5h).

Step 8: Determine the fatigue damage and fatigue life (Figure 5 i-l).

Steps 1 and 2, determine the external loads and calculate the internal loads. These forces come directly from the application for which the structure is designed and are obtained through analysis of the structure and a free body diagram (a-b in Figure 5). Step 3, determination of the critical points, is the first stress analysis of the structure (c in Figure 5). This can be done with

hand calculations, but it is most commonly done with a structural FEA model. Since the information gathered in steps 1 through 3 are generic in nature and apply to all structural analyses they will not be discussed in this dissertation.

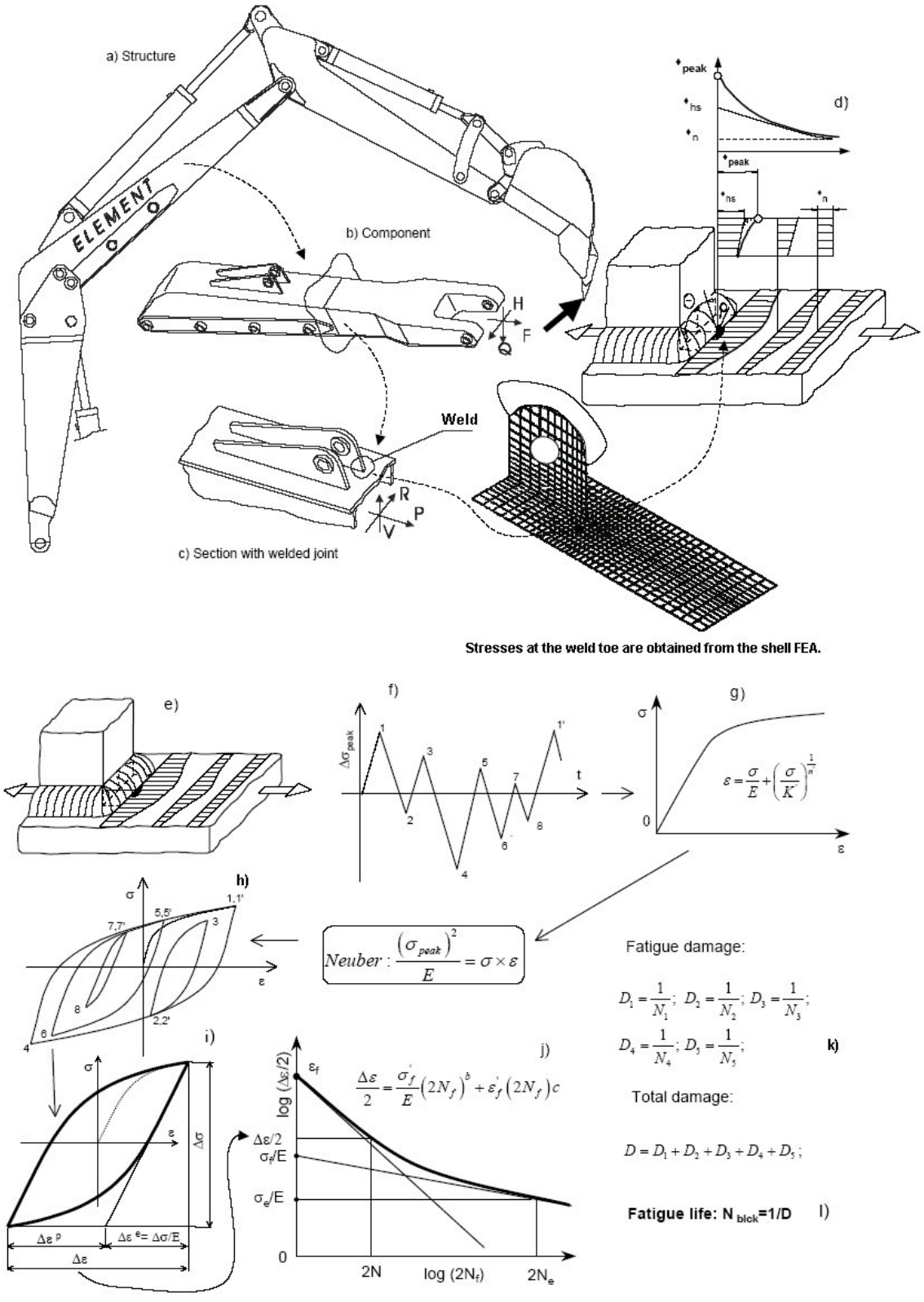

Figure 5) Steps in fatigue life prediction based on the strain-life approach (44).

Fatigue is driven by the peak stress to which the part is subjected, and this stress is calculated in Step 4 (d-e in Figure 5). Typically FEA tools are used to accomplish this task with the addition of the stress concentration from the weld. The most common method of modeling the peak stress is linear elastic FEA, where the plasticity in the material is ignored. Step 5, determine the peak stress history, is needed when the component is subjected to variable amplitude loading, i.e., loading where the values of the maximum and minimum stresses vary (f in Figure 5). While extremely important for real-world applications, constant amplitude loading was used in this work to simplify the problem. Although the determination of the peak stress history in situations where the load varies does not play a part in the experiments conducted and is therefore irrelevant for the analyses of this dissertation, the reader is directed to reference (32) for further details.

While linear elastic FEA (employed in Step 4) is simple and easily done it does not account for the elasto-plastic behavior of most materials. Thus, the linear elastic stresses determined in Step 4 need to be translated into to elasto-plastic stresses. This is done in Step 6, and the resulting values are then used in the Step 7 to obtain the stress-strain hysteresis loop (g-i in Figure 5). The stress-strain hysteresis loop is needed to calculate the strain amplitude, which is used Step 8 in determining the damage and the resulting fatigue life (j-l in Figure 5).
Details concerning the methods and calculations used in Steps 4 and 6-8 are given in the next sections.

Calculation of peak stress (Step 4)

The notch strain approach requires the stress at the notch location which is referred to as the peak stress. This can be obtained through direct or indirect methods. The most common method is the indirect method where the stress is calculated at a location where the stress is easier

to obtain and a scaling factor is used to obtain the peak stress. Several methods of obtaining the peak stress will be described and discussed in this section.

To begin there are three definitions of the stress that need to be understood. The first is the peak stress, σ_{peak}, which is the peak stress at the critical location; in this case the weld toe. The peak stress accounts for the local geometry and the weld stiffness effects. The nominal stress, σ_n, is the stress that is away from the weld and does not account for the effects of the weld. Finally the hot spot stress, σ_{hs} , which is defined as the stress at the critical location not including the increase in stress due to the weld toe geometry, but does account for the stiffness. The pictorial of these stresses are shown in Figure 6.

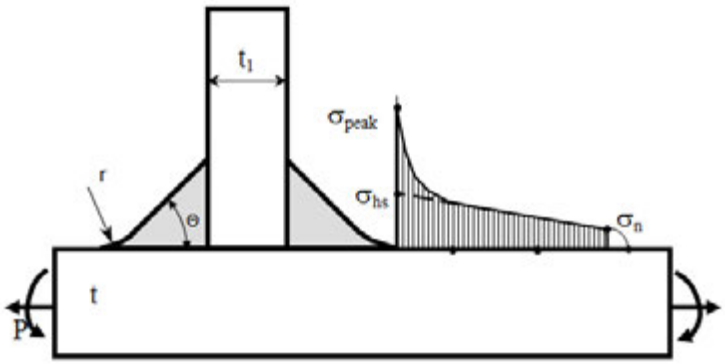

Figure 6) Sketch of the reference stresses in a weld analysis.

The end goal is to determine the peak stress, but this is not a trivial task. The more common method is to determine hot spot or nominal stress and multiply these by a scaling factor, referred to as the stress concentration, to obtain the peak stress. The definition of the stress concentration factor is provided in Equation 2.

$$K_t = \frac{\sigma_{peak}}{\sigma_n} \quad \text{or} \quad K_t = \frac{\sigma_{peak}}{\sigma_{hs}} \qquad \text{Equation 2}$$

where K_t is the stress concentration factor.

There are several ways determining the stresses needed, but the most common is to use linear elastic FEA. Three of the most common modeling methods are discussed below.

Fine mesh FEA can be used to accurately model both the macro and micro geometry of the weld toe (45). Since the geometry is accounted for in the model the resultant stress can be directly determined from the model so there is no need to apply a stress concentration factor to obtain the peak stress. The trick in the fine mesh FEA technique is to use small enough elements to capture the stress at the weld toe accurately, but also maintain a model size that can be run efficiently.

In a research environment capturing the true geometry in a fine mesh FEA model is achievable for small test samples. However, in a commercial application this method is too time consuming in computer modeling and run time, causing other methods to be used.

The shell mesh method uses shell elements to represent the structure and weld (45). In this method the peak stress cannot be read directly from the model because the local geometry is not captured and thus not accurate without further post processing. However, it has the advantage over fine mesh FEA in that it can be run quickly on computers of limited computing power. Shell element models of welded structures are capable of providing the hot spot stress and nominal stress, but not the peak stress. In this method the structural stress is adjusted to account for the stress concentration of the local weld geometry. Modeling techniques developed by Dong use shell meshes to capture the stiffness effects of the weld (46). The hot spot stress can be read directly from the mesh, making post processing of the data for further fatigue analysis easy.

The coarse mesh method is similar to the shell mesh method. Better suited for thick plate structures, the coarse mesh method was developed by Chattopadhyay as a variation of the calculation of the hot spot stress that uses a 3D coarse mesh rather than a shell mesh (47). A similar method was also developed by Dong (46). The major drawback of this method is that the mesh is not fine enough to capture the micro-geometry of the weld, especially at the weld toe, and requires extrapolation of the stresses through the thickness at the weld toe to calculate the hot spot stress at the weld toe. However, like the shell method it is considerable faster than fine mesh FEA. As with the other hot spot stress methods the peak stress is calculated using the stress concentration from the weld.

Since the fine mesh technique is not practical for most welded structures there has been much research studying how best to apply the stress concentration to the hot spot stress. Research by Monahan has shown that the stress concentration is different for parts subjected to bending versus tension stresses (48). Thus, when considering the hot spot stress the total has to be separated into the bending and tension stress components as shown in Figure 7. The specific stress concentration can then be applied to each component separately. The summation of the individual stress components multiplied by the stress concentration is then the peak stress used for the analysis. This is shown in Equation 3.

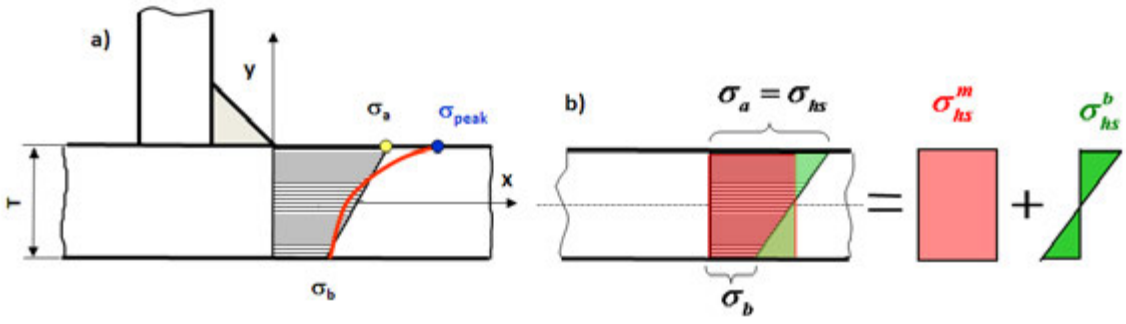

Figure 7) Sketch showing the breakdown of membrane and bending stresses of a T-joint.

$$\sigma_{peak} = \sigma_{hs_b} K_{t_b} + \sigma_{hs_m} K_{t_m} \qquad \text{Equation 3}$$

Where σ_{hs_b} is the structural or hot spot stress in bending, σ_{hs_m} is the structural or hot spot stress in tension, K_{t_b} is the stress concentration factor for bending and K_{t_m} is the stress concentration factor for tension.

Stress concentrations at welds have been well studied in the literature for symmetrical welded joints (48) (49) (50) (51). The common method of determining the stress concentration factor of weld is to use structural FEA tools to vary the key parameters. The most common input parameters are the weld toe radius (ρ), weld angle (Θ), and thickness of plates (t) (48), (52). The most detailed expression to-date is provided by Iida and Uemura (52). Their expression, Equation 4 , Kt for tensile stresses, and Equation 5, Kt for bending stresses, for the "T-weld" geometry includes the common factors listed above along with the amount of weld penetration, the weld size, and independent thickness values for each plate (52). Only the expressions for a T-weld subjected to bending and tension stresses are provided in this work. Figure 8 is a sketch of the weld showing the equation variables and the location of where the stress concentration equations apply.

Once the peak stress is determined the next step in the process, Step 5, is to define the peak stress history. Because the loading history used in this dissertation was constant amplitude this step does not apply and can be skipped. The next section will discuss Step 6, determining the elasto-plastic response at the notch.

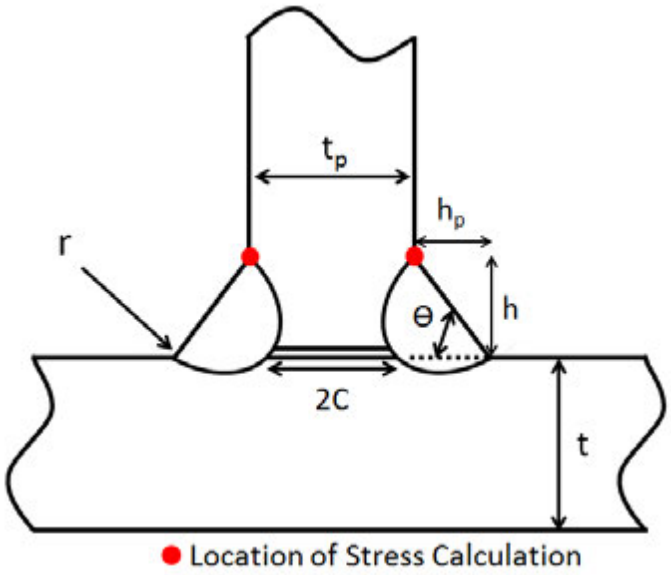

Figure 8) Sketch showing the variables used in the following equations. Note the loading on this sample is in bending on the vertical section. (52).

$$K_{t,hs}^{m} = \left\{1 + \frac{1+exp\left(-0.9(0.5\pi-\theta)\sqrt{\frac{W}{2h_p}}\right)}{1-exp\left(-0.45\pi\sqrt{\frac{W}{2h_p}}\right)} \times 2.2\left[\frac{1}{2.8\left(\frac{W}{t_p}\right)-2} \times \frac{h_p}{r}\right]^{0.65}\right\} \times \left\{1 + 0.64\frac{\left(\frac{2c}{t_p}\right)^2}{\frac{2h}{t_p}} - 0.12\frac{\left(\frac{2c}{t_p}\right)^4}{\left(\frac{2h}{t_p}\right)^2}\right\}$$

Equation 4

$$K_{t,hs}^{b} = \left\{1 + \frac{1+exp\left(-0.9\theta\sqrt{\frac{W}{2h_p}}\right)}{1-exp\left(-0.45\pi\sqrt{\frac{W}{2h_p}}\right)} \times \sqrt{\tanh\left(\frac{2t}{t_p+2h_p} + \frac{2r}{t_p}\right)} \times \tanh\left[\frac{\left(\frac{2h}{t_p}\right)^{0.25}}{1.\frac{r}{t_p}}\right] \times \left[\frac{0.13+0.65\left(1.\frac{r}{t_p}\right)^4}{\frac{r}{t_p}^{\frac{1}{3}}}\right]\right\} \times$$

$$\left\{1 + 0.64\frac{\left(\frac{2c}{t_p}\right)^2}{\frac{2h}{t_p}} - 0.12\frac{\left(\frac{2c}{t_p}\right)^4}{\left(\frac{2h}{t_p}\right)^2}\right\}$$

Equation 5

Where: $W = \left(t_p + 4h_p\right) + 0.3(t + 2h)$ Ref (52)

The variable definitions for Equation 4 and Equation 5 are provided in Figure 8.

Elasto-plastic stress strain response (step 6)

It is not unusual to have strains in notches that concentrate the stresses and strains that exceed the yield limit even when the bulk material is below the yield limit. This is shown in the fine mesh FEA model that accounts for the local geometry at the weld toe Figure 9. The area of high strain is depicted in red which is concentrated at the weld toe, but below this region the majority of the cross section is still at low strain.

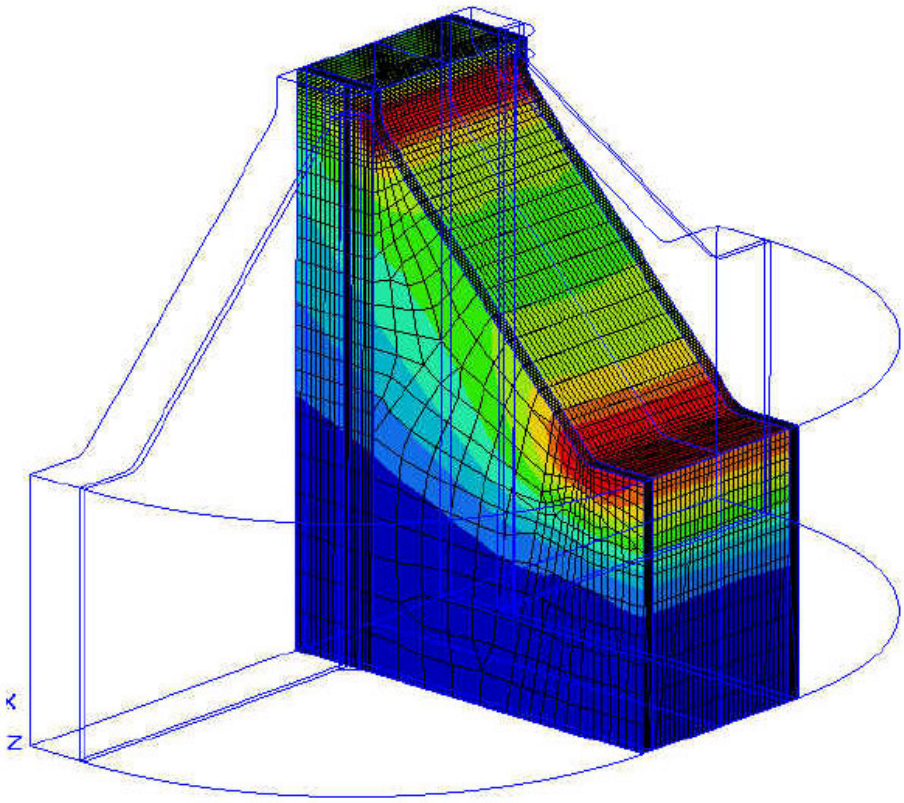

Figure 9) Fine mesh FEA model showing the localized increase in strain at the weld toe.

Most analysis methods assume that the material behavior is linear elastic in nature. The stresses from the linear elastic analysis need to be converted to elasto-plastic stresses prior to applying the strain life method. The linear elastic analysis is used because it is easy to apply and runs very quickly, but it does not capture the true elasto-plastic behavior of the materials. The actual stresses and strains are needed for accurate calculations. One common way of accomplishing acquiring the elasto-plastic materials response from a linear elastic analysis is by using the Neuber rule (53). The Neuber rule states that the geometrical mean of the stress concentration factors remains equal to the theoretical stress concentration K_t even when yielding has occurred.

$$K_t = \sqrt{K_\varepsilon \cdot K_\sigma} \qquad \text{Equation 6}$$

The expression K_ε is the strain concentration factor which is $K_\varepsilon = \varepsilon/e$ where ε is the local strain, e is the nominal strain and K_σ is the stress concentration factor which is $K_\sigma = \sigma/S$ where σ is the local stress and S is the nominal stress.

Since the nominal stress and strain is related by Hooke's Law, $e = S/E$, in a linear elastic stress analysis, the Neuber relationship can be rewritten as:

$$\frac{(K_t \cdot S)^2}{E} = \sigma\varepsilon \qquad \text{Equation 7}$$

Where $\frac{(K_t \cdot S)^2}{E}$ can be calculated from the nominal stress and $\sigma\varepsilon$ are the true stress and strain a result of the loading at the notch tip. The Kt for weld toes is discussed in Section 2.3.3. Since there are two unknowns a second equation is needed to solve this expression. The most common

equation is the Ramberg Osgood expression, shown in Equation 8, which provides the strain as a function of stress (54).

$$\varepsilon = \frac{\sigma}{E} + \left(\frac{\sigma}{K'}\right)^{\frac{1}{n'}} \qquad \text{Equation 8}$$

Where ε is the strain, σ is the stress, *K'* is the cyclic strength coefficient and *n'* is the cyclic strain hardening exponent. The theoretical stress, σ, can then be calculated using iterative solving techniques through substitution of the Ramberg-Osgood expression into the Neuber relationship. The theoretical strain, ε, is then calculated by substituting the theoretical stress back into the Ramberg-Osgood equation.

$$\sigma\left(\frac{\sigma}{E} + \left(\frac{\sigma}{K'}\right)^{\frac{1}{n'}}\right) = \frac{(K_t \cdot S)^2}{E} \qquad \text{Equation 9}$$

Calculation of Stress-Strain hysteresis loops (step 7)

When a material is loaded the stress / strain relationship follows a characteristic curve called the stress / strain curve. A similar characteristic behavior is seen when a material is cyclically loaded. Since the fatigue damage, used in Step 8 and discussed in the next section, is calculated using the strain amplitude, it is necessary to determine the strain amplitude of a given cycle.

It is common for the stress on the part as a response to loading to be reported. In order to determine the strain for a given stress, the relationship between stress and strain must be modeled. The most common expression for modeling the stress/strain response of a material is the

Ramberg-Osgood relationship shown in Equation 8 (55). This originally was proposed to model the monotonic behavior of materials but since the cyclic behavior of the material follows the same shape it can be used to also model the cyclic stress strain response (54). The values of *K'* and *n'* in the Ramberg-Osgood relationship are determined experimentally from the stabilized cyclic hysteresis loops from strain life testing which is discussed in the Material Properties section.

To better understand the cyclic stress strain response of the material it is good to look at it graphically. To begin the Ramberg-Osgood relationship is used to model the stress strain behavior of the material loaded from 0 to a stress of σ_A denoted by segment O-A shown in Figure 10. When the sample is unloaded the slope of the curve follows the modulus of elasticity (*E*), which is represented by segment A-B, in Figure 10. When the sample is subjected to a compressive stress equal to $-\sigma_A$, the material starts yielding at a stress level less than the original yield stress limit, σ_y. This phenomenon is described at the Bauschinger effect (54). It was observed by Massing (54), that the stress-strain curve going into compression, along path A-C, can be modeled by expanding the original curve, O-A, by a factor of two.

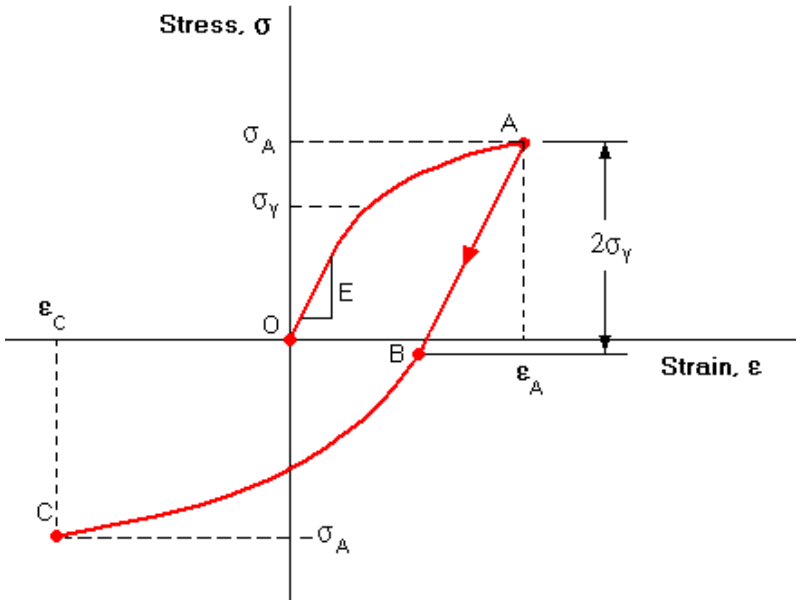

Figure 10) Developing the hysteresis loop curve from the cyclic stress-strain curve based on Massing's hypothesis.

If the loading process shown in Figure 10 is continued from $-\sigma_A$ to $+\sigma_A$, then a hysteresis stress-strain loop will be created as shown in Figure 11. The hysteresis loop defines a single fatigue stress-strain cycle.

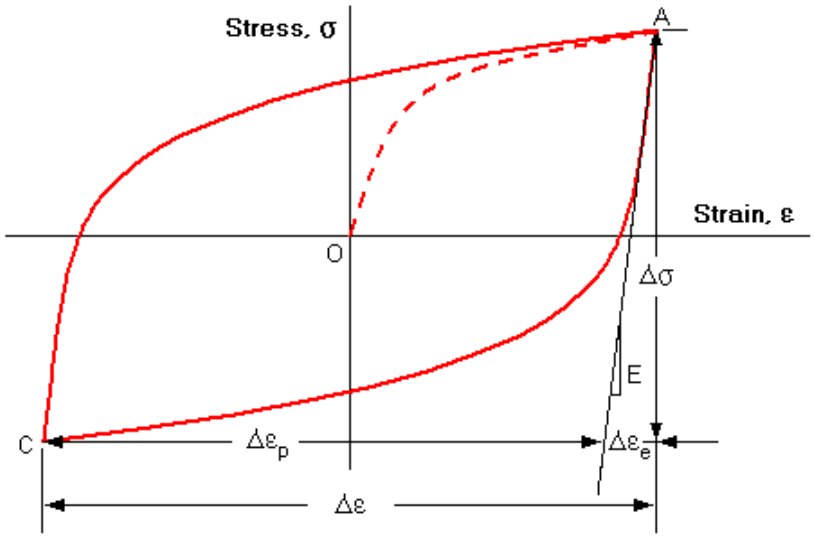

Figure 11) Hysteresis stress-strain loop.

Massing's hypothesis states that the stabilized hysteresis loop path may be obtained by expanding the original curve O-A by a factor of two given in the form of Equation 8. The reversing point A is assumed to be the origin of the new system of co-ordinates for the hysteresis loop branch described mathematically as:

$$\frac{\Delta\varepsilon_A}{2} = \frac{\Delta\sigma_A}{2E} + \left(\frac{\Delta\sigma_A}{2K'}\right)^{\frac{1}{n'}} \qquad \text{Equation 10}$$

Multiplying both sides of Equation 10 by a factor of 2, the general equation for the hysteresis loop branch can be derived:

$$\Delta\varepsilon = \frac{\Delta\sigma}{E} + 2\left(\frac{\Delta\sigma}{2K'}\right)^{\frac{1}{n'}} \qquad \text{Equation 11}$$

The use of Massing's hypothesis allows the hysteresis loop stress-strain path to be described by the same constants as those in the equation of the stabilized cyclic stress-strain curve shown in Equation 9.

Fatigue damage and life prediction for strain life approach (step 8)

In the final step the notch strain approach uses the combined Basquin and Manson-Coffin equations to relate the total strain amplitude to the number of cycles:

$$\frac{\Delta\varepsilon}{2} = \frac{\sigma_f'}{E}\left(2N_f\right)^b + \varepsilon_f'\left(2N_f\right)^c \qquad \text{Equation 12}$$

Where $\frac{\Delta\varepsilon}{2}$ is the strain amplitude, E is the modulus of elasticity, $\sigma_f^{'}$ is the fatigue strength coefficient, b is fatigue strength exponent, $\varepsilon_f^{'}$, is the fatigue ductility coefficient, c is the fatigue ductility exponent and $2N_f$ is the number of strain reversals to crack initiation (54). Although Equation 12 is made up of the work of Basquin and Manson-Coffin, it is referred to as the Manson-Coffin equation. There is no direct solution to the Manson-Coffin equation so the equation is solved iteratively to determine predicted life.

2.4 Material properties

As described in the previous section, the strain life method uses both the cyclic stress strain curve fit to the Ramberg-Osgood curve and the relationship of strain amplitude to number of cycles in the form of the Manson-Coffin equation. The material properties required as input into this method are obtained by physical testing as per ASTM E606 (56). A number of samples, typically 20, are tested to create the fatigue life curve. The material properties obtained via this testing for the Ramburg Osgood curve (Equation 8) are the cyclic strength coefficient (K') and the cyclic strain hardening exponent (n'). The peak stress and the plastic strain amplitude are used to calculate the material properties from the test data.

The material properties for the Manson-Coffin relationship, shown in Equation 12, are the fatigue strength coefficient, σ_f' , the fatigue strength exponent, b, the fatigue ductility coefficient, ε_f', and the fatigue ductility exponent, c. In general these properties are derived from the stabilized hysteresis loops from the strain life tests. The elastic strain verse number of cycles is used to fit the fatigue strength coefficient and fatigue strength exponent using Basquin's portion of the Manson-Coffin equation:

$$\frac{\Delta \varepsilon_e}{2} = \frac{\sigma_f'}{E}(2N_f)^b \qquad \text{Equation 13}$$

The plastic portion of the Manson-Coffin equation is used to determine the fatigue ductility coefficient and fatigue ductility exponent in Equation 14. The method for determining the constants using linear regression is described in ASTM E739.

$$\frac{\Delta \varepsilon_p}{2} = \varepsilon_f' \left(2N_f\right)^c \qquad \text{Equation 14}$$

2.5 Residual stress and its measurements

As shown in Figure 4, residual stresses that are induced during the welding process also must be considered when performing a fatigue life prediction. Residual stress is defined as self-equilibrating stresses that are contained within the work piece due to manufacturing / processing parameters rather than due to applied forces. Residual stresses come about due to misfits between different regions, different parts and/or different phases (58). They have been divided up into three different types of stresses by the length scales over which they equilibrate (59), which are summarized below.

Type III: These are stresses that are equilibrated over a length scale on the order of the atomic level and are, therefore, much smaller than the grain size. These stresses arise due to mismatch in the lattice structure due to dislocations. Type III residual stress is neither useful nor important from an engineering point of view.

Type II: These stresses equilibrate over a length scale of about three times the grain size. Type II stresses arise due to microstructural phase differences. To predict these stresses a detailed simulation of the microstructure is done. There is limited use of these models and no industrial applications have yet arisen.

Type I: These residual stresses equilibrate over a macro scale on the order of the dimensions of the part. These stresses are the most familiar to engineers and have been studied thoroughly. These stresses can be calculated using continuum mechanics and finite element analysis if enough information is known about the material properties and design of the part in question.

2.5.1 Residual stress effects on durability:

It is widely known that the residual stress state of a component will play a role in the durability of a product (60). In general, residual compressive stresses increase the life while tensile stresses decrease fatigue life, Figure 12.

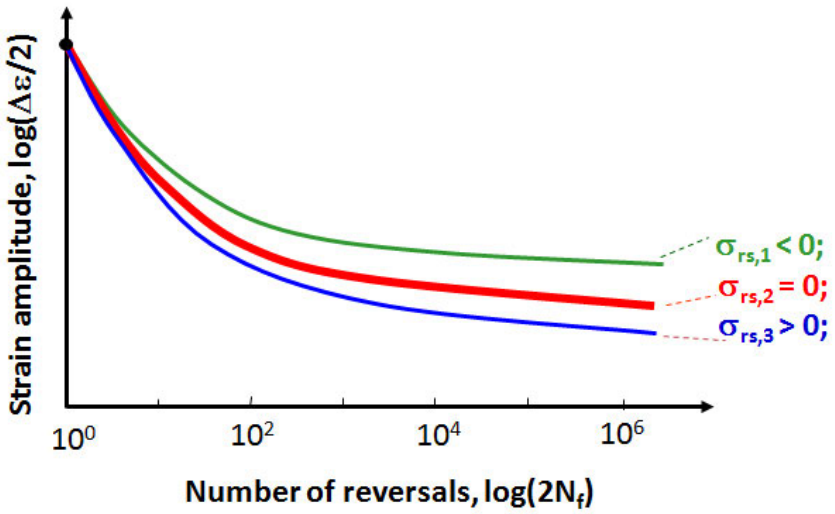

Figure 12) Graph showing the general effect of residual stress on the strain life curve of a material.

An accurate but sometimes misapplied view of residual stresses is to think of them as a mean stress on the component. For any component, the material is not concerned if the stress it

feels is due to an outside applied stresses or is present as an internal residual stress; durability (and ultimately, failure) is simply related to the stress to which the part is subjected. This is akin to people who do not care if the stress is from work or *writing a dissertation;* the final result is the stress they feel.

This can be seen when looking at the hysteresis loops (discussed in section 2.3.5) and noting how the residual stress changes the expected loop. The hysteresis loop shown in Figure 13a is characteristic of a part exhibiting no residual stress. The loop is centered with no mean stress. Figure 13b shows how the hysteresis loop changes with application of a residual tensile stress. The overall result is that the initial residual stress results in a mean tensile stress. The opposite is true when it comes to a residual compressive stress, Figure 13c. The residual compressive stress results in a mean compressive stress during operation. A schematic representation of stress versus time as it relates to the stress strain response of the material for these three scenarios is shown in Figure 14.

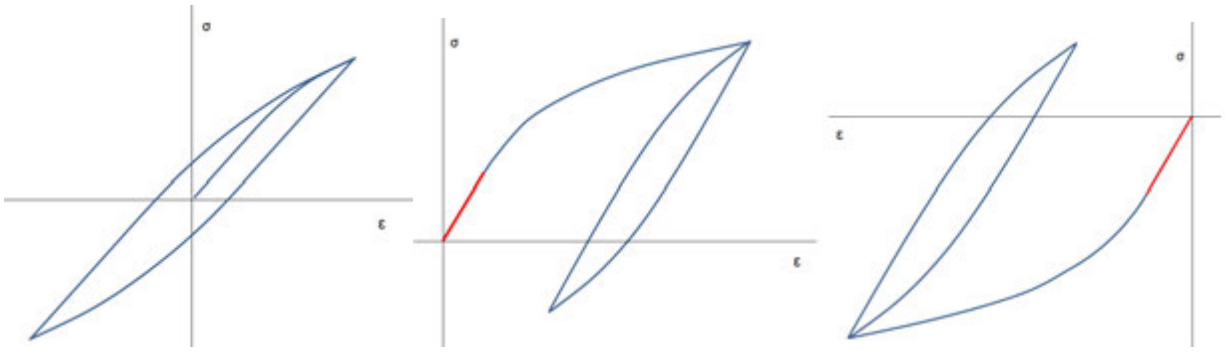

a) b) c)

Figure 13) Stress strain hysteresis loops for a) no residual stresses b) tensile residual stress and c) for compressive residual stress.

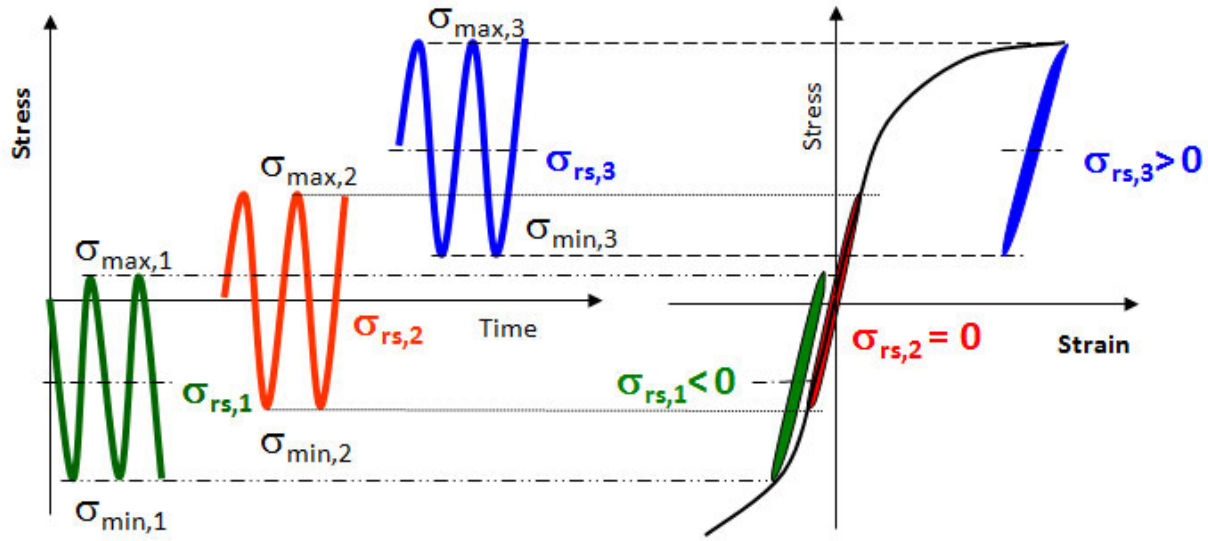

Figure 14) Stress profile and hysteresis loop for different residual stress.

The misapplication referred to above comes in the way the residual stresses are applied in the stress analysis. It is common in fatigue analysis to treat the residual stress as a mean stress. In this case when running a linear elastic analysis with a stress concentration the residual stresses are subjected to the stress concentration in the stress analysis. If this mistake is made, then the residual stresses would be over compensated since residual stresses are not affected by the stress concentration as applied stresses are.

An example of this is shown in Figure 15. Figure 15a shows the hysteresis loop for an application of residual stress correctly, while Figure 15b is application of the residual stress as a mean stress. A stress concentration of 3, an applied stress of 200 MPa, and a residual stress of

100 MPa, along with representative material properties, was used in this comparison. The predicted life for the correct application of residual stress is 1.83×10^6 and treating the residual stress as a mean stress results in a life of 8.98×10^5. It can be clearly seen that the misapplication of residual stress can lead to large errors in the stress analysis, thus leading to significant error in life predictions.

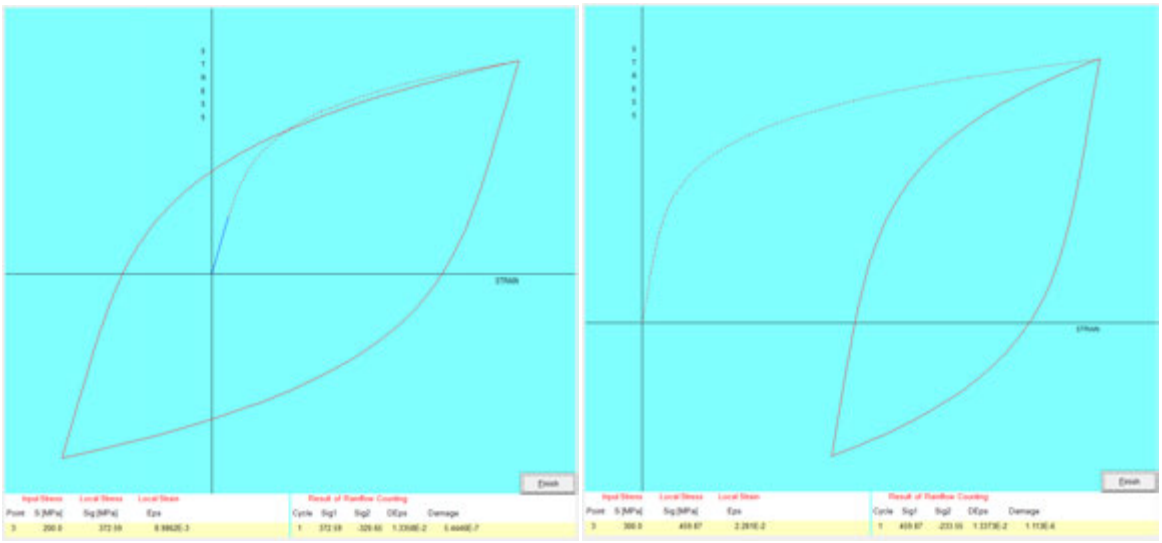

a) b)

Figure 15) Comparison in the application of the residual stress verses mean stress in stress analysis.

2.5.2 Residual stresses in welds:

As shown in the previous section, residual stress can affect the stress state of the material during loading for better or worse, depending on the sign of the stress. For that reason it is important to understand how residual stresses develop in welds.

The dominate factor in residual stress development is the change in volume of the weld pool and heat affected zone (HAZ) during the thermal cycle that results when welding. Upon

heating, the weld pool and HAZ expand, resulting in a residual compressive stress in the weld and a tensile stress in the base material. As the material solidifies and cools, the volume contacts; this leads to a residual tensile stress in the weld and compressive stress in the base material. These results can be affected or even reversed if significant microstructural phase changes occur. Ueda *et al.* developed a shrinkage model as a way of modeling residual stresses and distortions (61). In his model the amount of volumetric contraction was calculated through the use of thermal and microstructural models.

The development of residual stresses in a weld due to heating can be understood by looking at a simple example of non-uniform heating in three bars (Figure 16). At time 0 when the bars are at the same temperature there is no stress in the system. If the bars are heated uniformly together and allowed to expand and then cooled uniformly there are no residual stresses introduced. However, if only the middle bar is allowed to heat the other bars will resist the expansion of this bar, placing them in tension while the heated bar, being restrained by the cooler outside bars, is in compression. If there is no plastic deformation, then upon cooling the bars will go back to the original shape and there will be no residual stresses in the part. If there is plastic deformation the bars will not return to the original shape and residual stresses will result (62). The central bar will be left with a residual tensile stress while the outside bars are in compression.

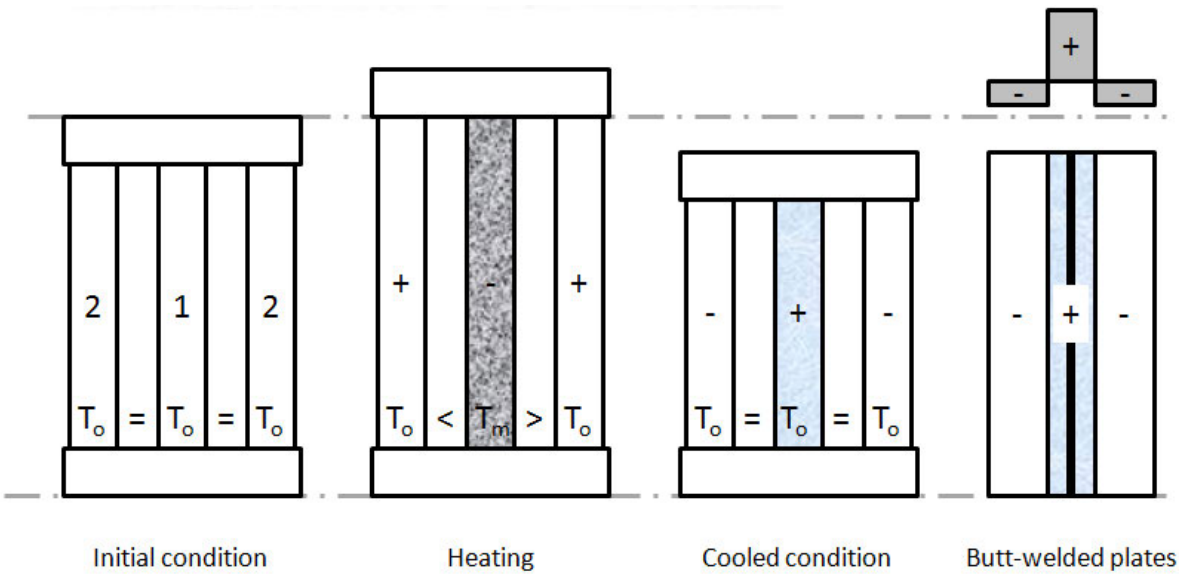

Figure 16) Three-rods system constrained by ridged bases, and a butt-welded plate simulated by the three-rod system.

The case just described is in many ways analogous to welding, where plastic deformation almost always results. This is because local heating of the material adjacent to the weld pool causes a drastic reduction in the yield strength of the material in that region while the majority of the material stays at a much lower temperature. At high temperatures the heated material yields plastically very easily since the yield strength drops with increasing temperature. Thus, a residual tensile stress results in the region of the weld toe.

The typical residual stress pattern in a weld is shown in Figure 16. After cooling the weld bead and toe are in residual tension with a balance of residual compression outside of the tension zone.

2.5.3 Residual stress measurement:

Accurate residual stress measurement is required if quantitative values are going to be incorporated into any comprehensive durability model. Unfortunately, residual stress measurement can be difficult, time-consuming, and is currently limited to test pieces rather than as part of the manufacturing / production process. In general there are three different methods of residual stress measurement, and these types are discussed in brief below. For more detailed information on residual stress measurement techniques see Withers and Bhadeshia's (59) in the bibliography.

The first method encompasses various stress relaxation measurements. This method involves removing material, either by drilling a hole, cutting a slit etc., as a way of relaxing the residual stress. The strains (i.e. displacement(s) of the part) that result from the relaxation are then measured. The stress state from the "before cutting" and "after cutting" conditions are then compared to calculate the stress state that must have existed before the relaxation. These methods are destructive in nature due to the removal of material. Depending on the amount of material, Type I or Type II stresses (Section 2.5 Residual stress and its measurements) can be measured using these techniques.

The second general method of residual stress measurement involves measuring the atomic lattice strain. This methods use diffraction techniques, involving either x-rays or neutrons (63), to measure atomic lattice spacing. The measured spacing is then compared to an unstressed lattice spacing to calculate the residual stress. These techniques are limited both by the size and depth of penetration of the beam and the physical size of sample that any particular instrument can accommodate. They also rely on having an unstressed sample as a reference standard. All three types of residual stresses can be measured, again depending on the beam and sample size.

The third general method of residual stress measurement techniques measures the change in response in an applied magnetic field or ultrasonic energy to deduce changes in stress. These techniques are the newest, are non-destructive, and provide the fastest measurement time, but they do not provide the stress distribution as a function of depth, which is needed for durability predictions. The measured response is also a function of microstructural factors in addition to residual stress, which makes interpretation somewhat complicated. Microstructural complications currently limit applicability of these techniques.

Clearly, residual stresses are very difficult and time consuming to measure, and there is no one technique that provides all of the information that is needed in order to make an accurate life prediction. For this reason, more and more engineers are turning to process simulation to provide an understanding of the stress distribution in their parts. The next section will discuss modeling techniques to acquire the residual stress state from simulation of the welding process.

2.6 Weld process simulation

Given the complexity and multi-faceted nature of the problem of life-prediction in welded structures it can be seen from the brief description above that a cost-effective solution can only come through computational simulation. The modeling of the welding manufacturing process is truly a multi-physics problem. The weld pool behavior is governed by electromagnetic and fluid dynamics, which determine the current density of the weld. The current density affects the heating of the part, which changes the microstructure, which in turn is governed by thermodynamic and kinetic considerations. Distortion and residual stress is dependent on the mechanical properties of the material, phase transformations occurring in the material, heat input and mechanical boundary conditions imposed by the clamping of the structure. Another complexity is the span of length scales. The analysis crosses many length scales, from phase

transformations in the microstructure, which occur on the nano- to micrometer scale, to weld distortions that result at the millimeter level, to the overall deformation of the final component structure that may be on the meter scale.

The interaction of all of these physical processes must be accounted for to fully model the welding process. The complexity of the problem creates difficulty in optimization of welded designs that incorporate welding simulation since this level of complexity requires considerable computing power. In the past weld modeling was limited to 2D or very small 3D models (64) and full weld analysis with traditional computation codes that only account for the thermal, microstructural and mechanical aspects are available. However, these models do not include the influence of the arc, nor do they fully consider the variety of coupled physical phenomenon, i.e., electromagnetic, weld pool (computational fluid dynamics), microstructure and phase changes during solidification, mechanics and residual stresses (FEA), and the multi length scales involved. Current widely used 2D approximations fail to represent real structures

Today computing power is just reaching the point where modeling full size welded structures is feasible. Still, analyses can be computer intensive, requiring weeks to run a simulation. Even with modern resources an unsolved problem still persists, namely, the reverse engineering problem – How do you optimize a weld design / parameters / geometry etc. in order to obtain a specified distortion and fatigue life?

Current efforts in weld modeling seek to take advantage of the transient full structure 3D analysis to produce a more accurate and realistic picture of the stresses that result during the welding process. The modeling process for residual stresses is described in the next section.

Modeling Process

Modeling of residual stresses and distortions combine microstructural models, thermal heat-flow models, and mechanical models to achieve a unified approach Figure 17. The most common simulations of the welding process today use coupled models where interactions between the microstructual, thermal and mechanical models are taken into account (65). A brief description of the interactions is discusses below Figure 17.

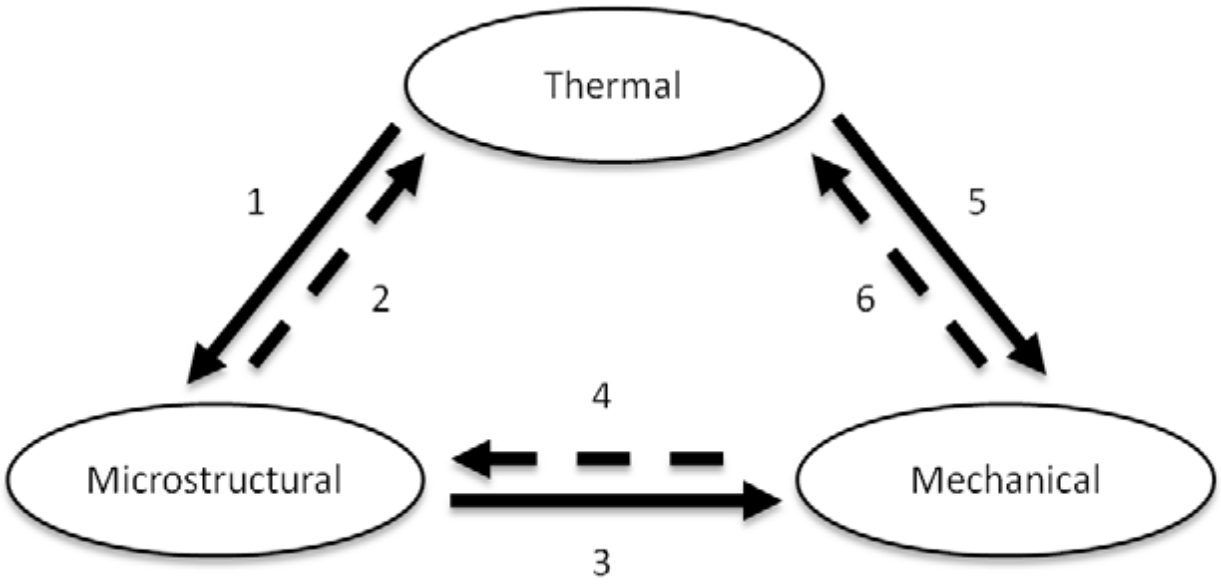

Figure 17) Drawing showing the interactions between the three areas in weld modeling.

Explanation of model interdependency:

1. The microstructual changes are driven by temperature and heating and cooling rates based on the thermodynamic driving force for phase transformations.
2. Latent heat is associated with phase transformations. Latent heat act as heat sinks and absorb energy on the heating and a source of heat by giving off energy on cooling.

3. When phase changes occur the volume of the unit cell changes due to a rearrangement in the atoms. This volume change results in a mechanical strain change.
4. Mechanical deformation can also result in a change in phase changes. An example of this is the transformation of unstable austenite to martensite due to mechanical deformation.
5. The expansion and contraction of materials due to changes in temperature also drive mechanical strains.
6. Plastic deformation caused by the thermal and microstructural changes can also generate heat which adds to the thermal load.

A simple flow chart showing the steps and models used in each step is shown in Figure 18. The first and second steps in Figure 18 account for the heating and cooling of the welded structure in the analysis. The thermal modeling involved in steps 1 and 2 is discussed further in the Thermal Modeling section. The change in temperature during welding also drives changes in the microstructure; phase transformations involved in step 3 are modeled using Kirkaldy's microstructure model, which is discussed in the Microstructure Modeling section. The microstructural changes in turn result in changes in the mechanical properties of the material (Step 4a), which need to be accounted for. The temperature changes and phase transformations also drive the development of mechanical strains (Step 4b). With the use of the adjusted mechanical properties the residual stresses can be calculated (Step 5). A discussion of the mechanical models used during each is discussed in turn below. Since the all the variables are time dependent, a transient analysis is done so this process is repeated until the temperature is at equilibrium.

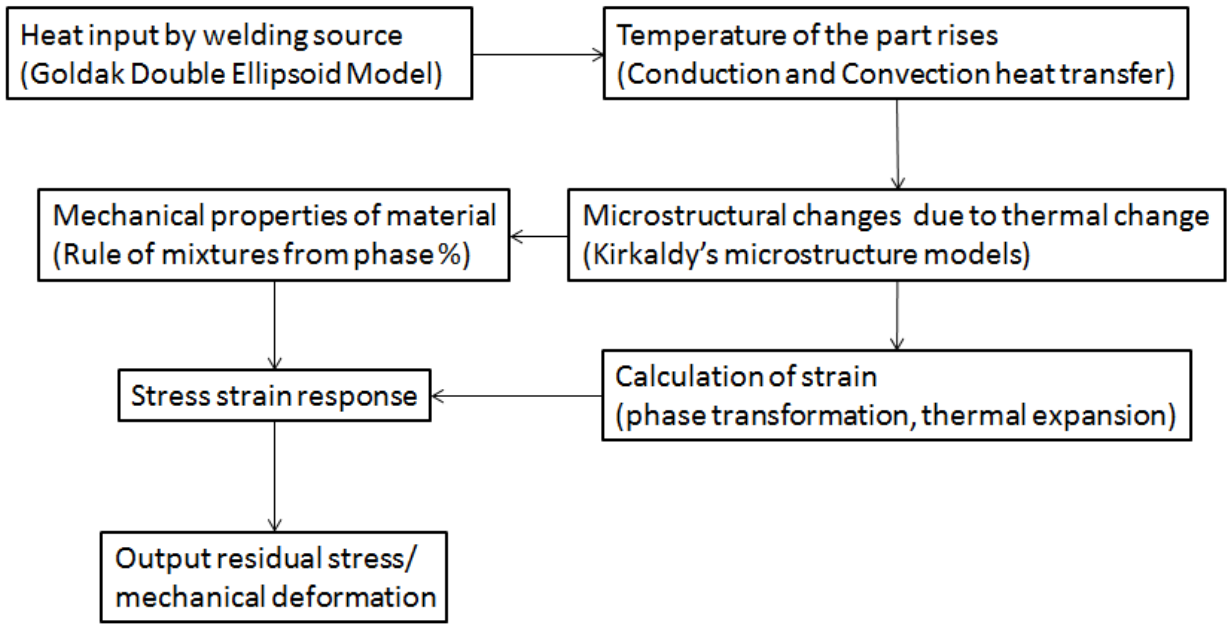

Figure 18) Flow chart showing the steps in the welding analysis used in this work.

Step 1 and 2 Thermal Modeling:

The weld modeling starts with heat input via a heating source. The heat is then dissipated into the part and the surroundings. Thermal modeling has to include both the heat source and the heat transfer.

Heat Source:

The first step in having an accurate thermal model requires having the correct heat input. This involves knowledge of the heat source, its power, and the shape and distribution of heat flow into the work piece. Depending upon which welding process is used, these three aspects of the heat source can be drastically different (66). For GMAW the most commonly used heat source fit was provided by Goldak in the 1980s (67). Goldak's model uses a double ellipsoid to represent

the weld pool shape. The typical power input for the weld pool is taken as $Q=nVI$ where Q is the total energy, n is the efficiency factor, V is the voltage and I is the current. For the typical GMAW process n is between 70 to 90% (68)

Goldak's double ellipsoidal model distributes the arc power as a Gaussian function from a radial distance from the center to the interior of the double ellipsoid (69). It is defined with 6 parameters that match six dimensions of the weld pool shape.

$$q(x,y,z,t) = \frac{6\sqrt{3Q}}{abc\pi\sqrt{\pi}} e^{-3x^2/a^2} e^{-3y^2/b^2} e^{-3[z+v(\tau-t)]^2/c^2} \qquad \text{Equation 15}$$

Where:

x,y,z = the coordinate system

t = time

Q = Heat input rate (W)

a,b,c = episode dimensional parameters (m) (See Figure 19 below)

v = velocity of the weld torch (m/s)

τ = a lag factor

The a,b,c dimensions are shown in Figure 19 (65).

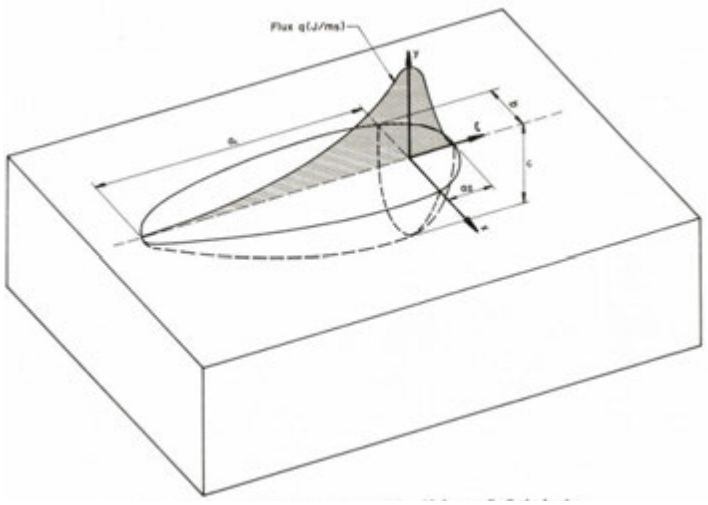

Figure 19) Drawing of the double ellipsoidal heat source.

The ellipsoid parameters can be estimated from a weld macrograph and the end of the solidified weld. Parameter b is equal to half the face of the weld and c is equal to the depth of the weld. Parameters a_2 and a_1 are the lengths of the front half of the weld pool.

The Goldak model is popular because of its ease of use and relationship to the weld pool dimensions (65), but this model does not have any relation to the welding parameters. Work continues to develop more accurate heat source models that reflect the real world welding conditions. There are a few available but these models are too computer-time intensive for industrial use in residual stress and distortion calculations.

Heat Transfer:

Once the heat is introduced through the heat input it is dissipated to thermal equilibrium through heart conduction, convection and radiation.

Conduction:

Since conduction is the movement of heat through connected particles, thermal energy equilibrates by moving it through the part from high concentration to low concentration. The basic equation for heat transfer conduction is given by equation (62):

$$c\rho\frac{dT}{dt}=\frac{d}{dx}\left(\lambda_x\frac{dT}{dx}\right)+\frac{d}{dy}\left(\lambda_y\frac{dT}{dy}\right)+\frac{d}{dz}\left(\lambda_z\frac{dT}{dz}\right)+q_3 \qquad \text{Equation 16}$$

Where:

c is the mass specific heat capacity, ($J\cdot kg^{-1}\cdot K^{-1}$)

ρ is the density of the material ($kg\cdot m^{-3}$)

λ is thermal conductivity ($J\cdot m^{-1}\cdot s^{-1}\cdot K^{-1}$)

q_3 is the volumetric density of the heat source [$W\cdot m^{-3}$]

The relationship provides the change in temperature as a function of the distance and time.

Convection:

Convection is the transfer of thermal energy from a solid substance to a surrounding liquid or gas. Convection occurs at the surfaces of the weldment and governed by:

$$q=h\cdot A_s\left(T_s-T_b\right) \qquad \text{Equation 17}$$

$$q = h\cdot A_s(T_s - T_b) \qquad \text{Equation 18}$$

Where:

A_s= surface area

T_s = surface temperature

T_b= temperature of the fluid

h=heat transfer coefficient

Radiation:

Thermal radiation is the transfer of thermal energy through the release of electromagnetic energy to the environment. This type of heat transfer is even possible in vacuum. The governing equation for thermal radiation is provided in:

$$q = \varepsilon \cdot \sigma\left(T^4 - {T_\infty}^4\right) \qquad \text{Equation 19}$$

ε =emissivity factor

σ=Stephan Boltzmann's constant

T= material temperature

T_∞=surrounding temperature

More specific details on the heat flow models can be found in references (65) (66) (68) (62).

Step 3 Microstructure Modeling and Step 4a Mechanical Properties:

It is well known that microstructural changes affect the mechanical properties of the material and also drive distortions and residual stress due to changes in phase volume. The microstructure of the heat affected zone (HAZ) plays a large role in the durability of the structure and the properties of the HAZ can vary widely depending on the composition and thermal cycle of the weld. For structural steels the microstructural phases and micro-constituents that are of interest are ferrite, pearlite, austenite, upper and lower bainite, carbide and martensite. In additional to phase constituents, grain growth in the HAZ is also of interest. A detailed discussion of modeling the microstructural changes is discussed by Akhlaghi and Goldak in reference (65).

The microstructural algorithms that are presented below show the temperature dependency of phase transitions on the chemical composition of the steel. These equations are based on the work of Kirkaldy (65) for heat treating of steel.

For high strength low alloy steels, the solidus and liquids temperatures are given by (65):

$$T_L=1530-80.581C \qquad \text{Equation 20}$$

$$T_S=1527.0-181.356C \qquad \text{Equation 21}$$

Where:

C = carbon content of the steel in weight percent

T_L = Liquidus temperature

T_S = Solidus temperature

The A_3 line on the iron carbon phase diagram is where the steel crosses into the single phase austenite region. For modeling the equation is (68):

$$A_3(°C)=912-200\sqrt{C}-15.2Ni+44.7Si+315Mo+13.1W-30Mn+11Cr+20Cu+700P-400Al-120As \qquad \text{Equation 22}$$

The pearlite start temperature is given by (65):

$$A_1(°C)=723-10.7Mn-16.9Ni+29Si+16.9Cr+290As+6.4W \qquad \text{Equation 23}$$

As the weld cools through the bainite start temperature the formation of pearlite and ferrite stop and bainite is produced. The bainite start temperature is given by (65):

$$BS(°C)=656-58C-35Mn-75Si-15Ni-34Cr-41Mo \qquad \text{Equation 24}$$

Upon rapid cooling the austenite in the weld HAZ starts to form martensite. The martensite start temperature is given by (65):

$$MS(°C)=561-474C-35Mn-17Ni-17Cr-21Mo \qquad \text{Equation 25}$$

These equations provide guidelines for what temperatures the phases start and stop, but they do not account for the cooling rate dependency. Most often time-temperature diagrams and continuous cooling diagrams are used to determine the microstructure based on cooling rate and temperature. These diagrams are not sufficient for welding due to the high temperature, so Watt and Henwood adjusted Kirkaldy's models to account for the welding conditions. The result is a set of differential equations that account for the rate dependency of the transformations. The ordinary differential equation for austenite to ferrite is (65).

$$\frac{dX}{dt}=\frac{2^{\frac{G-1}{2}}(\Delta T)^3\exp\left(-\frac{23500}{RT}\right)}{56.9Mn+1.45Ni+67.6Cr+24.4Mo}X^{\frac{2(1-X)}{3}}(1-X)^{\frac{2X}{3}} \qquad \text{Equation 26}$$

Equation 25 uses the austenite grain size, G, to account for the number of ferrite nucleation sites. The ΔT term accounts for the under cooling from the A_3 temperature which is

given in Equation 25. The exponential term provides the diffusivity of carbon in the atomic structure as a function of temperature. The denominator reflects the alloying elements role in the diffusion of carbon and finally the last term accounts for the phase fraction of the austenite and ferrite.

The equations for the bainite, pearlite, and martensite formation have the same general form as the austenite to ferrite equation and can be found on page 62 and 63 of reference (65). A more detailed discussion of modeling the microstructural changes is discussed by Grong in chapter 5 and 6 of reference (68) and by Goldak and Akhlaghi in chapter 2 and 6 of reference (65).

After the microstructure is determined the material properties can be calculated. The material properties are calculated from the microstructural model where the resulting hardness is based on the rule of mixtures of each of the phases present. The phase percent is calculated from the microstructural simulation described above.

Step 4b Mechanical modeling – Calculation of strain:

The heat input and microstructural changes described by the models above from the weld causes thermal expansion and contraction. As shown in Figure 16, the increase in temperature can lead to permanent plastic deformation, which results in residual stresses and distortions. The total strain, $\dot{\varepsilon}_{ij}^{Tot}$, is a combination of the elastic strain, $\dot{\varepsilon}_{ij}^{e}$, the plastic strain, $\dot{\varepsilon}_{ij}^{p}$, thermal strain, $\dot{\varepsilon}_{ij}^{t}$, due to thermal expansion, the creep strain, $\dot{\varepsilon}_{ij}^{c}$, and the strains associated with the phase transformation $\dot{\varepsilon}_{ij}^{Trv}$ and strain rate transformation plasticity, $\dot{\varepsilon}_{ij}^{Trp}$, described in Equation 28 (65).

$$\dot{\varepsilon}_{ij}^{Tot} = \dot{\varepsilon}_{ij}^{e} + \dot{\varepsilon}_{ij}^{p} + \dot{\varepsilon}_{ij}^{th} + \dot{\varepsilon}_{ij}^{c} + \dot{\varepsilon}_{ij}^{Trv} + \dot{\varepsilon}_{ij}^{Trp} \qquad \text{Equation 27}$$

Step 5: strain/strain response and Step 6: residual stress deformation

The amount of strain that is calculated from step 4 results in the deformation of the structure which results in the buildup in the residual stresses. The deformation and residual stresses are modeled using standard structural finite element analysis techniques that account for plasticity. An overview of this is provided by Inoue in reference (70).

CHAPTER 3: EXPERIMENTAL PROCEDURE

3.1 Sample preparation

Material Selection

The material used for the experimental portions of this dissertation was ASTM A572 grade 50 high strength low alloy steel (HSLA). The chemical composition of the material is given in Table 1, with the balance being Fe. This is a common construction material employed in the off highway vehicle market. All material was shot blasted to remove mill scale prior to any welding.

Table 1) The chemical composition of the high strength low alloy steel used for these tests.

	C	Mn	Si	S	P	V	Ti	Nb
Wt%	0.15	0.85	0.02	0.02	0.02	0.005	0.001	0.005

Welding Parameters

Weldments for the various experiments conducted in the following chapters were all initially tack welded using metal inert gas (MIG) welding. After initial tack welding continuous beads were run using a robotic welding process. The welding parameters were 33 volts, 300 amps, 20 cm/min weld speed, 8.1 m/min wire speed, and 1.32 mm diameter wire. The pulse and weave pattern were turned off on the welder. Sample preparation methods specific to each experiment conducted for this dissertation are described in the following section.

Weld Sample Preparation

Samples used to study distortion prediction and verification in Chapter 4 consisted of a single fillet welded T specimen, as shown in Figure 20. The base and stringer plates had dimensions 300 mm by 600 mm by 10 mm and 50 mm by 600 mm by 10 mm, respectively. The T

initially was tack welded in four places equally spaced along the length of the sample on both sides of the stringer; a continuous weld was then made on one side of the tacked T.

Figure 20) Photograph of the welding set up for distortion experiments.

Fatigue Samples

The large T-weld samples, shown in Figure 21, were then sectioned using a horizontal band saw made by Do-All to make the fatigue specimens. The geometry of the fatigue specimens is shown in Figure 22. A water based lubricant with rust preventer was used during cutting to limit the amount of heat input into the samples. After cutting, a 25 mm hole was drilled into the vertical leg to attach the load cell for cyclic testing.

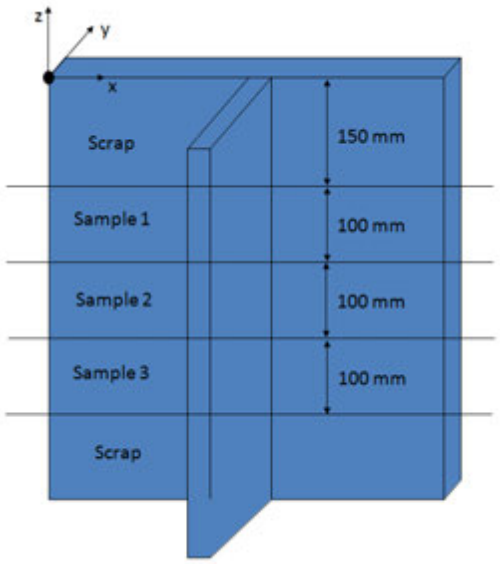

Figure 21) Sketch of the sectioning to make the fatigue specimens.

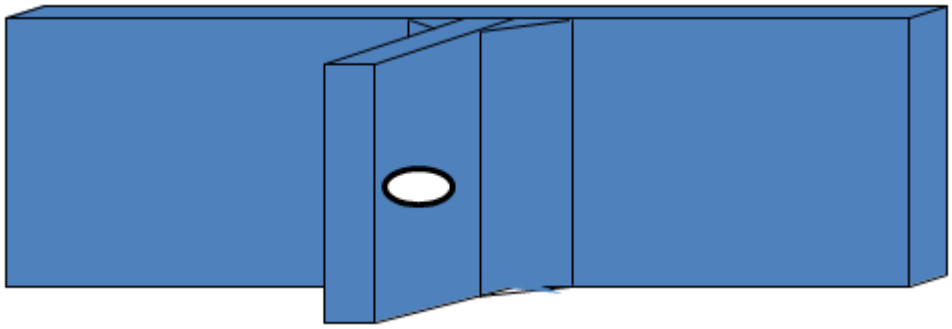

Figure 22) Sketch of the fatigue sample that was cut from the original weldment.

Metallurgical Mounts

Samples for optical examination were prepared from sections removed from the larger weldments using a Marvel bands saw. Subsequent sectioning was performed using a Struers Exotom 100 abrasive saw. All samples were mounted using a Struers Pronto-Press in a Multi-Fast mounting compound. Both macro and micro-samples were polished using a Struers Terra-polish from course sanding down to 3 micron diamond polish finish. The samples were rinsed in

water and dried with methanol between each polishing set. The macro samples were etched using a 10% concentration of nitric acid in methanol while the micro-samples were etched using a 3% concentration of nitric acid in methanol.

Macrographs of the etched structure were taken with an Epson photo-scanner. The microstructure was observed and images recorded using an Olympus PMG-3equipped with an integrated Pax-cam 3 camera and Pax-it software. A typical micrograph showing a cross-sectioned weld is shown in Figure 23.

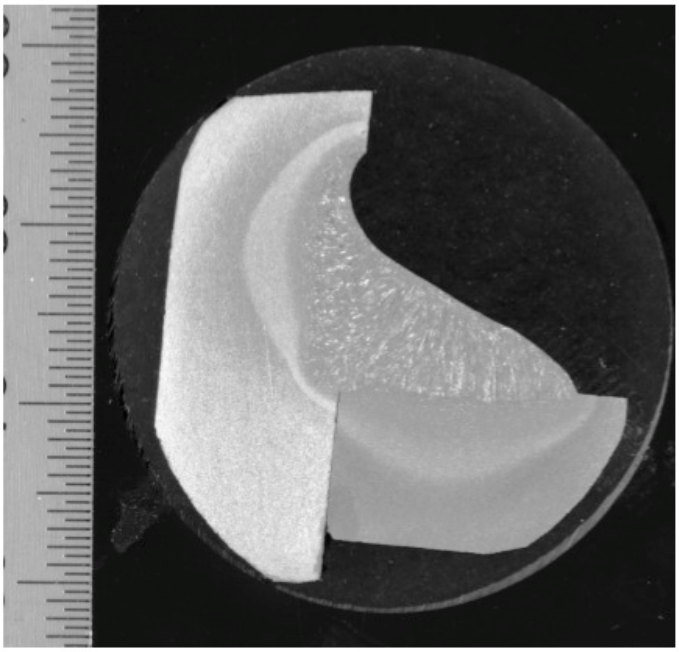

Figure 23) Macrograph of weld cross section. Each small mark on the scale on the left is 0.5 mm.

3.2 Examination and testing

Mechanical Property Measurements:

Micro-hardness data was acquired using a Struers Duramin micro-hardness tester with a 1 kg load for hard material and a 500 g load for soft material. The measurements were manually read at 400 times magnification and converted to hardness values. Rockwell C, A, and R15N macro-hardness measurements were made using a Rockwell 2000 hardness tester made by Wilson. Brinell hardness measurements were made using a J type Wilson Brinell hardness tester.

Tensile Testing was performed by Anderson Laboratories in Greendale, WI. Samples used were flat dog-bones prepared and tested to ASTM E8 specification.

Geometry Measurements:

Measurements of weld-toe geometry were made on polymer replicas made from the weld. This was done using a 2-component vinyl polysiloxane, better known as dental impression mold. The components were mixed in a one to one ratio using a static mixer. The replication procedure involved first cleaning the weld with acetone to remove any debris. The replication compound was then spread over the weld and base material and smoothed in a manner similar to the technique used in caulking. The material was then allowed to dry. Usually this required two to three minutes. Once dry, the material was peeled from the weld, providing a mirror image. An example can be seen in Figure 24.

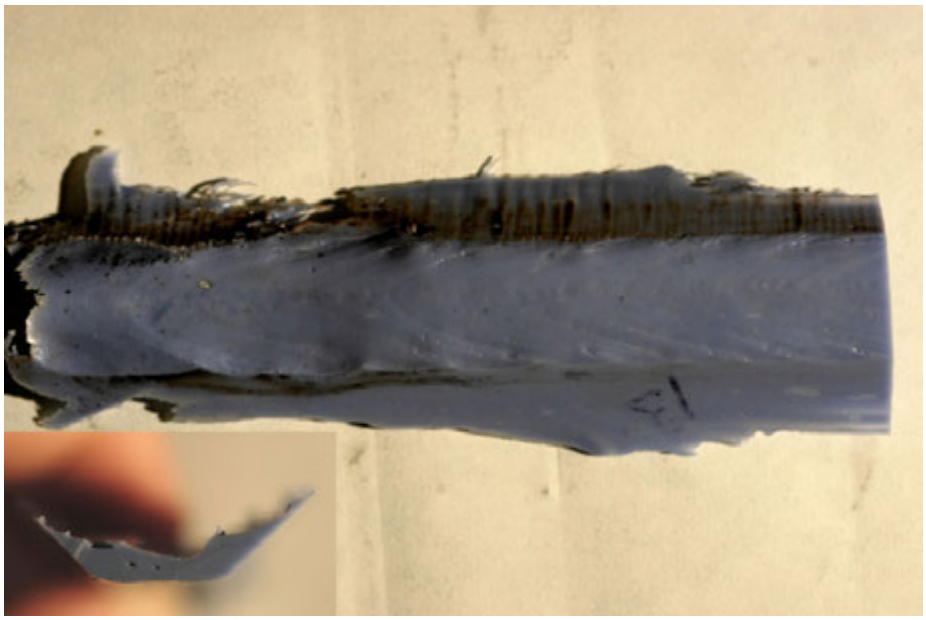

Figure 24) Example of weld mold and a cross section with the cross section in the lower left.

Once the replica was obtained, a thin section was cut from it using a razor blade. The section was cut thin so that it could be laid flat and a photograph taken. The photograph was obtained using a stereomicroscope calibrated and interfaced to the PAX-it software previously mentioned. PAX-it was then used to draw in lines to locate the base material, weld toe angles, and weld toe radii. The numerical values of these variables were then obtained from the software, exported into a spreadsheet, and then analyzed using the software Statistica and Weibul+7, both made by Reliasoft. An example of an analyzed weld is shown in Figure 25.

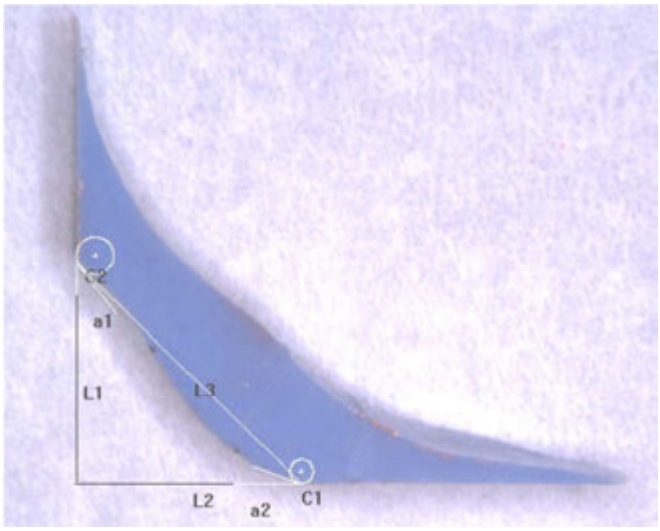

Figure 25) Analyzed weld cross section

Deformation Measurements

A GOM Aramis system was used to obtain 3D deformation measurements. The operating basis of the 3-D image correlation technology uses a combination of two-camera image correlation and photogrammetry. This system uses a pair of high-resolution digital CCD cameras to view the part. The camera bar is mounted to a tripod that can simply be placed in front of the test sample at the correct working distance. A random or regular pattern with good contrast, designed to deform along with the part, is applied to the surface of the test object and monitored using the CCD cameras. For the work of this dissertation, aluminum oxide and water slurry was applied to the surface. When dry, it provided a pattern that was resistant to the high temperatures from the welding. High intensity lighting at an oblique angle was used to overwhelm the surface radiance and maintain visibility of the oxide pattern.

Data collection involved recording a movie of the surface using the CCD cameras in real time while the part was being welded. The initial step in image processing involves defining unique correlation areas known as macro-image facets, typically 5 to 20 pixels square, across the

entire imaging area. The center of each facet is a measurement point that is tracked in each successive image with sub-pixel accuracy. Using photogrammetric principles (71), the 3D coordinates of the entire surface of the specimen can then be precisely calculated. The results are the 3D shape of the component, the 3D displacements, and the plane strain tensor.

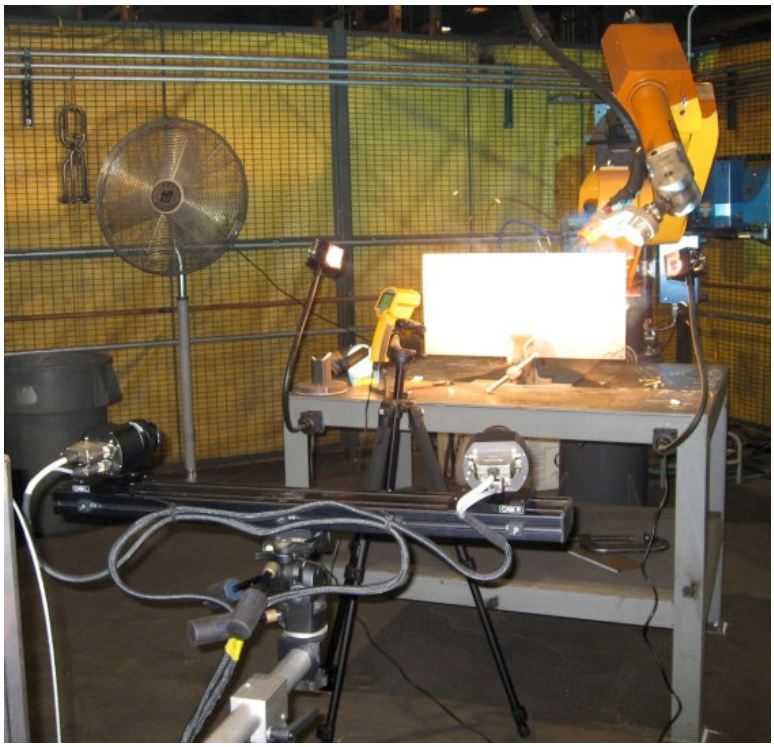

Figure 26) Photograph showing the ARAMIS camera set up. A speckle pattern was applied on the back side of the 300 mm by 600 mm plate. The temperature was measured in the middle of the HAZ as shown.

A measurement volume of 800 mm by 600 mm by 600 mm was used for this study. The system has an error of +/- 24 microns with the set up used in this experiment. Plate deformation was measured on the flat side opposite the T-weld. Approximately 3200 points were collected for each weld.

A reference sample was taken prior to welding to calibrate the system. Deformation then was measured during the entire welding process. Once the weld was completed deformation was then measured at one-second intervals until the part had cooled to below 150^{o}F on the backside of the weld location. A final measurement was taken after the piece had cooled to room temperature. This experiment was repeated on a second weld samples to understand the variability from sample to sample.

The temperature for the deformation experiments was measured using a Fluke inferred pyrometer Model 574. The instrument was placed to measure the temperature of the backside of the plate as the welding took place. Thus, the temperature recorded matched the region where the deformation was also recorded. The distance from the instrument to the work piece was optimized to have the minimum measurement area, which is 19 mm. The temperature was logged continuously during the welding / cooling process.

Fatigue Testing and Measurements

Fatigue testing was conducted using an Inston 50kN hydraulic linear actuator equipped with a 50kN load cell to apply a cyclic load to the test sample. The test set up is shown in Figure 27. The testing was controlled by an Instron 8801 controller. The tests were run in load control at an R ratio of -1. A displacement limit of +1 mm beyond the stabilized displacement was set to shut the test down when this was exceeded. This was used as a method for crack detection as well as for safety.

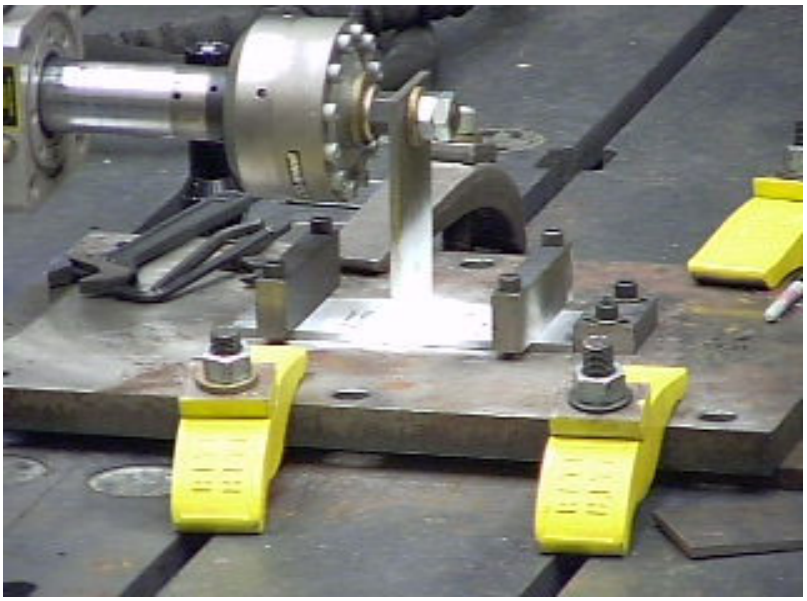

Figure 27) Photograph of the fatigue test set up.

Cracks were detected visually with a five power magnifying glass. The samples were painted with high contrast paint to aid in the visual detection of cracks. The number of cycles and the size of the crack were noted. The number of cycles was recorded when the displacement limit was triggered when the displacement of the actuator increased to 1 mm.

Residual Stress Measurement

Residual stress in the welded samples was measured using the neutron diffraction facilities at the High Flux Isotope Reactor (HFIR) of the Oak Ridge National Laboratory (ORNL) (72). Neutron diffraction was chosen because of its non-destructive nature and ability to measure the subsurface stresses without sectioning. This enabled stress to be measured on the exact same samples that were later fatigue tested. Neutron scattering experiments were carried out on the Second Generation Neutron Residual Stress Facility (NRSF2). Calibration of the diffractometer and the

position-sensitive detectors were accomplished using a series of powder standards (73) (74). The goniometer and data collection are controlled by Labview-based software (75).

A laser alignment system on NRSF2 was used that provided rapid and precise alignment and positioning of the neutron beam at the same location when acquiring data, no matter the sample orientation (76) (77). The samples were mounted on an automated X-Y-Z translation table and the surfaces of the specimen were initially located with transit-levels and then referenced to the translation table coordinates though the system software. More sample alignment details can be found in reference (78).

The sampling gauge volume for the measurements was defined by the intersection of the projections of the incident and receiving slits (Figure 29). The gauge volumes for stresses measured in the X and Y direction was 2 mm by 2 mm x 20 mm where the gauge volume in the Z direction was 2 mm by 2 mm by 2 mm. The locations of the measurements are show in Figure 28.

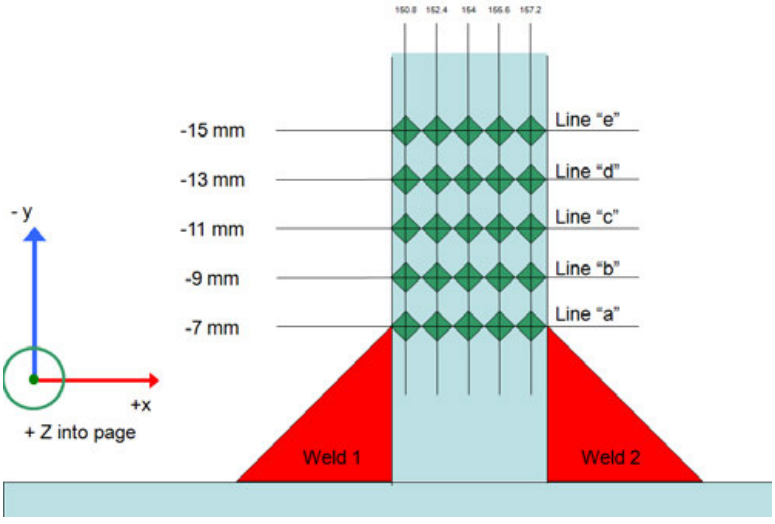

Figure 28) Drawing showing the location of the residual stress measurements.

Reference bars for the neutron measurements were electro-discharge machined (EDM) from the base material and taken to have zero stress. The reference bar dimensions were 4 x 25 x 4 mm. The bar was affixed to the sample and rescanned periodically throughout data collection to both provide the stress-free interplanar spacing, d_0, and as an experimental check. The sampling volumes were the same as those of the sample in each particular measurement direction.

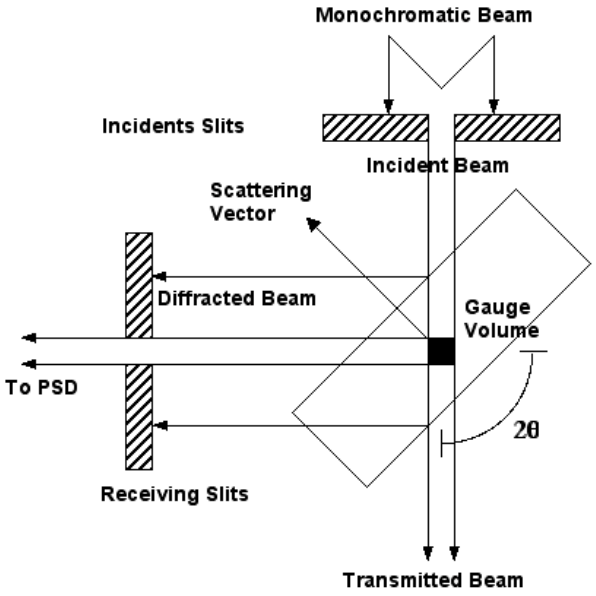

Figure 29) Schematic of the neutron diffraction method, showing the gauge volume cross section as defined by the slits (shown at 90 degree for convenience). The measured strain component is in along the scattering vector direction.

The residual stresses were measured from the T-welds both prior to and after making the fatigue samples. Three locations were measured corresponding to the center of each of the three fatigue samples shown in Figure 21.

3.3 Weld modeling procedure

Much of the text from this section was taken directly from the paper titled "Analytical and experimental validation of residual stresses using state-of-the-art techniques" by Johnson et.al. (79).

Welding Process was simulated using a weld computational mechanics program called VrWeld from the Goldak Technologies Inc. VrWeld allows the designer to model the transient three dimensional temperature field, the evolution of microstructure in the weld, the transient 3D displacement, and finally the stress and strain in the structure. Inputs for the simulation include stereo-lithographic (STL) files for the parts being welded, the set of weld procedures and the weld path for each joint, and material properties for the materials welded and the boundary conditions (80) For thermal analysis the boundary conditions were chosen from prescribed temperatures, prescribed power density, prescribed thermal fluxes and convection cooling applied during the welding process (80). Microstructure was modeled using the algorithms described in Watt et al (81) and Henwood et al (82). For stress analysis, the boundary conditions were prescribed displacement constraints (vice and tack welds) Goldak et al (80).

VrWeld solves the coupled equations for the conservation of energy, mass and momentum for a structure being welded (80) . Complex equations are solved by using the mathematics of transient non-linear FEM and the evolution of microstructure. The accuracy of the solution computed by VrWeld for the thermal stress analysis of a weld in a welded structure depends on how accurate the following data is specified:

Geometry

The geometry of the structure is defined by STL files exported from a CAD system. The geometry of the weld joint and filler metal are described separately or can be imported if available as STL files. In the present simulation, welds were modeled as triangular fillet weld.

Material Properties

The material property parameters used in the thermal solver, microstructure solver and thermal-stress solver and the composition of each material are specified in the Material Library. For low alloy steels, the properties of each of the phases, i.e., alpha or ferrite, pearlite, gamma or austenite, bainite and martensite for each high strength low alloy steel are used. The temperature dependent thermal conductivity, the specific enthalpy for each phase is specified. The specific heat is the rate of change of the specific enthalpy with respect to temperature. It can be computed from the temperature dependent specific enthalpy. All these temperature dependent material properties were given as input for the present simulation.

Process Parameters

The process parameters for each weld are stored in the weld procedure. They include the welding current, voltage, arc efficiency, wire diameter and wire speed and the power density distribution in the weld pool region. The start time for each weld pass, the welding speed and the weld path are stored in each weld joint.

FEA Mesh

The quality of the mesh is important. Finer meshes are expected to be more accurate if the FEA problems are solved with sufficient accuracy. However, meshes that are too fine can be ill-conditioned which means that they are more difficult to solve accurately. Also finer meshes take longer to solve. It is usually a good strategy to do the analysis first with a very coarse mesh. Then repeat the analysis with a finer mesh until the change in the solution is sufficiently small. At each stage one can also visualize the element error that shows where refining the mesh would provide the largest gain in accuracy. Often the first coarse mesh is sufficiently accurate over significant regions and the mesh only needs to be refined in a few local regions to achieve greater accuracy. Figure 30 shows the finite element model for the welded structure used in this work.

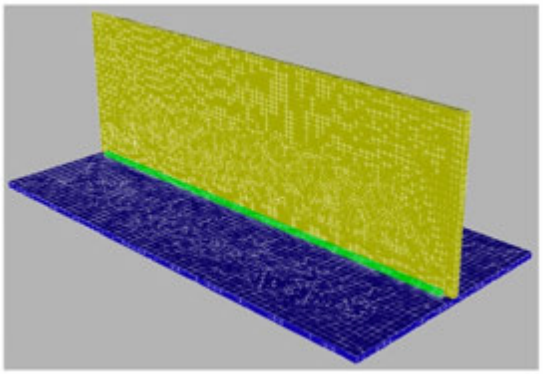

Figure 30: Finite element model of welded joint build up using VrWeld.

Boundary Conditions

Boundary conditions includes fixtures that prescribe or constrain displacements, this also include tack welds or applied forces. Boundary conditions are time dependent. Figure 31, shows how the tack welds were applied for weld simulation of the sample used in this work.

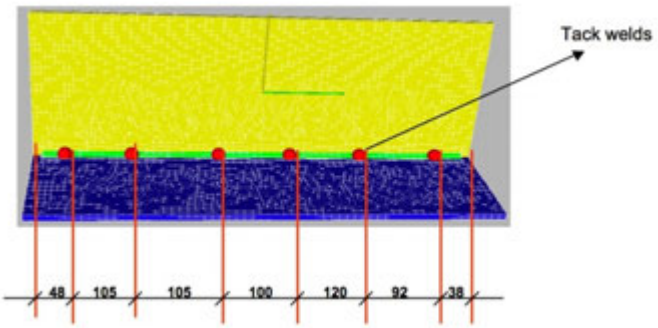

Figure 31: Tack welds modeled at the same locations as in experimental tests.

Heat Source Model Parameters for Arc Welds

The heat source model parameters for arc welding typically include: arc current in amperes, I, arc voltage, V, and arc power efficiency. For MIG welds, wire speed and wire diameter are included. The first objective in doing a thermal analysis of an arc weld is to obtain an accurate model of the weld pool and heat-affected-zone (HAZ). Goldak's double ellipsoid weld pool model (65) distributes the arc power as a truncated Gaussian function of the radial distance in the interior of a double ellipsoid. The front half of the ellipsoid has length a1, width b1 and depth c1. The rear half of the ellipsoid has length a2, width b2 and depth c2. Along any radial line from the centroid of the ellipsoid, the power density varies as a truncated Gaussian function. With this power density distribution, the FEM energy solver computes the nodal thermal power for all elements that intersect the double ellipsoid. It then scales or constrains this total thermal power to be equal to the arc power.

Refer to flow chart in Figure 32, which summarizes the steps for carrying out welding simulation process in VrWeld (83).

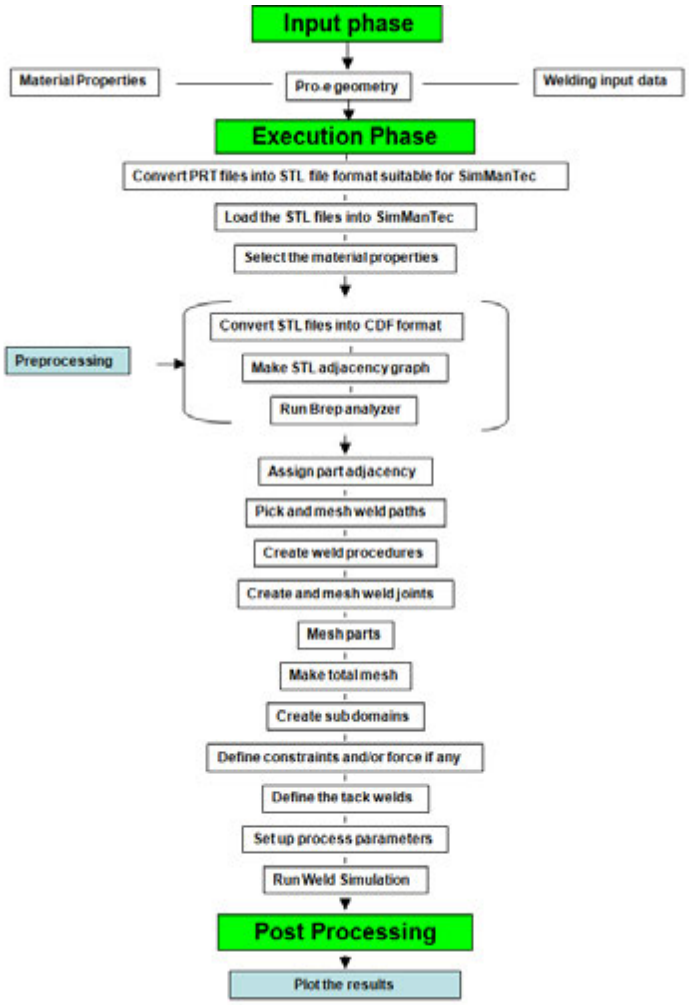

Figure 32) VrWeld process flow for analysis set up**.**

Structural Modeling:

The FEA structural modeling of the welded joint was done to determine the stresses that occur from testing. The stresses from the FEA are used to calculate the peak stress which is used in the fatigue life prediction. The FEA software package used for the analysis was ANSYS. The FEA model was made using Hypermesh by Altair.

The part was modeled using linear elastic brick elements. The model had 4 elements through the thickness to capture the stress gradient. A schematic of the mesh near the weld is

shown in Figure 33. The elements were second order brick element and were approximately 2 mm in size. The auto meshing feature was used to build the model so the element size was optimized by the software for mesh quality to provide the best stress analysis results.

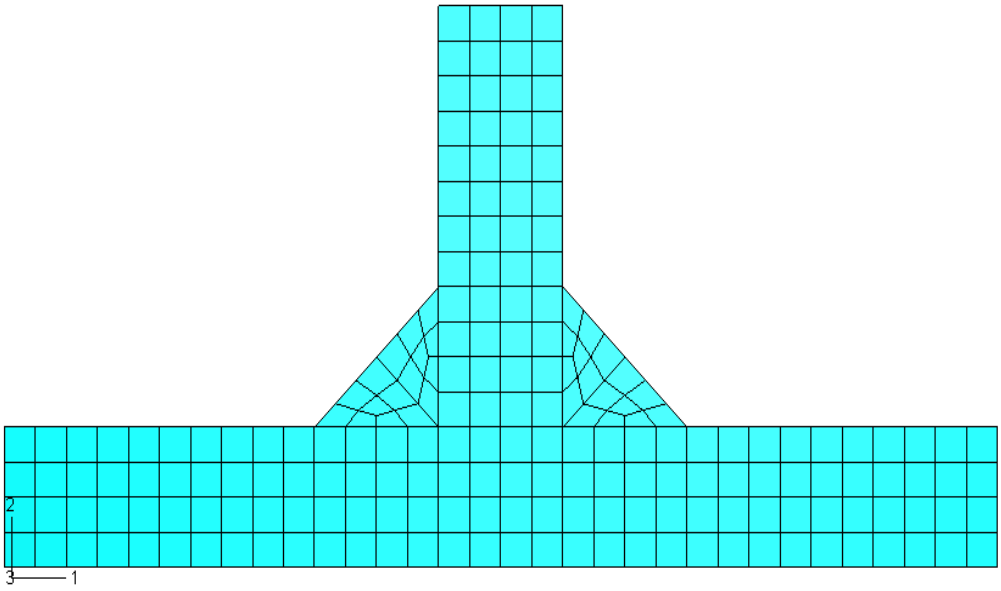

Figure 33) Section of the FEA mesh for the double fillet t weld.

The nodes in the FEA mesh that correspond to the location of the clamps were fixed to limit motion in the x, y and z directions. A load of 1000N was applied evenly to the nodes that surrounded the through hole where the test load is applied as shown in Figure 34.

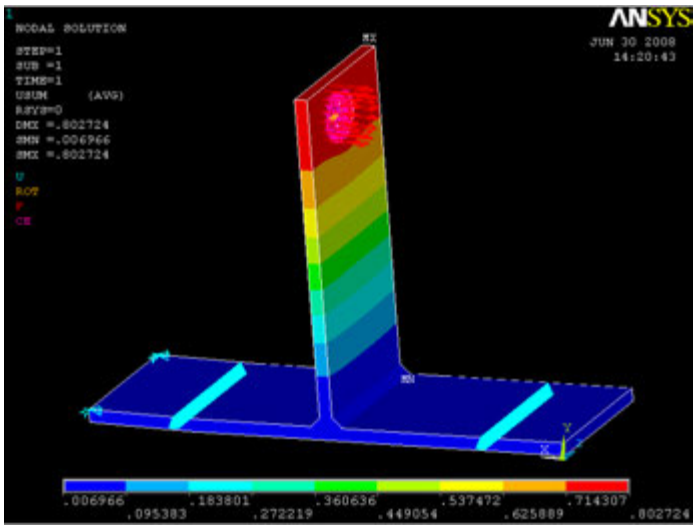

Figure 34) FEA model showing the displacement results. The clamps are modeled as restraining movement in the x and y direction. Fixities on the corners are placed to eliminate ridged body motion.

CHAPTER 4: ANALYTICAL AND EXPERIMENTAL VALIDATION OF DISTORTION USING STATE OF THE ART TECHNIQUES

4.1 Introduction

In order to understand the effectiveness and accuracy of welding simulation the distortion in a simple T-welded sample was evaluated. The distortion measurement was performed using 3D image correlation which allowed for full field measurements of the 300 by 600 mm sample during the welding process. In concert with the measurements, welding simulation was performed using VrWeld, a commercially available welding simulation software package, to predict the distortion resulting from welding. First a visual comparison is used to evaluate the distortion in a qualitative manner. A quantitative evaluation of the large datasets from both measurement and simulation is performed using the L2 error method of comparison. The L2 error method compares the deviation of two sets of vectors. In this case the vectors are the total displacement. The first comparison made is between two welded samples. This is used as a baseline to compare the deviation between experimental and simulation results. Using this methodology the welding current is evaluated to understand the effect it has on the simulation as it compares to the test data.

4.2 Experimental procedure

The welding process details are described in section 3.1. The weld legs were uneven with a 12 mm leg on the stringer and an 8 mm leg on the plate side. A cross section of the weld is shown in Figure 23. A typical weld like this would be made using pulsed arc and a pattern weave to ensure equal leg lengths. This was purposely not included because the capability to capture the weave and pulse are not easily done in the computational simulation. An inferred thermometer

was used to measure the temperature as a function of time. The temperature was later used to calibrate the convection coefficients for cooling.

The distortion measurements were made using an ARAMIS 3D image correlation system made by GOM. The system uses a random pattern imprinted on the specimen to track the movement of predefined area called a facet. Each facet is approximately 10 mm by 10 mm and the facets are over lapped by 3 mm. A facet represents a measurement of a single area. The total displacement is made up of the combination of all of the measurement facets. The measurements were taken on the backside of the T specimen geometry as shown in Figure 35b. The total number of facets or measurement points was 3200 across the 300 by 600 mm back plate. An area measurement was taken every second for 1000 seconds. One time interval is referred to as a measurement time step. For reference, the speckle pattern is shown in Figure 35a.

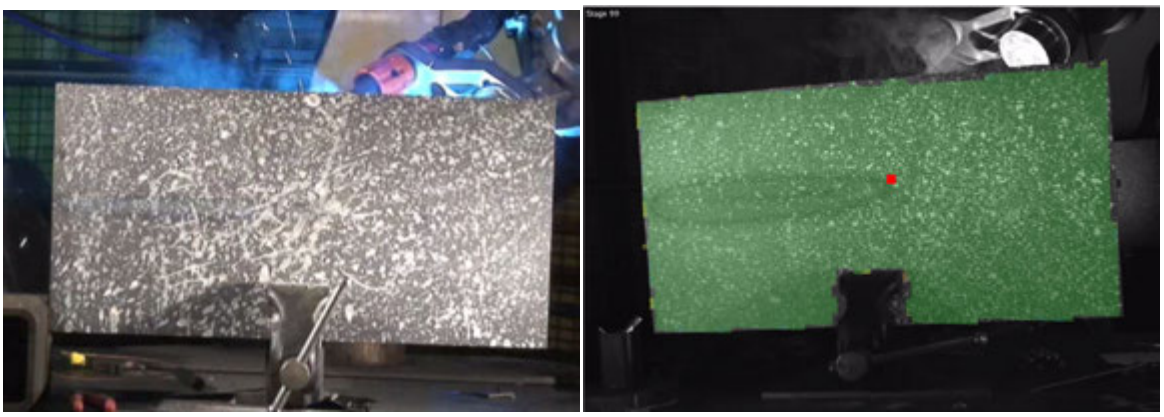

a) b)

Figure 35) a) Photograph showing the speckle pattern b) The green area on the back side of the plate indicates the measurement area.

Two samples were welded and measured for later comparison. The total number of experimental data points collected for each sample was 3.2 million. At each facet the x, y and z

position was measured. A local coordinate system was chosen that could be easily reproduced in the simulation. Since the initial steel plate was not perfectly flat, a best fit plane was established through the initial x,y,z coordinates of the back side plate. The bottom left corner of the plate was established as the origin. The displacement, $(\bar{x}, \bar{y}, and\ \bar{z})$, of each facet point at each time step was calculated by:

$$\bar{x} = x_i - x_o \qquad \text{Equation 28}$$

$$\bar{y} = y_i - y_o \qquad \text{Equation 29}$$

$$\bar{z} = z_i - z_o \qquad \text{Equation 30}$$

Where, x_i,is the measured coordinate and, x_o, is the initial coordinate.

The welding simulation was run with VrWeld. The geometry of the part was imported as an STL file, a common file type that represents the geometry using a set of triangles. The welding speed and direction is input along with the clamping conditions that match the experimental fixture. The BAB-Anderson material properties for a high strength low alloy steel from the VrWeld material database were used. The convection coefficients were developed from the experimental measurement data using the procedure by Goyal (83).

4.3 Results

Qualitative Representation

Displacements in individual directions are difficult to compare since there are so much data. To visualize the displacements to make for easier interpretation the total displacement, *u*, was calculated by:

$$u = \sqrt{\bar{x}^2 + \bar{y}^2 + \bar{z}^2} \qquad \text{Equation 31}$$

This technique was used on both the simulation and measurement data. The contour plots shown in Figure 36 through 38 are graphical representations of the total displacement field of the back plate for both the simulation and measured displacement. The measurement data is filtered using by averaging the nearest points. This technique filters the noise from the system and provides a better data set for analysis. Selected contours matching the time step for the measured data are shown for comparison. The displacement is magnified 30 times to show the deformation pattern.

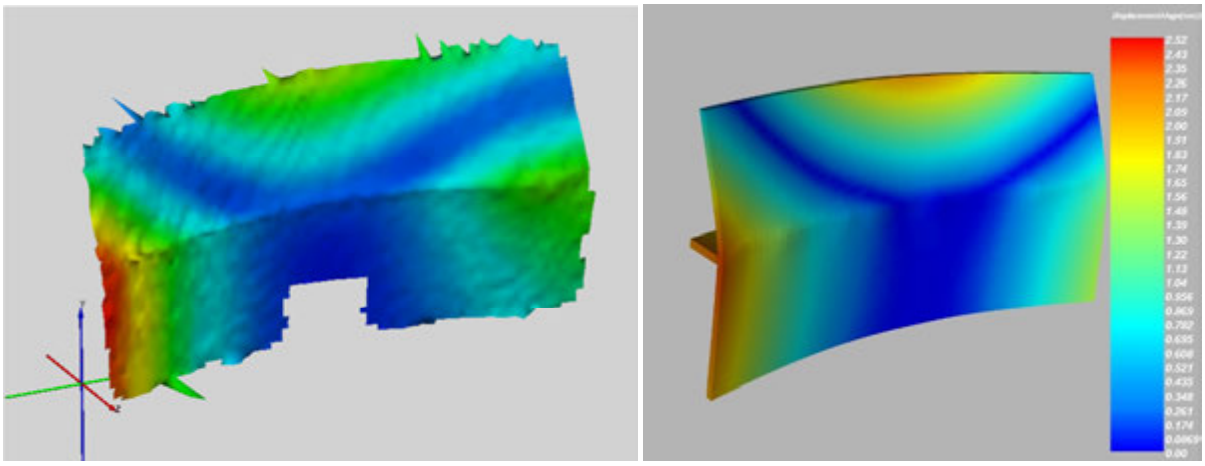

Figure 36) a) Experimental deformation data after the weld stopped at t =176 sec. b) Corresponding simulation results

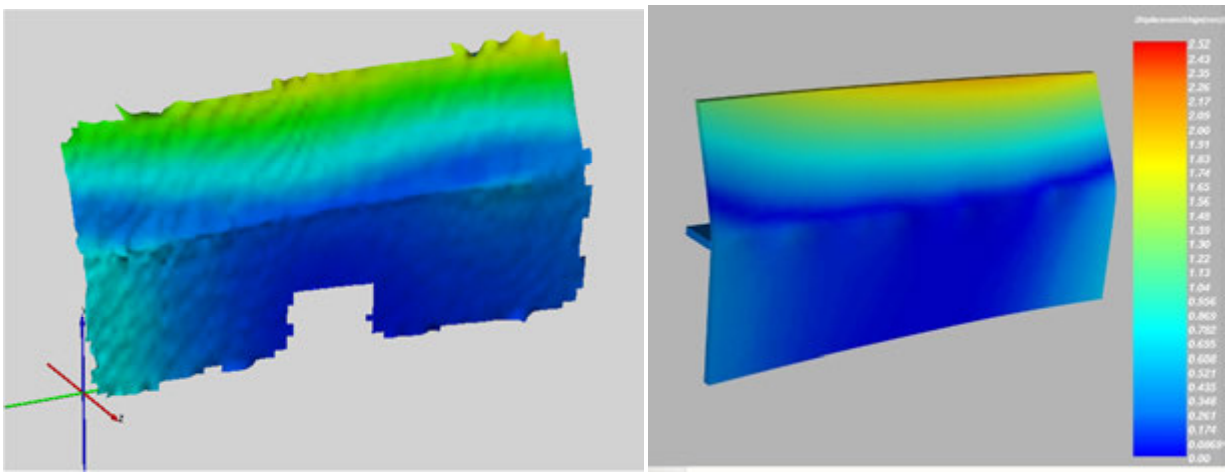

Figure 37) a) Experimental data at t=400 sec. b) Corresponding simulation results

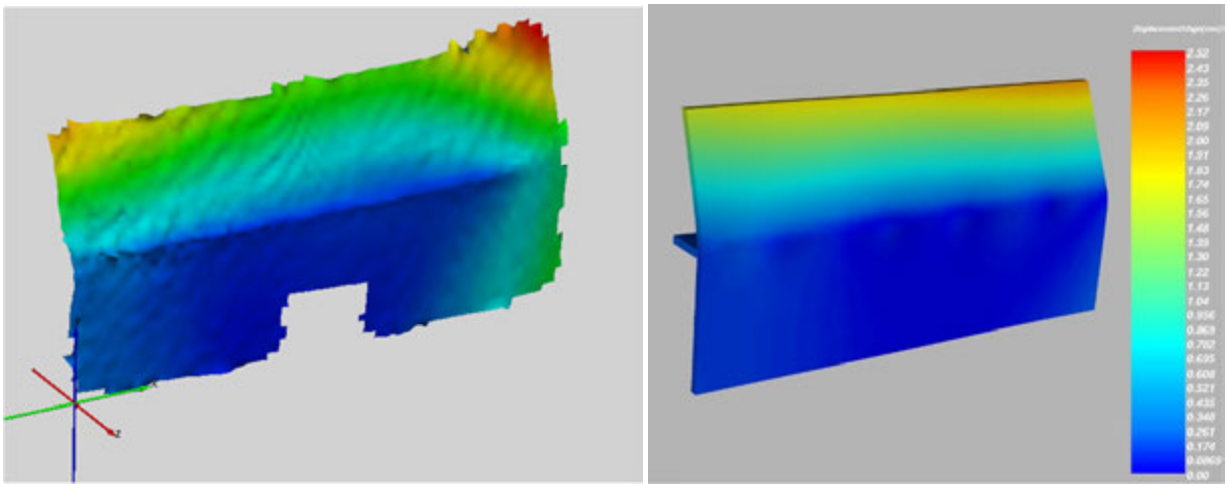

Figure 38) a) Experimental data at t = 1000 sec after sample was released from the clamps. b) Corresponding simulation results

L2 Norm Deviation Calculations

The deviation in L2 norm is an ideal method of comparing large data sets. Here it is used to compare the computed and measured values to see the total deviation of the displacement fields. The three dimensional displacement vector at the grid points i is denoted u_i. For each time step the L2 norm for the n data points was evaluated for the difference between the computed

and experimentally measured displacement vectors. The value of the L2 norm is given by the following equation:

$$\|e\|_{L2} = \sqrt{\sum_{i=1}^{n} \left(u_{i_{computed}} - u_{i_{measured}}\right)^2} \qquad \text{Equation 32}$$

Equation 32 uses the total displacement for the computed and measured displacement to calculate L2 norm. In order for the above equation to be used effectively, the experimental and simulation data is set in an identical coordinate system. The difference in displacements between experimental data and computed data for each time step is then computed, and the contribution to the L2 norm was evaluated. The plots are made with the L2 norm difference versus time shown in Figure 39. The curve labeled Sample1 in Figure 39 is the L2 norm between the first and second experimental test. The data for three different welding currents, 330 Amps, 300 Amps and 270 Amps is shown.

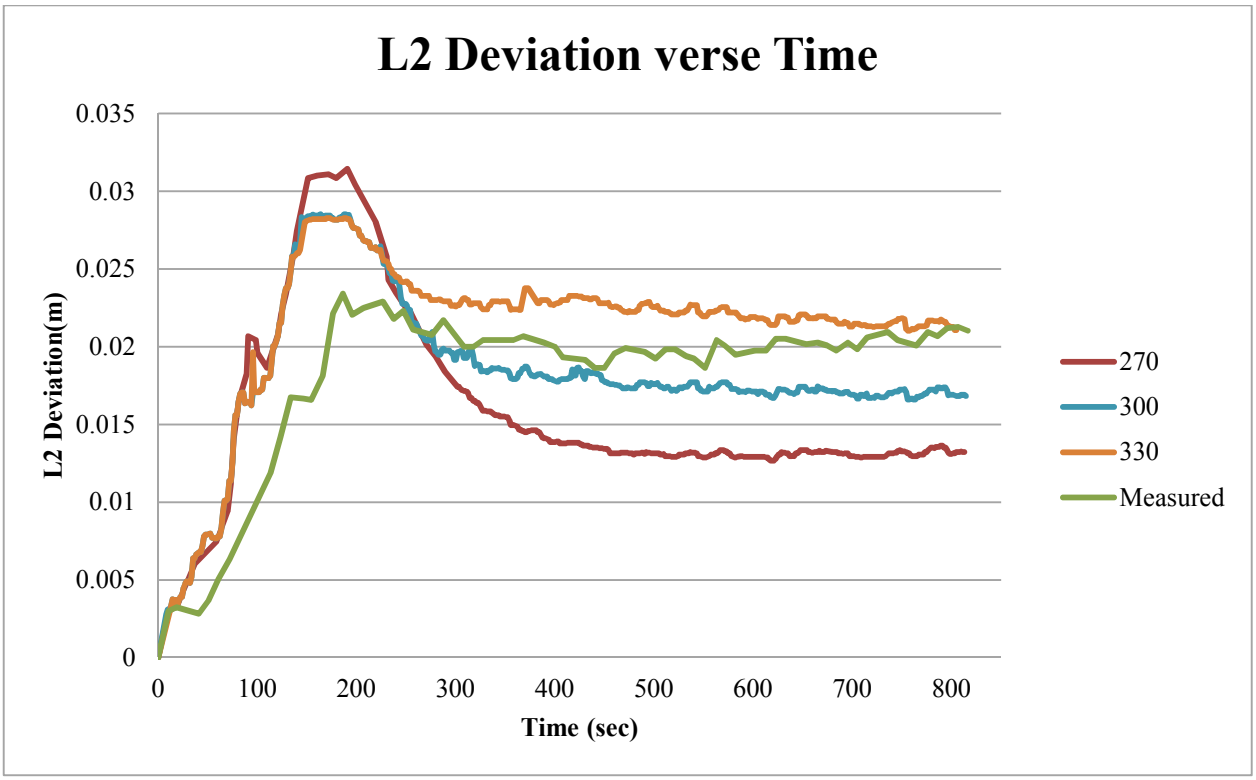

Figure 39) Graph showing the L2 norm deviation as a function of time for different welding currents. Sample1 is the deviation between two experimental runs.

The difference in displacements between experimental data and computed data for each time step was then computed, and the contribution to the L2 norm was evaluated. The plots are then made with the L2 norm deviation versus time.

4.4 Discussion

Qualitative Comparison

A general comparison of the experimental and simulation deformation can be done by a comparison of the contour plot. This type of comparison provides a general overview of the magnitude and shape of the deformation. From the comparison of the experimental contour plots to calculated simulations, it can be seen that the general shape and magnitude of the

prediction matches the experimental data very well. Figure 36 shows that at the time the welding stopped, 174 seconds after the start, the deformation pattern matches very well with a maximum displacement of 2.52 mm for the measurement and 2.30 mm for simulation. The shape of the deformation pattern shows the same trend and the magnitude of the distortion matches well. At 400 seconds after the start of the weld, Figure 37, the deformation pattern still matches very well with the simulation showing slightly more total deformation for 2.10 compared to the measurement of 1.82 mm. The final comparison at 1000 seconds, after the sample had cooled enough where no more deformation would occur, the patter has very good correlation between the simulation and measurement results. The measurement shows slightly more deformation with a maximum total deformation of 2.52 in the top corner of the plate where the simulation had a maximum deformation of 2.23 mm. It is difficult to draw quantitative conclusions from the comparison of deformation plots. For this reason a more quantitative approach that utilized all the data collected is shown in the L2 Norm Deviation Calculation section.

L2 Norm Deviation Calculations

The closer the L2 norm is to 0 in Figure 39, the less deviation there is from the first experiment. The first thing to notice is that even between the first and second experimental data there is deviation. This provides a baseline and shows the accuracy of the experiment by looking at the repeatability of the experimental results. A deviation between two welded samples is not unexpected due to natural variations in the process and material which are impossible to replicate. This does show that the deviation from sample to sample needs to be considered when evaluation of simulation models.

When comparing the curves for the various welding currents used in the simulation in Figure 39, it can be seen that as the power decreases, the simulation results have lower deviation from the experimental results. This data the total power input has a significant effect on the total distortion.

The maximum deviation for all cases is when the welding has just ended. This occurs here because this is where the maximum distortion occurs. In practice the distortion at the end when the weld has cooled to room temperature is of most concern. When looking at the last time step, the minimum deviation from the first experimental sample is lowest with the lower current.

4.5 Conclusions

The 3D image correlation was successfully used to capture full field transient displacements of a welded sample. The full field data was used to compare computational weld modeling results to experimental data for a quick validation of the distortion predictions. The comparison showed that the welding simulation matched the measured distortion quite well.

A more detailed validation of the weld models was also demonstrated by comparing the deviation between measured and experimental data using the L2 norm. The technique outlined in this paper can be used to understand the sensitivity of the input data. This was demonstrated by evaluating the sensitivity of the weld model to welding current. Further analysis could provide an understanding of the effect of each of the welding parameters has on the distortion. A sensitivity analysis could be performed and the results could be used for process control to minimize the distortion.

The importance of looking at the repeatability of the in the experimental data was also demonstrated in this experiment. The variation in the experimental measurements provided a

baseline for which the simulation can be evaluated. The consideration in the accuracy of the experiment is needed when models of complex phenomenon are being validated.

CHAPTER 5: VALIDATION OF RESIDUAL STRESSES USING NEUTRON DIFFRACTION TECHNIQUES

5.1 Introduction

Residual stresses come about in the welding process due to changes that occur due to the localized heating and cooling of the weld and HAZ. Measurements of these residual stresses are expensive and time consuming. For that reason modeling of residual stresses needs to be evaluated. The residual stresses are important because they have a significant effect on the durability of welded structures.

In order to use the residual stresses from welding simulation the overall accuracy of the prediction needs to be determined. To accomplish this, a detailed analysis comparing the residual stress predictions from VrWeld and experimental residual stress measurements from neutron diffraction is completed.

5.2 Experimental procedure

Experimental details are given in section 3.1. Included below are details specific to this experiment.

Welding of Sample

The samples used for the residual stress validation are shown schematically in Figure 40.

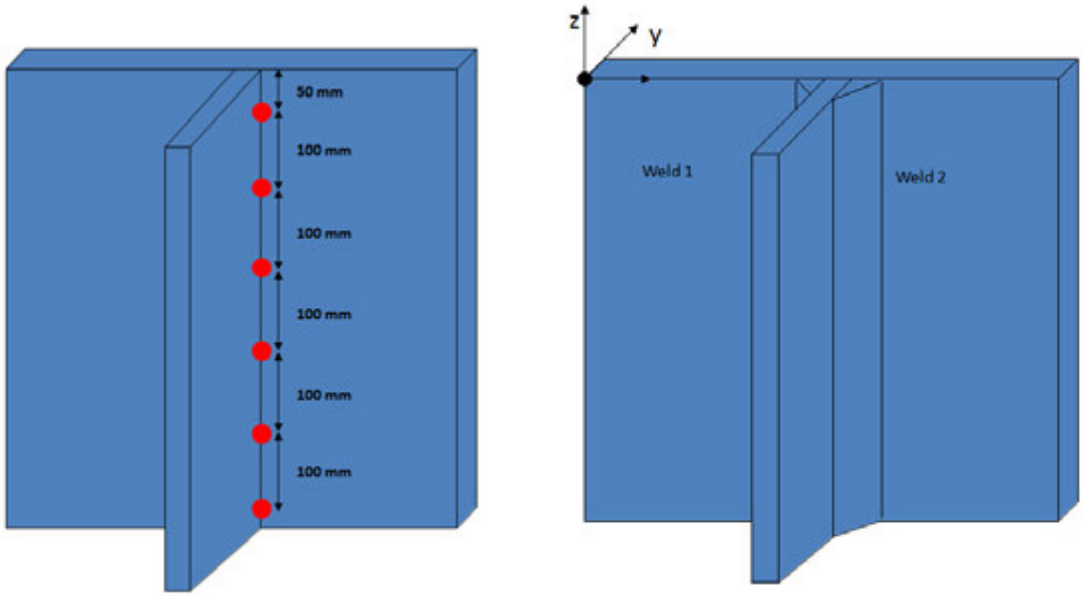

Figure 40) Schematic of the welded sample. A) initial tack welding. B) final structure.

The base and stringer plates consisted of two ASTM A572 steel grade 50 steel plates with dimensions 305mm by 610 mm by 8 mm welded together to form a T. The T was tack welded in six locations along the length of the sample on both sides of the stringer as shown in Figure 40. The tack welds were not precisely placed so the actual locations of the tack welds were accounted for in subsequent simulations (see discussion in Section 3.3).

After laying down a continuous bead on one side of the T, the sample was rotated and the process repeated in order to make the second weld. The process for each sample was video recorded to accurately account for the time dependency of the clamping conditions which are used to model the boundary conditions in the welding simulation.

Residual Stress Measurement:

Macro-residual strain is determined from the shift in the interplanar spacing of the lattice planes within the diffracting grains relative to the interplanar spacing of a strain-free reference sample. The measured strain is an average of the strains in a large number of grains within the sampling volume. Bragg's law (84) relates the angular location of the diffraction peak determined in the scattering measurement to the interplanar spacing, d, by:

$$d_{hkl} = \frac{\lambda}{2 \cdot sin\Theta_{hkl}} \qquad \text{Equation 33}$$

where λ is the wavelength of the neutrons (1.73 Å) and θ_{hkl} is half the scattering angle for a diffraction peak corresponding to the crystallographic Miller indices *h,k,l*. The 211 ferritic iron peak was located at around 95.4° 2θ and used in this study. In the post data collection the data were processed for peak position and intensity using Labview-based software. The residual strain component is related to the shift in interplanar spacing by:

$$\varepsilon_{elastic} = \frac{(d_{hkl} - d_{0\ hkl})}{d_{0\ hkl}} \qquad \text{Equation 34}$$

where $d_{0\ hkl}$ is the interplanar spacing of the stress-free reference. In order to calculate the full strain tensor at least six independent measurements are needed. If the shear stresses are assumed to be zero, then only three orthogonal strain measurements are needed. Hooke's law is used to then transform the strain measurements to residual stresses by: (85)

$$\sigma_{11} = \frac{E}{(1-\upsilon)(1-2\cdot\upsilon)} \times [(1-\upsilon)\varepsilon_{11} + \upsilon\,(\varepsilon_{22} + \varepsilon_{33})] \qquad \text{Equation 35}$$

$$\sigma_{22} = \frac{E}{(1-\upsilon)(1-2\cdot\upsilon)} \times [(1-\upsilon)\varepsilon_{22} + (\varepsilon_{11} + \varepsilon_{33})] \qquad \text{Equation 36}$$

$$\sigma_{33} = \frac{E}{(1-\upsilon)(1-2\cdot\upsilon)} \times [(1-\upsilon)\varepsilon_{33} + \upsilon\,(\varepsilon_{11} + \varepsilon_{22})] \qquad \text{Equation 37}$$

where E is the Young's modulus (205,000 MPa), υ is the Possion's ratio (0.27) and ε_{11}, ε_{22}, ε_{33} are the strain measurements (Equation 34).

The measurements were made in three locations along the weld on a sample designated as A13C-23. The first measurement location was made 205 mm from the top of the sample. This location is referred to as "A13C-23-1." The second measurement was made at 305 mm from the end of the sample and this location is designated as "A13C-23-2". A third measurement location was measured 405 mm from the end of the weld and this location was designated "A13C-23-3". The location is marked on Figure 41.

For each location multiple residual stresses were measured. The stresses were measured on the vertical plate in 2 mm increments from the toe of the weld up to 8 mm away. Through the plate thickness, the measurements were taken 1.6 mm from each other starting at 0.8 mm from the edge. The locations of the measurements are shown in Figure 42. In order to calculate the residual stress three strain directions must be measured as shown by the equations noted in Section 3.2 Residual Stress Measurement. The strain in the x and y direction could be directly measured in the required locations, but due to the sample geometry and diffractometer set up the strain in the z direction could not be measured in the same locations. In order to overcome this,

the measurements were conducted 45 mm from the end of the specimen. This was the furthest from the end of the sample the measurement could be made.

The strain is averaged over the gauge volume in the measurements. For comparison the simulated residual stresses were also averaged in the x direction to match the measurement gauge volume.

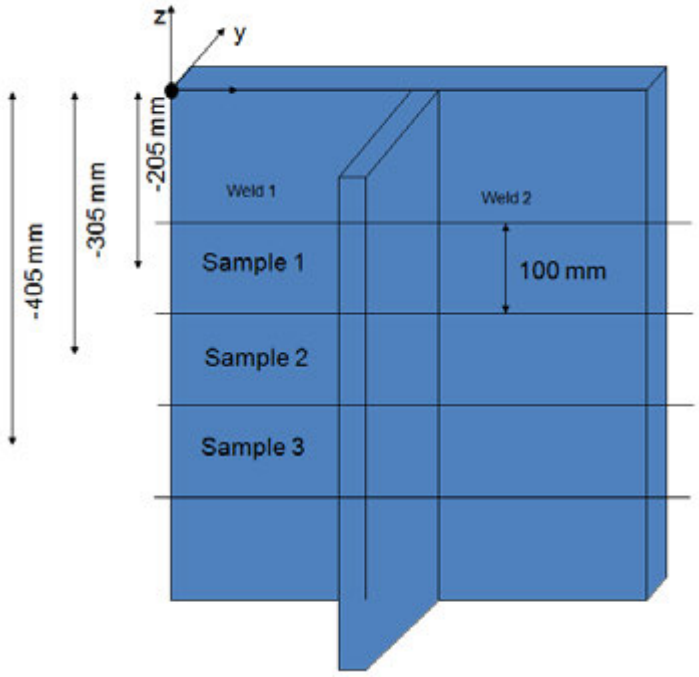

Figure 41) Sketch showing the three measurement locations.

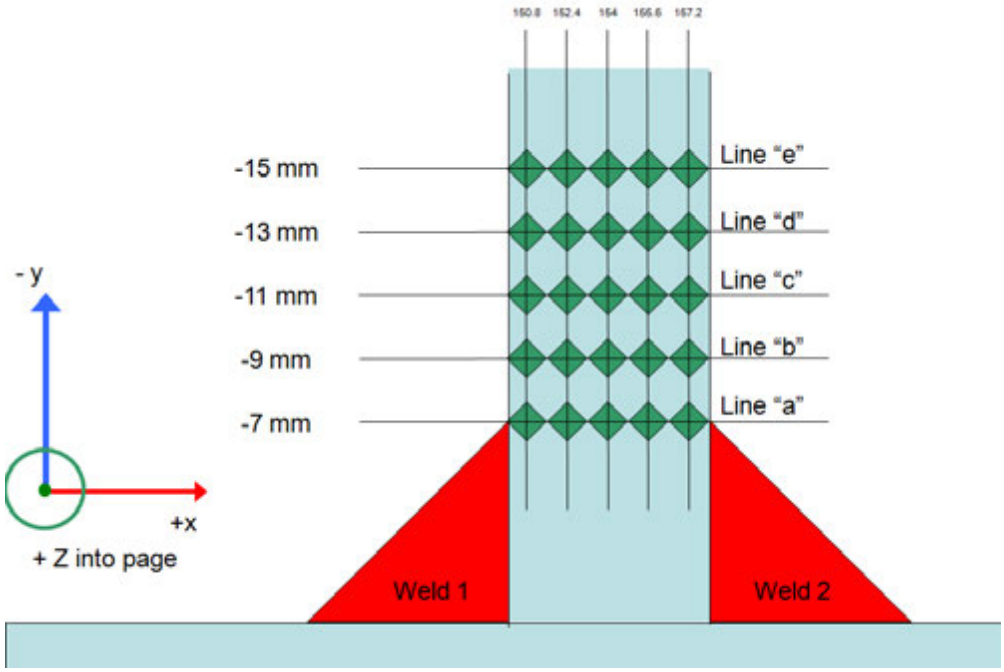

Figure 42) Sketch showing the location of the residual stress measurements.

Welding Simulation Procedure:

As stated in Section 3.1 welding simulation was performed using VrWeld, a commercial welding simulation software package. The input parameters include the geometry of the part to be welded, the parameters of the weld process (heat input, temperature dependent material properties, etc.), environmental parameters such as convection coefficients, base material chemistry and physical properties (86).

The sample geometry of the T-weld was first modeled in Pro-Engineer and exported as a stereo-lithography file or STL file for use in the VrWeld simulation software. An overview of the meshed part is shown in Figure 43a.

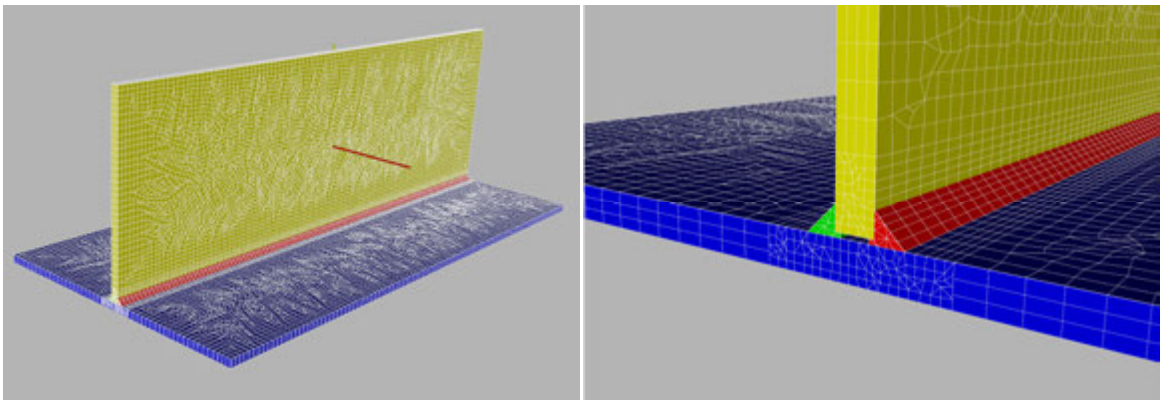

Figure 43 a) Finite element model of T-weld for welding simulation. b) Fine mesh in the HAZ.

The mesh is finer in the HAZ to account for the high temperature gradient and microstructural changes that occur, Figure 43b. The experimental welding parameters described in section 3.1 were used in the simulation. The tack welds were modeled by fixing the nodes in the locations shown in Figure 44.

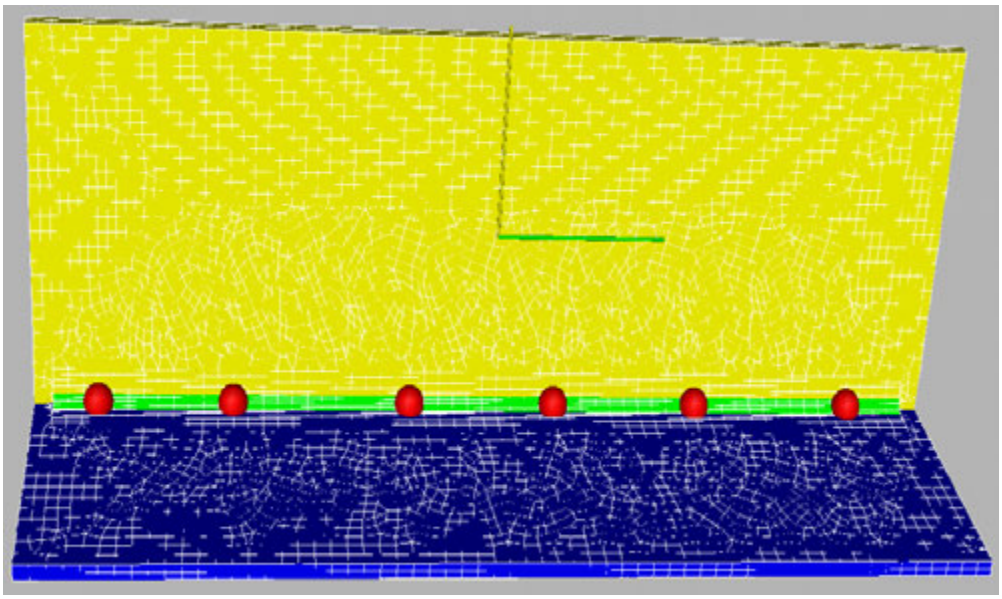

Figure 44) The red spheres mark the location of the tack welds in the simulation.

Displacement boundary conditions were prescribed to match the vise clamping condition. Since the sample was rotated to make the double fillet weld in residual stress validation and fatigue life work, two sets of clamps were modeled as shown in Figure 46. The clamps were modeled as ridged fixities and released at the prescribed time during the welding process. Since the welding process is not 100% efficient the heat input in the simulation was calibrated against experimental results to determine the proper efficiency level. To do this a macrograph of the weld is taken and the heat source shape in the simulation is matched to this shape by varying the efficiency level. An example of the image and matched simulation used in this dissertation is shown in Figure 46. Figure 46b shows the polished macroscopic cross-section while Figure 46a shows an example of a simulated heat source with proper fitting.

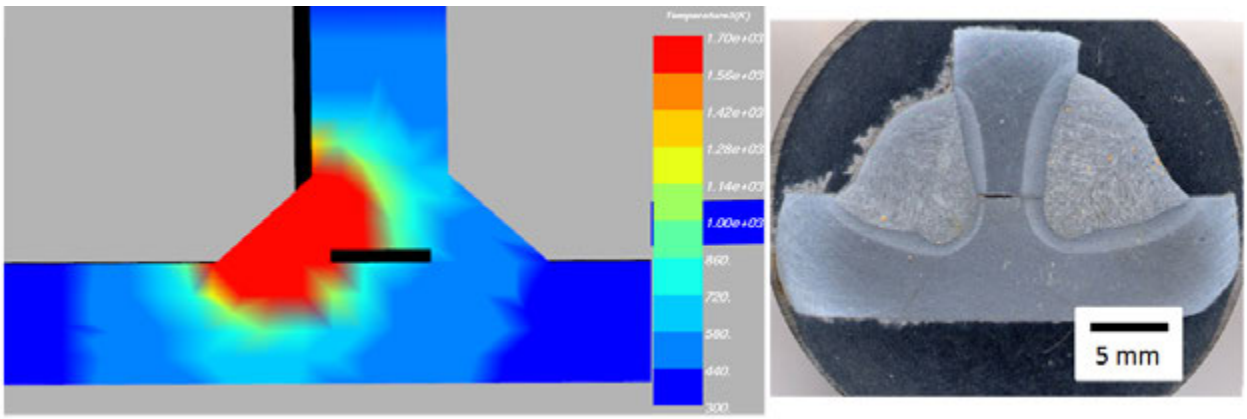

a) b)

Figure 45) a)Screenshots showing the heat source fitting for the welding simulation. b) weld micrograph used for the heat source fitting.

By adjusting the efficiency level, the value that best matched the actual profile was found to be ~80%.

The size parameters used in the double ellipsoid model discussed in Chapter 2 – Weld Modeling are:

$$a2 = 6\ mm,\ a1 = 12\ mm,\ b = 6\ mm,\ c = 12\ mm$$

Clamps were modeled in ProE and the VrWeld software then used the nodes that are adjacent to the clamp geometry as the clamp boundary conditions. Figure 46 shows the clamp geometry. The clamping is represented with two sets of clamps (STLfix1 for weld one and STLfix2 for weld 2). Two other sets of boundary conditions were used to constrain ridged body motion. The first (nf1) was used during the rotation of the sample between weld 1 and weld 2 and the second (nf2) was used after the weld 2 during the final cool down portion. The clamps are time dependent so STLfix2 is not applied during weld one and vice versa for weld two.

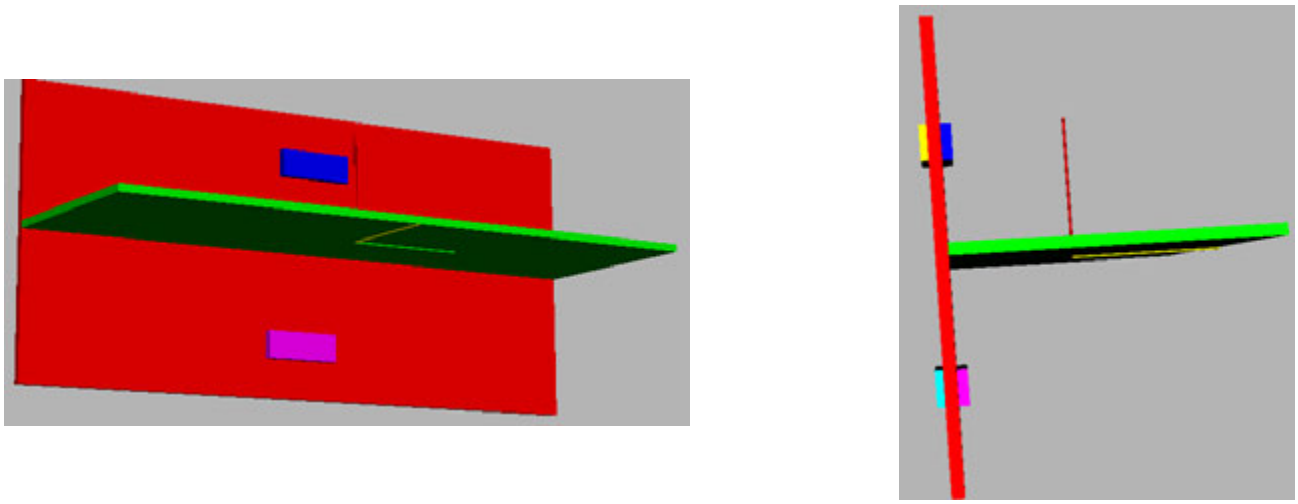

Figure 46) The clamping conditions are shown. The clamps were modeled to have the same dimensions as the vise holding the sample during welding.

The time for each of the welds was taken from the video recording of the process and representative times were used in the simulation. The times used for the simulation are as follows: STLfix1 was applied first during the first weld. The welding time for weld one is 70.254. Weld STLfix1 was released at 110 seconds and at that time nf1 was applied until 150.254 seconds when STLfix2 was applied. Weld two was then started at 160.254 seconds and was completed in at 230.254 seconds. STLfix2 was removed and nf2 was applied at 245 seconds. The simulation was run to 3600 seconds in order have the sample cool to room temperature.

5.3 Results

When analyzing the data it was found that the same trend in residual stress measurements hold for all three locations. To aid the reader only section 2 will be discussed. Only the measurements along line "a" are considered in this analysis. The initial residual stress state of the material from the manufacturing process biased the results in the other locations. Line "a" is in the heat affected zone so the residual stresses are assumed to be from the welding process alone.

Results from Sample 2 along weld line a

The residual stress measurements along line "a" for samples 23-2 and 24-2 and the computational simulation are shown in Figure 47 through Figure 48. Refer to Figure 42 for the location of the measurements. Point 1 refers to the point marked "150.8" and point 5 refers to the point marked "157.2." The other three points are the points between these two locations. The measurement data is shown for sample 2 along line "a" from Figure 42. The error bars for the stress in the x direction is +/- 25 MPa, +/- 34 MPa for the y direction and +/- 23 MPa for the z direction. This corresponds to 2 standard deviations of measurement error. The measurement

error was calculated my assessing the standard deviation of the d_0 reference sample mentioned in Section 5.2 Experimental Procedure.

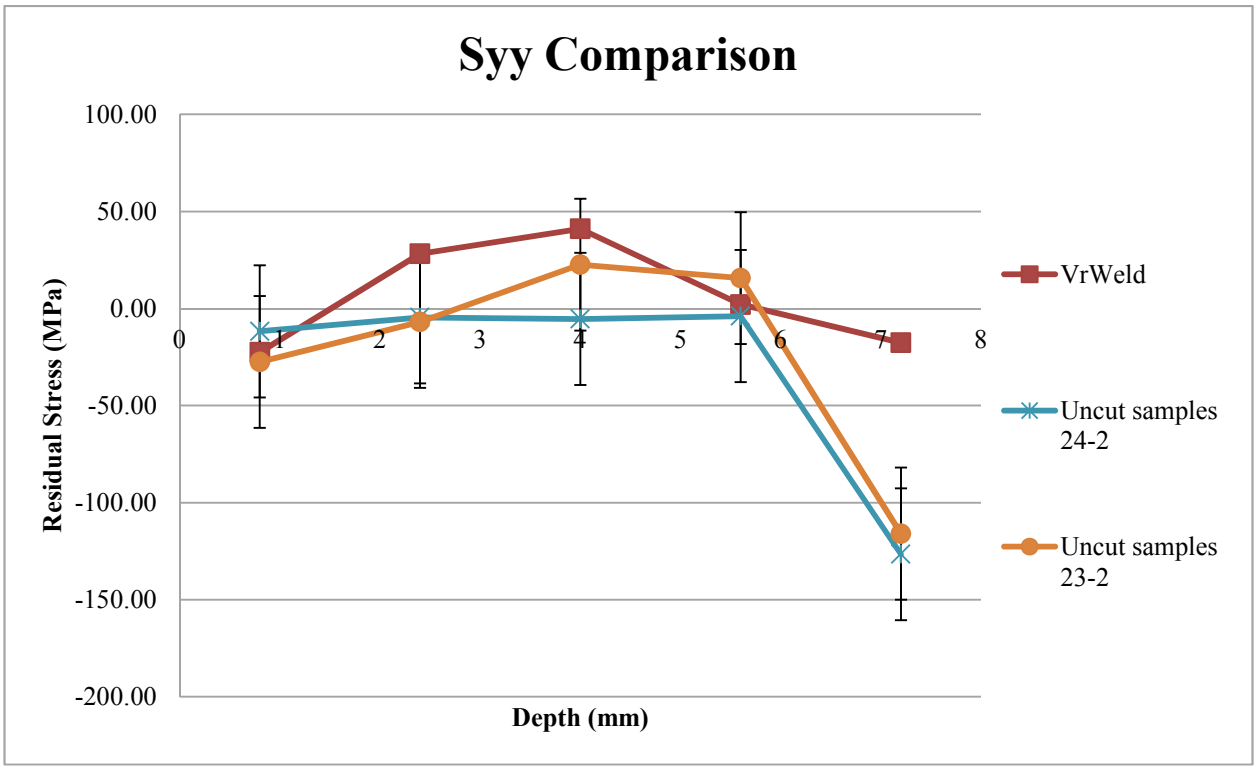

Figure 47) Comparison between the measured residual stresses and the predicted residual stress in the y direction.

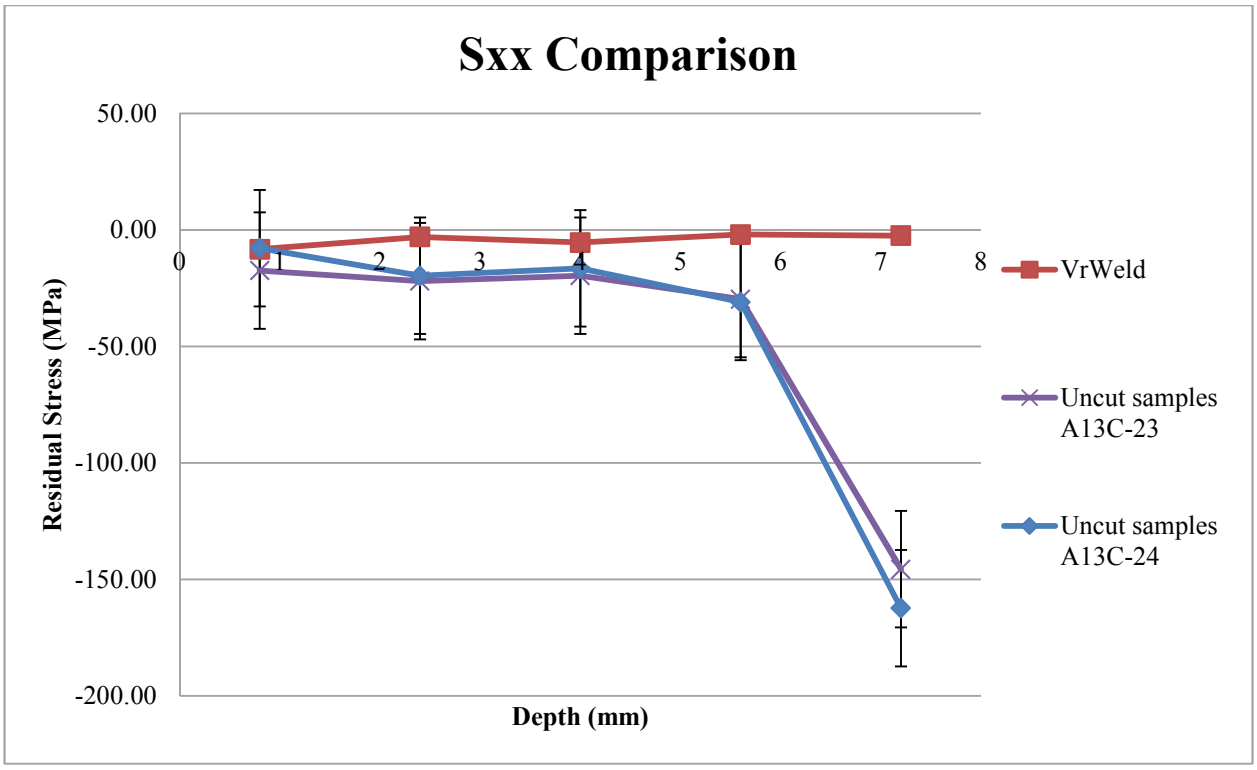

Figure 48) Comparison between the measured residual stresses and the predicted residual stress in the x direction

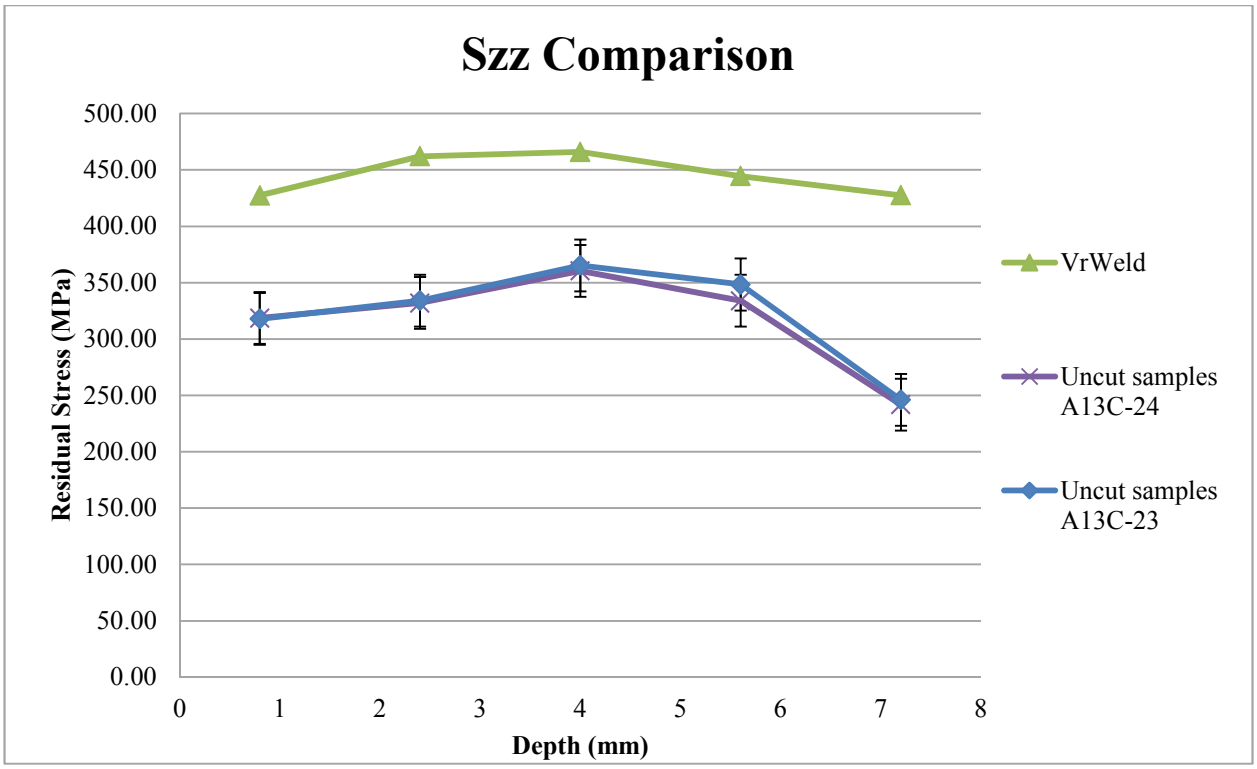

Figure 49) Comparison between the measured residual stresses and the predicted residual stress in the z direction.

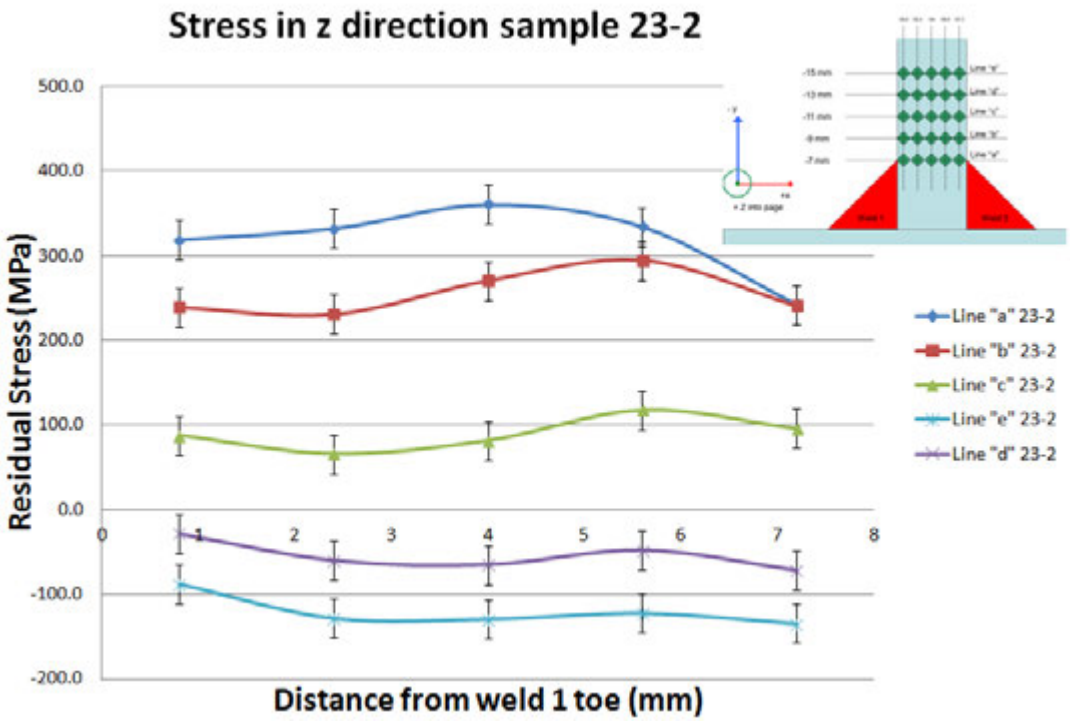

Figure 50) Graph showing the residual stress drop off in the z direction as function of the distance in the y direction from the weld toe.

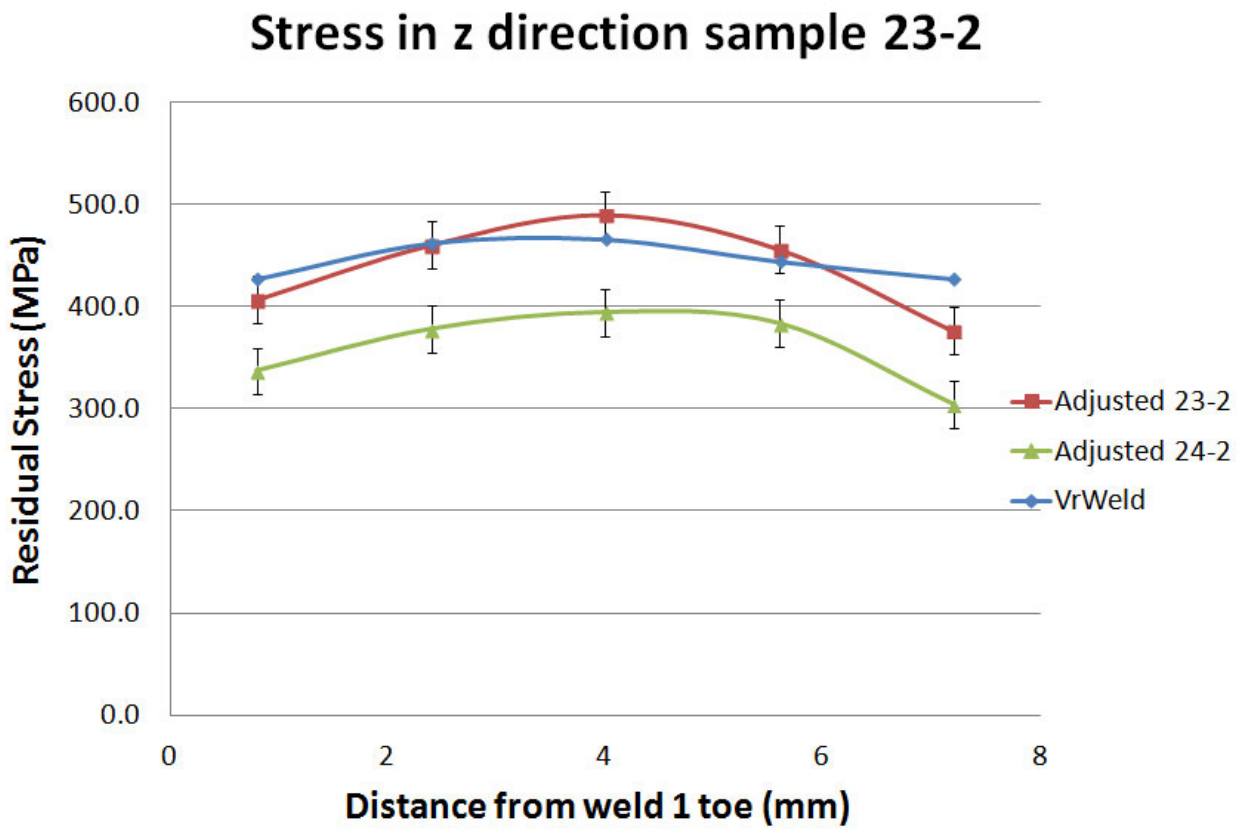

Figure 51) Graph showing the adjusted stress in the z direction compared to predicted residual stress.

5.4 Discussion

The residual stress patterns of the VrWeld simulation match the experimental results fairly well, showing the same general shape in the stress distribution. There are some anomalies in the values which require further discussion.

The first point of discussion is the deviation at point number 5 at 7.2 mm in depth. This point shows significantly lower stress than the simulation in all three directions. When measuring the residual stress the neutron beam is first aligned using the laser-scanning system and then fine adjustments were made by aligning the neutron beam using visual sighting equipment at the toe of weld 1, but it is not possible to align on the toe of weld 2. Unfortunately the weld size between

weld 1 and weld 2 were not the same. As seen in Figure 45b the weld size for weld 1 is slightly larger than weld 2 so when the neutron beam is scanned through the sample the beam is outside of the weld zone. Another point of difference is weld 2 has a smaller HAZ as shown in Figure 45b which would lead to less change in the residual stress from the welding.

The measured and simulated stresses in the y direction match very well at the first point, after which the simulation predicts slightly higher residual tensile stress then the measurements. Whatever the true reason for the observed deviation the values seen are still within a reasonable amount when considering the measured variation from sample to sample.

Unlike the x and y comparisons the stresses measured in the z direction are significantly lower than the predictions. The cause for this is due to the initial residual stress that was present in the material prior to welding. The residual stress measurements show that the stresses in the z direction are tensile along line “a” and “b” and then gradually get more compressive along line “c”, “d”, and “e” as shown in Figure 50. When the measured residual stress is offset by the initial residual stress that were measured along line “e” the residual stress prediction and measurements agree very well.

After accounting for the initial residual stress state in the material the residual stresses that were predicted and measured match very well. The critical location for fatigue analysis is the weld toe. In this case the predicted residual stresses falls in between the two measured samples.

5.5 Conclusion

This paper provided a validation of the residual stress predictions from simulation by comparing them to measurements conducted with neutron diffraction. From the study the following conclusions can be drawn:

1) Welding simulation can be used to predict the residual stresses with the accuracy needed in the critical locations for fatigue analysis.
2) There are part to part variations in residual stress that are inherent in the manufacturing process. These are likely due to the processes the parts were exposed to prior to the experiments. In order to use welding simulation to the fullest the initial state of the part needs to be know either through measurement or simulation.
3) It is critical to measure the input parameters when performing model validation rather than relying on the process set points.

The welding simulation showed that it has the accuracy to predict the residual stresses to be used in future durability assessments.

CHAPTER 6: REDISTRIBUTION OF STRESS DUE TO CYCLIC LOADING

The second question posed in this dissertation, "Does cyclic loading change the residual stress state…" is addressed in this chapter. Discussed below is an evaluation of a series of experiments where the residual stress as a function of cyclic loading was monitored using neutron diffraction.

6.1 Introduction

During durability testing it is a common practice to place strain gauges in the area of interest to measure the stains that occur during operation. If the strain gauges are placed near welds on a newly manufactured piece of equipment the gauge will "take a set", a term used to describe a shift in the strain. This shift is noticed to occur immediately upon testing. However, it has been noticed that if the piece of equipment to be tested is operated prior to placing the gauges the gauges do not take a set. In other words, there appears to be a change in the residual stress state that occurs immediately in newly welded parts due to initial operation. This phenomenon has been attributed to the relaxation of the residual stresses that arose during the manufacturing process. This relaxation is important when one realizes that most studies dealing with residual stress in fatigue assume that the level present initially continues throughout the service life of the part. If the stress level is changing significantly, the amount of change, and when it occurs, needs to be understood if one is to accurately assess the effect of residual stress on fatigue life.

The relaxation of residual stress in cyclically loaded structures has been studied (87) (88) (89) and there is a clear consensus that there can be significant stress relaxation in the first few cycles (89), (90), (91). Qian provides a summary of different relaxation models which shows that the numerical models for estimating the residual stress relaxation due to cyclic loading are dependent on the applied stress, number of cycles, material strength, initial residual stress state,

and amount of cold working (92). However, none of the reviewed models are able to account for the relaxation of the stresses in the first few cycles, information which is critical in this work.

To accurately predict the fatigue life of the structure the stabilized residual stress state needs to be known. This chapter will compare the measured residual stresses in the T-welded samples in the as-welded condition prior to cyclic loading and then at subsequent time intervals during cyclic loading. Any changes in residual stress will be determined and the effect these changes have on subsequent fatigue life predictions will be discussed.

6.2 Experimental procedure:

Experimental details on the preparation of the welded samples are given in Section 3.1 Sample Preparation. Included below are details specific to this experiment.

The large T-welded samples were sectioned into three samples using a band saw as denoted in Figure 52. Testing was conducted on 5 separate samples to ensure consistency and reproducibility; two samples from specimen 16 and three samples from specimen 21. The initial residual stresses at the weld toes in the as-welded samples were measured using neutron diffraction as discussed in Section 5.4. All measurements were done at the High Flux Isotope Reactor (HFIR) neutron diffraction facility at Oak Ridge National Laboratory. The samples were labeled with the sample number and the location within the sample as shown in Figure 52, with the numeral after the sample label denoting the particular weld toe. Thus, sample 16-1-2 would denote a sample taken from T-weld specimen number 16, sample 1 from the sample, measured from weld toe number 2. It should be remembered that for the T-welds two welds could be measured, one on either side of the T-weld.

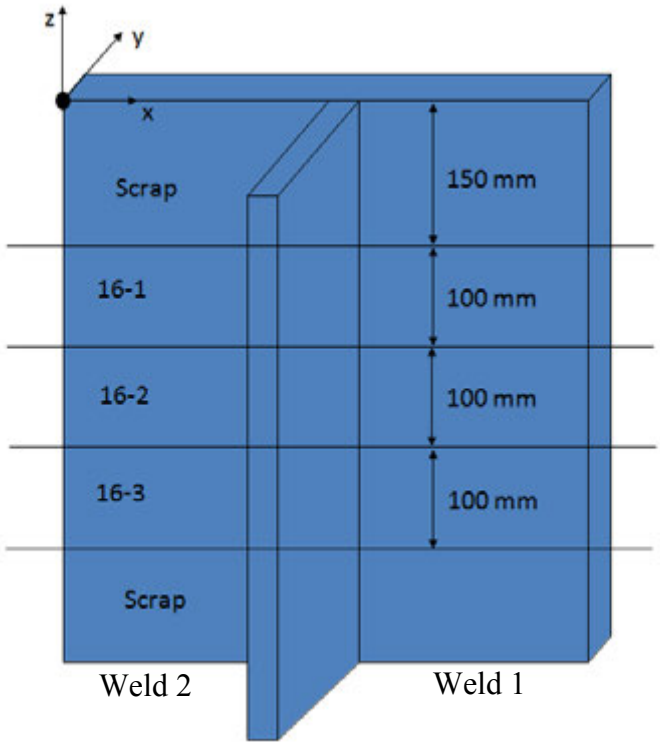

Figure 52) Overview of the large sample showing the numbering scheme**.**

The cyclic loading was done in a similar method as previously discussed in Section 3.2 Examination and Testing at High Temperature Materials Lab (HTML) within Oak Ridge National. The fatigue regime used cycled from tensile 2980 N to compressive 2980 N (i.e. -2980) for 100 cycles. The welded samples were returned to the High Flux Isotope Reactor to measure the residual stresses after cycling in the same location as the previous measurements. The neutron diffraction measuring technique was kept constant as explained in Section 5.2. The same sample fixturing was used for all the neutron measurements to ensure that the stresses were measured in the same location. This entire process was repeated after an additional 900 cycles at the HTML for a total of 1000 cycles. Common procedures and fixturing was used for the cycle testing, which ensured consistency from sample to sample and run to run.

The residual stress distribution through the thickness of the parts was measured. However, since fatigue generally initiates at the surface at a stress concentration point such as a weld, only the toe measurements are reported.

6.3 Results

While the stresses in all direction as noted in Figure 52 were measured, those in the Y direction are of most interest since these stresses are aligned with the crack direction and are those most responsible for causing fatigue damage. Therefore, only the stresses in the Y direction are discussed in this dissertation. The results obtained using neutron diffraction are summarized in Table 2, below and displayed graphically in Figure 53.

The measurements from weld toe 2, the samples labeled XX-X-2 in Figure 53, show an average reduction of residual stress of 54% with the high being a 70% reduction in 16-2-2 and a low of 41% in 16-1-2. All the measurements taken for weld toe 2 have the same trend.
The initial stress value for sample 22-1-1 was not as compressive as the other samples. This sample did not see a reduction in the residual stress after 100 cycles. The stress between 0 and 100 was constant when accounting for the accuracy of the measurement. Sample 16-2-1 showed a residual tensile stress of +39 MPa at 100 cycles. The residual stress changed to -24.4 MPa after 1000 cycles which is consistent with the other weld toe 1 samples. Table 2 provides all the measurement and this information is shown graphically in Figure 53. The error in the measurements was determined to be +/- 25 MPa; the method of determining this error is explained in chapter 5. In general the measured residual stress was found to be compressive in nature, with the value dropping significantly within the first 100 cycles.

The measurements from weld toe 1, the samples labeled XX-X-1 in Figure 53, show an average reduction of residual stress of 70% with the high being a 128% reduction in 16-2-1 to a

low of -18% in 21-1-1. All the samples show the same general trend with a few exceptions. For example, the initial stress value for sample 22-1-1 was not as compressive as the other samples; consequently this sample did not see much reduction in residual stress after 100 cycles. The stress between 0 and 100 cycles was essentially constant when accounting for the accuracy of the measurement. This can be compared to Sample 16-2-1, which showed a residual tensile stress of +39 MPa at 100 cycles. The residual stress changed to -24.4 MPa after 1000 cycles which is consistent with the other weld toe 1 samples

The measurements from weld toe 2, the samples labeled XX-X-2 in Figure 53, show an average reduction of residual stress of 54% with the high being a 70% reduction in 16-2-2 and a low of 41% in 16-1-2. This trend is consistent for all samples.

.

Table 2) Table of residual stress measurements as a function of number of cycles.

	Residual stress Measurements (MPa)									
	16-1		16-2		21-1		21-2		21-3	
	Weld Toe 1	Weld Toe 2	Weld Toe 1	Weld Toe 2	Weld Toe 1	Weld Toe 2	Weld Toe 1	Weld Toe 2	Weld Toe 1	Weld Toe 2
As cut	-146.4	-174.7	-138.4	-208.6	-43.5	-172.2	-141.1	-239.8	-126.8	-231.1
100 Cycles	-11.7	-103.7	39.2	-63.4	-51.4	-99.4	-56.0	-91.2	-18.7	-105.9
1000 Cycles	-8.4	-82.0	-24.4	-85.3	-37.0	-95.1	-30.7	-89.5	-17.2	-78.2

	Percent Reduction in residual stress from initial state (MPa)									
	16-1		16-2		21-1		21-2		21-3	
	Weld Toe 1	Weld Toe 2	Weld Toe 1	Weld Toe 2	Weld Toe 1	Weld Toe 2	Weld Toe 1	Weld Toe 2	Weld Toe 1	Weld Toe 2
100 Cycles	92%	41%	128%	70%	-18%	42%	60%	62%	85%	54%
1000 Cycles	94%	53%	82%	59%	15%	45%	78%	63%	86%	66%

	Percent Reduction in residual stress from 100 to 1000 cycles state (MPa)									
	16-1		16-2		21-1		21-2		21-3	
	Weld Toe 1	Weld Toe 2	Weld Toe 1	Weld Toe 2	Weld Toe 1	Weld Toe 2	Weld Toe 1	Weld Toe 2	Weld Toe 1	Weld Toe 2
1000 Cycles	28%	21%	162%	-34%	28%	4%	45%	2%	8%	26%

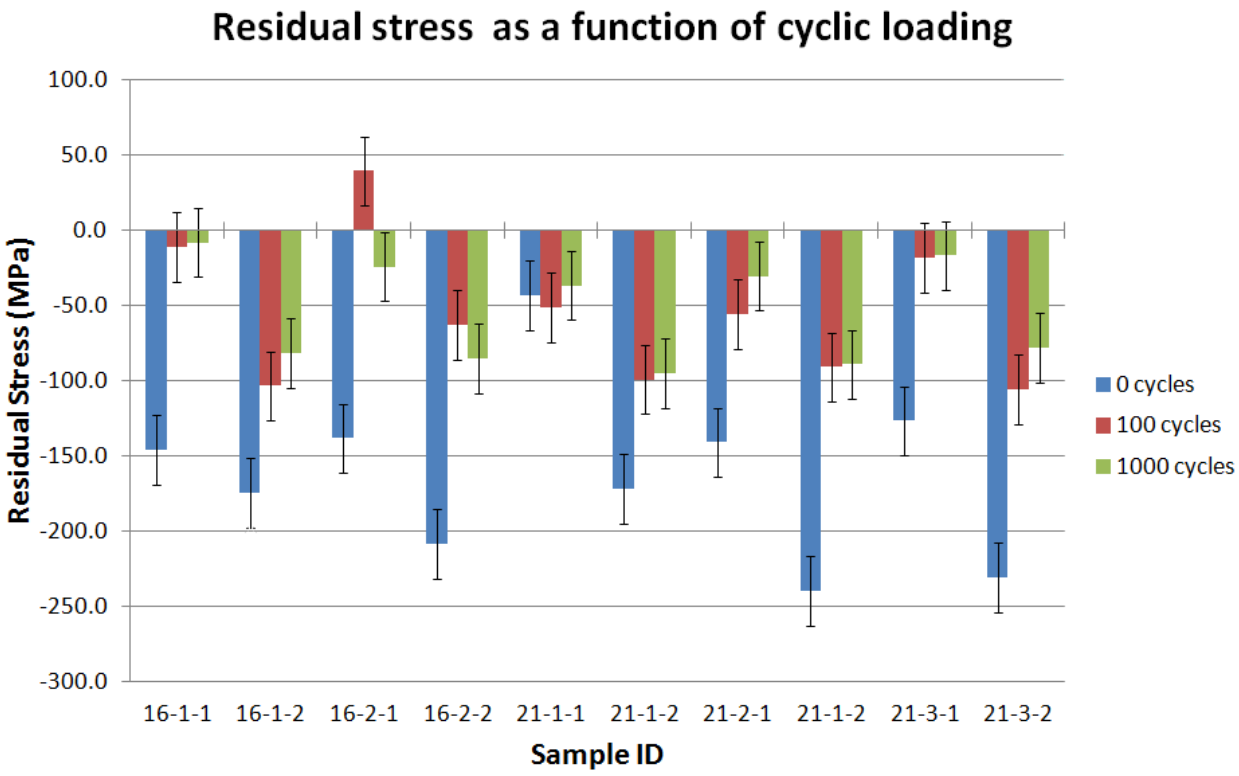

Figure 53) Graph showing the residual stress at the weld toe as a function of the number of cycles.

There are a number of clear differences in the state of residual stresses in weld toe 1 vs 2. For example, the initial magnitude in the residual stresses in weld toe 2 in general is larger than weld toe 1. However, the reduction in residual stress in weld toe 1 is much greater than weld toe 2. Careful consideration of the location of the neutron measurements from Chapter 5 offers one reason for the variations seen. It seems likely now that the neutron measurements at weld toe 2 were actually taken approximately 2 mm from the weld toe. Figure 54 shows that macrograph of the cross section of the welded joint. When considering that the neutron measurements were aligned on weld 1 and the traverse was taken in the x direction to weld 2 (as indicated by the

black arrow), the measurements in weld 2 would appear to have been made above weld 2. Thus, while the measurements taken on weld toe 1 were at the weld toe a straight line scan would miss weld toe 2 by a small but substantial amount. This would be consistent with the measurements taken in Chapter 5.

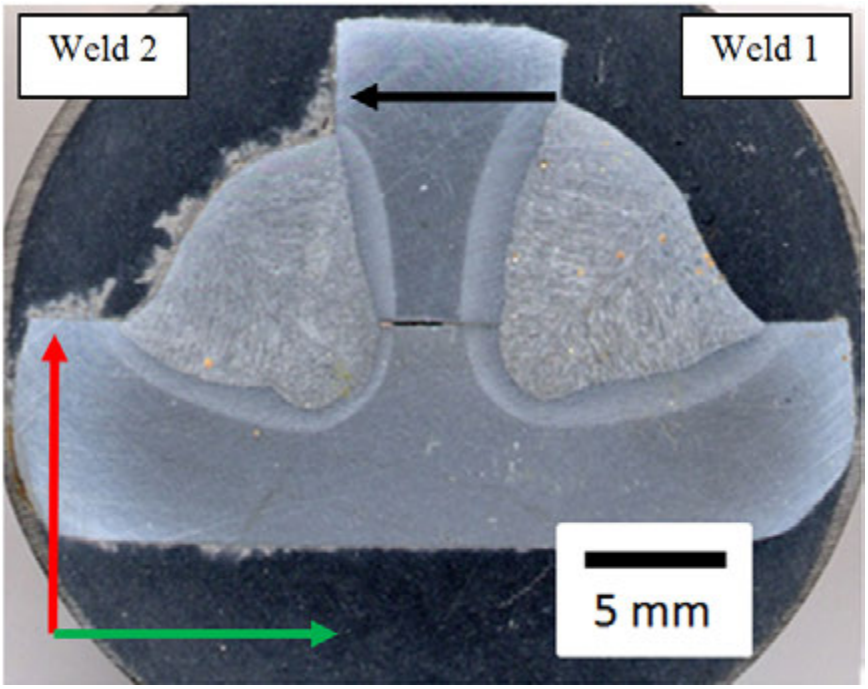

Figure 54) Macrograph of the cross section of the weld.

6.4 Discussion

The results clearly show that residual stresses change due to the cyclic application of a load. This is in agreement with the relaxation of residual stresses shown in other studies and most recently presented by Qian in (92). Qian's model shows a dependence of the amount of residual stress relaxation on the applied stress, the yield stress of the materials, the number of cycles experienced, and material fitting parameters fit from experimental data. In his work he suggested that residual stress relaxation shows the same behavior as dislocation creep and a

model was proposed that showed good correlation. Qian applied stresses that ranged from 25% to 120% of the yield strength with an R ratio of 0.1. He observed little stress relaxation below the yield stress while significant relaxation occurred when the stresses were above the yield stress.

While the applied stress used in this experiment was lower than the yield stress, keep in mind this does not take into account the effect stress concentration has on increasing the local stress. If one takes into account weld geometry, the stress at the weld toe in the samples in this experiment were significantly above the yield stress due to the much higher Kt. Thus, the stress relaxation observed is in accordance with previous studies and the model proposed by Qian.

The fact that weld geometry induces a significant stress concentration could be the underlying cause producing localized plasticity at the weld toe in these samples. The stress concentration created by the local geometry and thickness change in the T-weld at the weld toe produces a non-uniform stress distribution through the thickness of the vertical plate. Figure 55 shows the stress distribution under an applied bending force through the thickness of a double fillet weld (48).

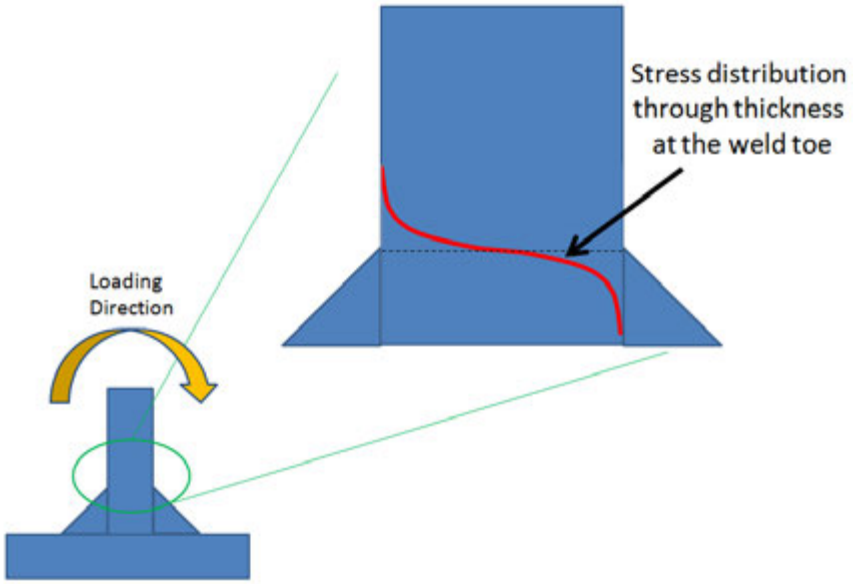

Figure 55) Diagram showing the stress distribution through the thickness when bending is applied to the sample.

The high stresses and resultant plasticity could reduce the initial residual stress in several ways. The first hypothesis is that the high stress concentration causes a portion of the material at the weld toe to locally yield and plastically deform, as shown in Figure 56a, much the same way plastic deformation occurs ahead of a crack tip (93). In this simple model, only the portions of the material where the stresses exceed the yield strength plastically deform. When the load is released the plastic deformation zone has expanded while the elastically deformed material around this zone returns to the original volume. The resultant volume mismatch then drives the establishment of a new set of residual stresses, which are different than the initial residual stress state. This mechanism is shown in Figure 56b. Note that on the opposite side of the T-weld sample the situation is reversed. For this scenario the weld toe region is put under compression. In this case the process reverses and the strain induced is a negative strain rather than a positive strain, the opposite effect would occur and the residual stresses would be in tension.

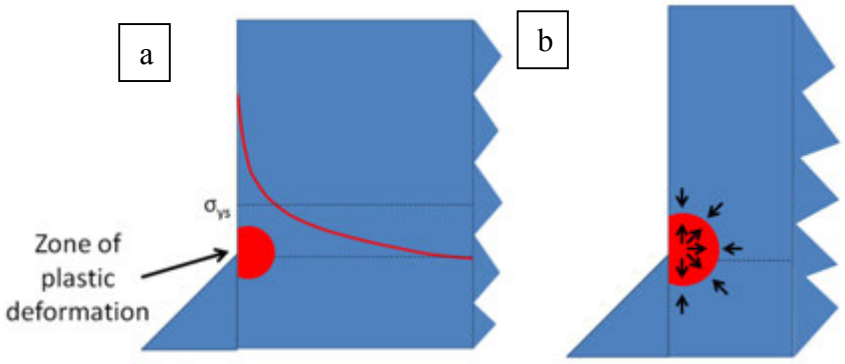

Figure 56) Pictorial of the mechanism for the changes in residual stress at the weld toe.

Using a simple uniaxial model to calculate the amount of plastic strain induced at the weld toe shows that the residual stresses are much more compressive than the initial conditions.

A second way of thinking of the stress relaxation would be to look at the strain/strain response at the weld toe. If the relaxation of the residual stress comes from localized plasticity then the residual stress state can be modeled using the cyclic stress strain response. A visual representation of this situation is shown in Figure 57, where the values were calculated by using the cyclic stress strain response shown in Section 2.3.4 Elasto-plastic stress strain response. Figure 57 shows two scenarios. The first scenario is where the material is starting at Point "A", where the sample is under a residual compressive stress and is loaded in tension, followed by completely reversed compression, after which the external load goes to 0. The end result of this scenario is a slightly tensile residual stress. The second scenario also starts at point A under compressive stress but goes into compression first followed by a tensile load, and finally the load is released and goes to 0. In this case the resultant residual stress is highly compressive.

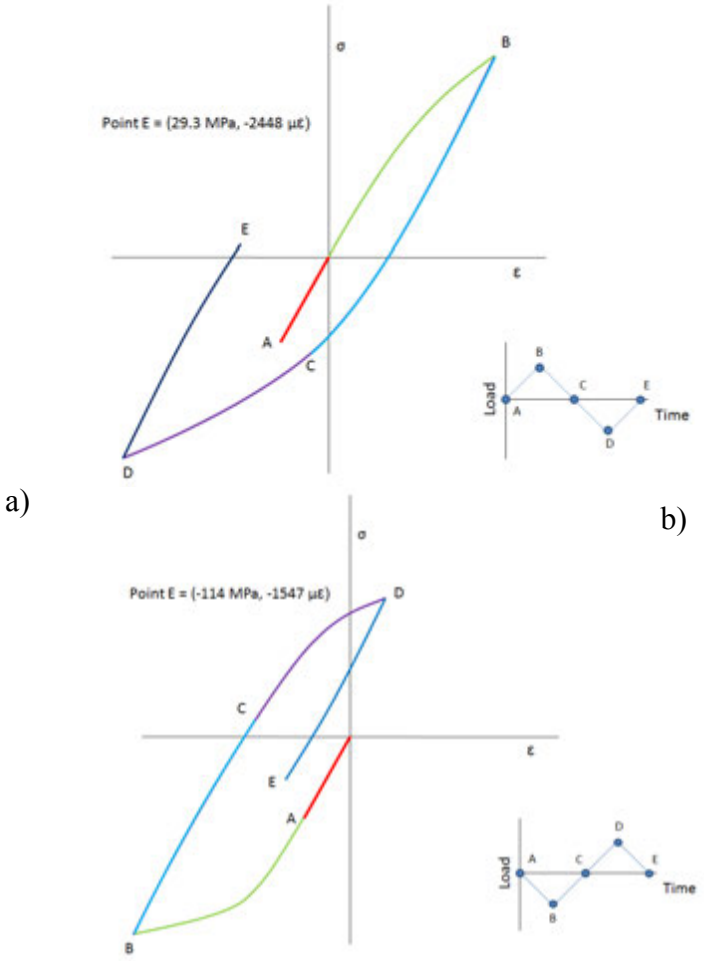

Figure 57) Sketch of the stress strain curve during loading for two scenarios. Scenario A (graph a) shows the stress strain path when the sample is loaded in tension first followed by compression. Scenario B (graph b) shows the stress strain path when the sample is loaded in compression first.

Even though both of these explanations are plausible for changing the residual stress state, unfortunately neither matches the experimental results. It is clear from the residual stress measurements that the stresses are significantly relaxed and did not conform to the residual stress state predicted by modeling the plasticity directly. This shows that a simple unidirectional

plasticity model does not account for the residual stress relaxation. A more comprehensive three-dimensional stress model that accounts for yield criteria and plasticity induced in the base material is needed to fully understand of the effectiveness of this model. Such an analysis is beyond the scope of this dissertation work.

Once the initial relaxation occurs within the first few cycles the measured residual stress does not change significantly, the small change that does occur from cycle 100 to cycle 1000 being within the measurement error and not statistically significant. It is interesting to note the difference between stress reductions for the two weld toes. As stated in section 6.3 the measurements taken on weld toe 2 were most likely measured adjacent to the toe of the weld. The distribution of expected stresses adjacent to a weld toe is shown in Figure 58. Since the weld toe 2 stresses are not lower (i.e. they are not at the location of high stress concentration), less stress relaxation is expected. This would hold consistent with the hypothesis that the amount of plastic deformation drives the stress relaxation. In a lower stress region, with no stress concentration, little or no plasticity is expected.

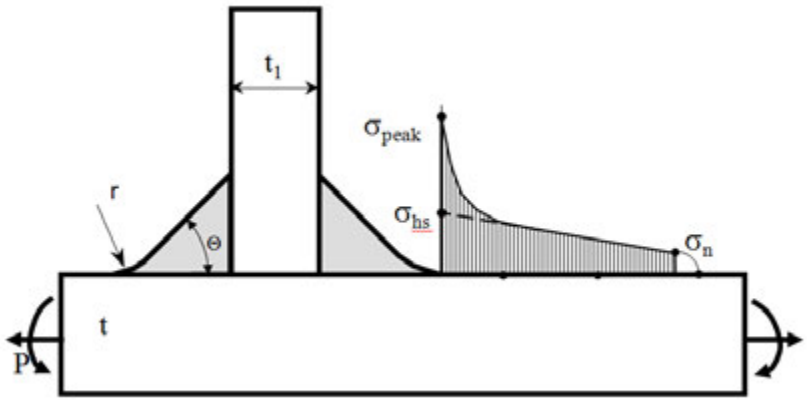

Figure 58) Stress distribution ahead of the weld toe showing the drastic change in stress near the weld.

If the hypothesis that the rapid initial change in residual stresses is driven by local plastic deformation due to stress concentration is true, it would seem that both the initial residual stress state and the applied stress interact to produce stress relaxation. Since the loading applied in this experiment is constant amplitude, where the peak stress is consistent, the relaxation of the stresses would occur at the first loading cycle. The damage that occurs on the first cycle due to this high stress is small when considered over the lifetime of the part, so the difference in damage if one excludes the residual stresses from the initial state is negligible. For the purposes of this dissertation, where constant amplitude testing is used, the stabilized stress state should give a more accurate evaluation of the effect of residual stress than the initial manufactured residual stress. A comparison of the use of the initial and relaxed residual stress states for fatigue life predictions will be conducted in Chapter 7.

6.5 Conclusion

The residual stresses measured in as-fabricated parts may be a poor indication of the actual stress state the part sees during its use life. Experiments show that the initial stresses redistribute themselves very quickly as the structure is cycled, mostly likely within the first few cycles, resulting in a residual stress state that can be considerably different from what was initially measure. A basic model of how the residual stresses change has been presented, but it does not effectively account for the residual stresses. The physical principles of the model account for the plasticity around the weld toe, but additional variables are needed to accurately model the residual stress redistribution. The experimental work shows the redistributed residual stresses stabilize around a fairly constant value. The results of these experiments show that the stabilized residual stress is a much more accurate description of the residual stress state in a part and should be used in fatigue life calculations.

CHAPTER 7: STOCHASTIC LIFE PREDICTION OF WELDED STRUCTURES

The third and final question this dissertation seeks to answer is: Can the distribution of fatigue life be predicted by accounting for the variability of the input parameters such as residual stress, material strength, local weld toe geometry, and material properties? In this chapter a methodology to predict the variation in fatigue life by incorporating the statistical distribution of these input parameters is discussed. A validation of the technique to predict life variation will be presented by comparing the fatigue life distribution of experimentally tested samples to the predicted fatigue life distribution, obtained by a consideration of the data obtained throughout the initial chapters of this dissertation.

7.1 Introduction

The fatigue life of a component or structure is dependent on three major design aspects; the component geometry, the material's mechanical properties, and the stresses placed on the component. The latter includes both service loading of the structure and any residual stresses present. Additionally, all of these design aspects have variability associated with either their measurement or application as an added complication, and this variability has a direct impact on the fatigue life of the structure. This concept is shown schematically in Figure 59.

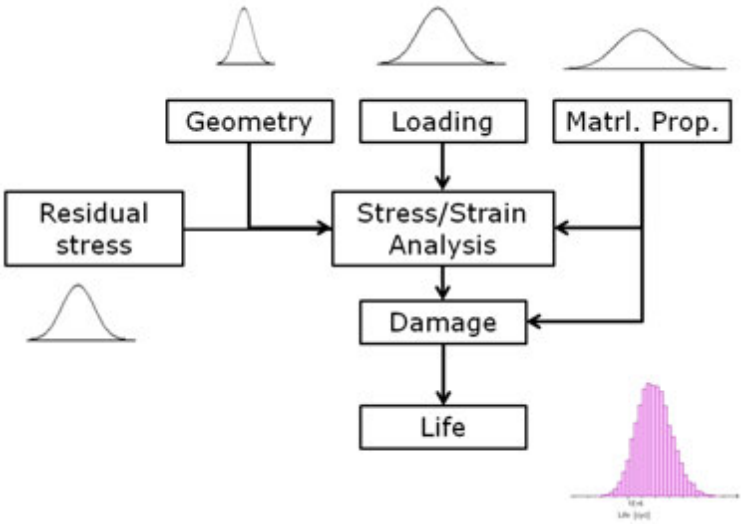

Figure 59) Schematic of the fatigue life prediction process. Each variable used in the life prediction is treated as a distribution.

Welded structures are notorious for having variability in fatigue life due to the large amount of uncertainty associated with the input parameters, as discussed in Section 2 Background. Capturing this variability in a quantitative manner is of prime interest if computational methods for predicting life are to be useful. This chapter will suggest and demonstrate a process for capturing the variability of the input parameters and determining their statistical characteristics. The resultant data will then be used in fatigue life calculations to predict durability and the results will be compared to actual experimental test data.

The notch strain life approach, described in detail in Section 2.3.2, will be used for fatigue life prediction in this analysis. As shown in Figure 59, the distribution of four input parameters is needed to predict the fatigue life, namely sample loading, geometry, material properties, and residual stress distribution. In this study, the distribution of the loading is held constant for each of the three load levels used and the coarse mesh FEA method proposed by Goyal is used to calculate the stress from the loading (94). Sample geometry in the case of a

welded joint is defined in this study by the weld toe angle and radius. The distribution of the weld toe radius and angle are used to calculate the distribution of the stress concentration factor, which is directly related to the geometry. The third and fourth input variables, the distribution in the material properties and residual stress distribution, were determined experimentally using strain life fatigue testing and neutron diffraction experiments, respectively.

Many of the above parameters have already been discussed in detail in earlier chapters, so in the next section only a brief summary will be provided. A methodology for determining material property distribution, which has yet to be discussed, will be presented in some detail.

7.2 Experimental procedure

Calculation of stress from loading

The FEA analysis of the T-welded sample was used to determine the hot spot stress for the loading conditions. This was done by using the method described in Section 3.2 Structural Modeling. The stress distribution starting at one weld toe directly across to the other weld toe was extracted from the FEA model. Since the FEA model used a linear elastic material model, the stresses could be scaled based on the input load without having to run multiple models. The hot spot stress is extracted from the FEA model using the details provided by Goyal et al. (94) Goyal shows the stress distribution from 25% to 75% of the thickness is found to be independent of the weld stress concentration factor. The hot spot stress is then calculated by extrapolating the linear distribution of the mid thickness stress to the surface.

Weld Geometry Measurement and Kt distribution

The weld geometry, specifically the radius and angle of the weld toe, was measured using the procedure described in Section 3.2 Geometry Measurements. The weld geometry was

measured on 14 samples approximately every 5 mm along the weld line. The number of points measured along each of the weld lines ranged from 10 to 19 points. Points that showed abnormalities due to the making of the replica were excluded from the data. A total of 220 locations on the welds were considered in the analysis. The results were compiled and the statistical distribution of the weld geometry was determined using a software package called *Weibull+*.

The weld stress concentration factor (Kt) is defined as a function of the weld toe radius and angle. Using the equations for bending of a T-weld discussed in Section 2.3.3 Calculation of Peak Stress and the measured distribution of weld toe radii and angles a Monte Carlo simulation was performed to determine the distribution of Kt. The Monte Carlo simulation considered the distribution of the measured weld toe and radius geometries and calculates the Kt. The simulation was run 1000 times and the results were recorded. The simulation treated the weld toe and radius as independent distributions with no dependencies on each other. *Weibull+* software was used to determine the weld Kt distribution from the Monte Carlo simulation results.

Material Property Distribution

Strain life fatigue tests were carried out using ASTM specification E606. In the strain life fatigue tests, the stress-strain hysteresis loops were obtained through fully reversed strain controlled cyclic loading, using the samples and equipment described in Section 3. To best determine the strain life curve 18 samples (or tests) were run at different strains. The ASTM A572 grade 50 steel used in this dissertation showed cyclic softening during the strain life testing so the half-life hysteresis loop was used in the material property fitting. The data from each sample that was run at a particular strain was then fit to the respective portions of the Manson-

Coffin relationship found in Equation 12. The manner by which this was done is discussed below.

The two parts of the Manson-Coffin equation are fit independently; the plastic portion the curve, $\varepsilon_f^{'} \left(2N_f\right)^c$, to the plastic strain amplitude verses number of reversals, and the elastic portion of the curve, $\frac{\sigma_f^{'}}{E}\left(2N_f\right)^b$, to the elastic strain amplitude verses number of reversals. The values for the fatigue strength exponent (b) and the fatigue strength coefficient ($\sigma_f^{'}$) are determined from the elastic portion of the curve while the fatigue ductility exponent (*c*) and the fatigue ductility coefficient ($\varepsilon_f^{'}$) are determined from the plastic portion. The description of the method for curve fitting to calculate the strain life fatigue parameters is outlined in ASTM E739-10. In brief, the total strain amplitude for each of the individual samples at a particular strain is broken down into the elastic and plastic portions of the strain. The elastic portion is given by:

$$\frac{\Delta\varepsilon_e}{2} = \frac{\sigma_a}{E} \qquad \text{Equation 38}$$

where $\Delta\varepsilon_e$is the elastic strain amplitude, σ_a is the stress calculated from the strain-life sample, and E is the elastic modulus. The plastic portion is calculated using the following equation.

$$\frac{\Delta\varepsilon_p}{2} = \frac{\Delta\varepsilon_t}{2} - \frac{\Delta\varepsilon_e}{2} \qquad \text{Equation 39}$$

where $\frac{\Delta\varepsilon_t}{2}$, the total is strain amplitude and $\frac{\Delta\varepsilon_p}{2}$ is the plastic strain amplitude.

The plastic strain amplitude is plotted against the number of cycles on a log-log scale and a best-fit line using a least square regression is drawn. On this plot, $\varepsilon_f^{'}$ is the intercept at the y axis and c is the slope of the curve. The form of the equation is shown in Equation 40 (95).

$$\frac{\Delta\varepsilon_e}{2} = \varepsilon_f^{'}\left(2N_f\right)^c \qquad \text{Equation 40}$$

The elastic portion of the curve is fit in the same manner as the plastic portion, with in this case the y-intercept being $\frac{\sigma_f^{'}}{E}$ and the slope is the exponent b.

$$\frac{\Delta\varepsilon_e}{2} = \frac{\sigma_f^{'}}{E}\left(2N_f\right)^b \qquad \text{Equation 41}$$

Figure 60 provides a sketch of the two curves that are fit to determine the strain life fatigue parameters.

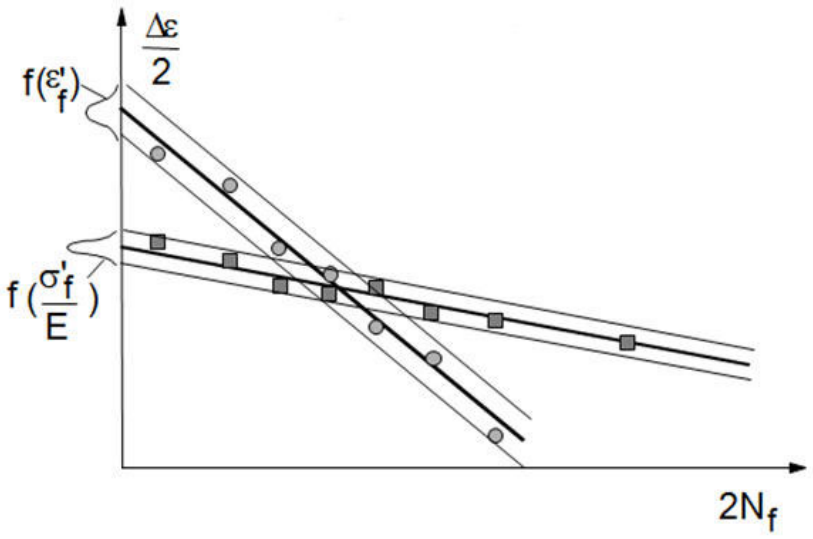

Figure 60) Representative graph showing the breakdown of the elastic and plastic portions of the Manson Coffin strain life curve.

The material property fitting and statistical characterization was done with a separate program called *FALIN*. *FALIN* uses the standard fitting procedure for strain life fatigue data outlined in ASTM E606. The program also provides a distribution of the material properties by accounting for variability in the test data. The procedure accounts for the difference in the predicted life from the best-fit parameters and the test data to determine the distribution of the fatigue strength coefficient ($\sigma_f^{'}$) and fatigue ductility coefficient ($\varepsilon_f^{'}$). The distributions for the fatigue strength coefficient ($\sigma_f^{'}$) and fatigue ductility coefficient ($\varepsilon_f^{'}$) were log normal, which is typical.

Unfortunately, the ASTM A572 grade 50 steel tested to determine the strain life was not from the same heat of material as was used for the T-weld samples. Due to test limitations the minimum thickness of samples that can be run is 12 mm, while the thickness of the T-weld sample material was only 8 mm. An attempt was made to run 8 mm samples; however, it was

unsuccessful due to unexpected fatigue initiation in the grip section of the samples. In an attempt to account for the strength difference between the material used to gather the strain life parameters and the T-welded samples, the strain life fatigue material properties were scaled using the Seeger equation to account for the difference in hardness between the test data and the t-welded samples (57).

Residual stress distribution

The statistical distribution of the residual stress was taken from the near surface neutron measurements presented in Chapter 6. *Statistica*, a statistical analysis software package, was used to determine the statistical distribution for the sample at 0 cycles and after 100 cycles. The distributions of the residual stresses for each of these conditions were then used in *FALIN* to predict the expected fatigue life distribution.

Fatigue life predictions:

Each of the distributions for the four input variables was used in a Monte Carlo simulation to predict the fatigue life distribution. A schematic outline of the process used is provided in Figure 61 where the life prediction is repeated "N" number of times. Fatigue life predictions were made using the *FALIN* software package. The fatigue life predictions combine the stress concentration Kt, the hotspot stress, tabulated material properties, and the measured (or predicted) residual stress to predict the fatigue life. The strain life fatigue properties along with the distributions of Kt, σ_f' , ε_f' , *K'*, and *n'*, are input into the software. The hotspot stress was used in the analysis since the stress concentration is an independent variable and needs to be used

to calculate the peak stress. From the hotspot stress and the stress concentration, the Neuber rule was used to calculate the peak stress.

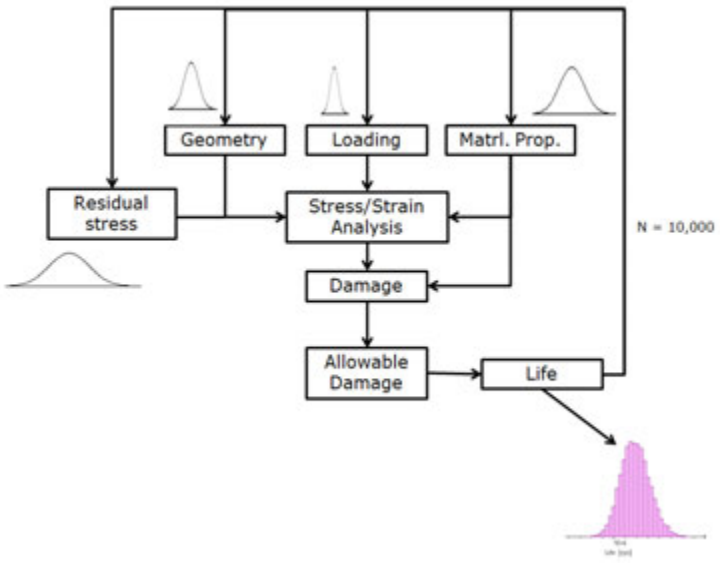

Figure 61) Process flow of how the predicted life distribution was done using the Monte Carlo simulation.

With the distributions of Kt obtained from measurements of the weld toe radius and angle and the $\sigma_f^{'}$, $\varepsilon_f^{'}$, K', and n' obtained from the fitting of the strain life material properties, a Monte Carlo simulation to predict the fatigue life was run with 10,000 iterations. The results of the Monte Carlo were then used to predict the distribution of life and compared it to the experimentally determined fatigue life distribution.

7.3 Results

Weld Geometry and Bending Stress Concentration:

The measurements of the weld toe angle and radius measurements are shown in Figure 62. The figure shows that there is little to no correlation between the weld toe angle and the

radius. This large spread is one of the reasons fatigue life prediction can be so difficult.

Analysis of this data using *Weibull+* produces the probability distributions shown in Figure 63.

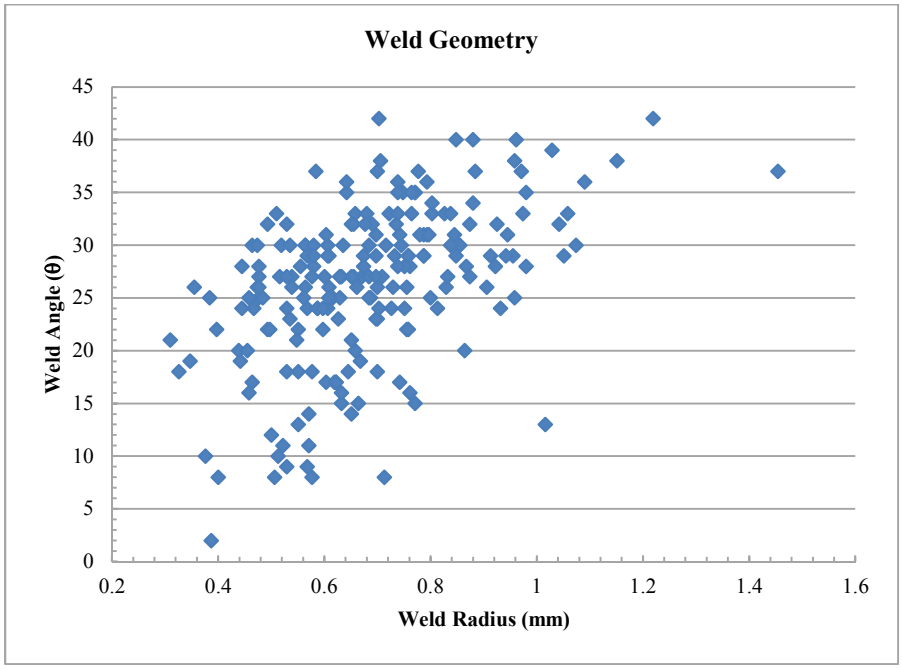

Figure 62) Scatter plot of the weld toe angle verse the weld toe radius.

Figure 63A shows the probability density function (PDF) plot of the weld toe angle while Figure 63b shows the PDF of the weld toe radius.

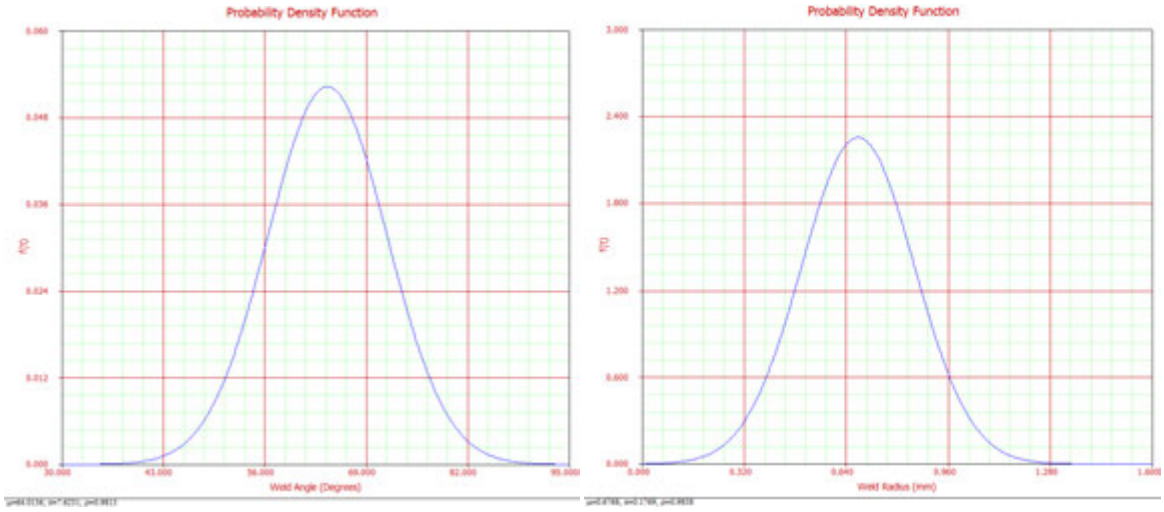

Figure 63) a)PDF plot of weld angle. b) PDF plot of the weld radius distribution

The weld toe angle and radius data of Figure 63 is best fit by a normal distribution. The mean and standard deviation for the radius and angle as determined from these distributions are given in Table 3. The distribution of Kt was determined by sampling the weld toe angle and radius distribution independently with Monte Carlo simulation techniques. Equation 5, which is restated below, was used in the Monte Carlo simulation to calculate bending Kt and determine the stress concentration distribution.

$$K_{t,hs}^{b} = \left\{1+\frac{1+\exp\left(-0.9\theta\sqrt{\frac{W}{2h_p}}\right)}{1-\exp\left(-0.45\pi\sqrt{\frac{W}{2h_p}}\right)}\times\sqrt{\tanh\left(\frac{2t}{t_p+2h_p}+\frac{2r}{t_p}\right)}\times\tanh\left[\frac{\left(\frac{2h}{t_p}\right)^{0.25}}{1.\frac{r}{t_p}}\right]\times\left[\frac{0.13+0.65\left(1.\frac{r}{t_p}\right)^{4}}{\frac{r}{t_p}^{\frac{1}{3}}}\right]\right\}\times\left\{1+0.64\frac{\left(\frac{2c}{t_p}\right)^{2}}{\frac{2h}{t_p}}-0.12\frac{\left(\frac{2c}{t_p}\right)^{4}}{\left(\frac{2h}{t_p}\right)^{2}}\right\}$$

Equation 5

Table 3) Table of the descriptive statistics of the weld toe radius and angle

	Distribution Type	**Mean**	**Standard Dev.**
Weld Angle	Normal	64.01°	7.6231°
Weld Radius	Normal	0.6768 mm	0.1769 mm

Stress concentration distribution:

Figure 64 shows the probability plot from the Monte Carlo simulation of Kt using the measured weld toe radius and weld toe angle distributions. The measured data is shown as circles while the solid line is the line of best fit using a log normal distribution. Log normal distributions typical fit functions that have an absolute minimum such as with Kt. The values at the extreme edges, below 1% and above 99%, show slight deviations from this distribution. The descriptive statistics of the Kt distribution are shown in Table 4.

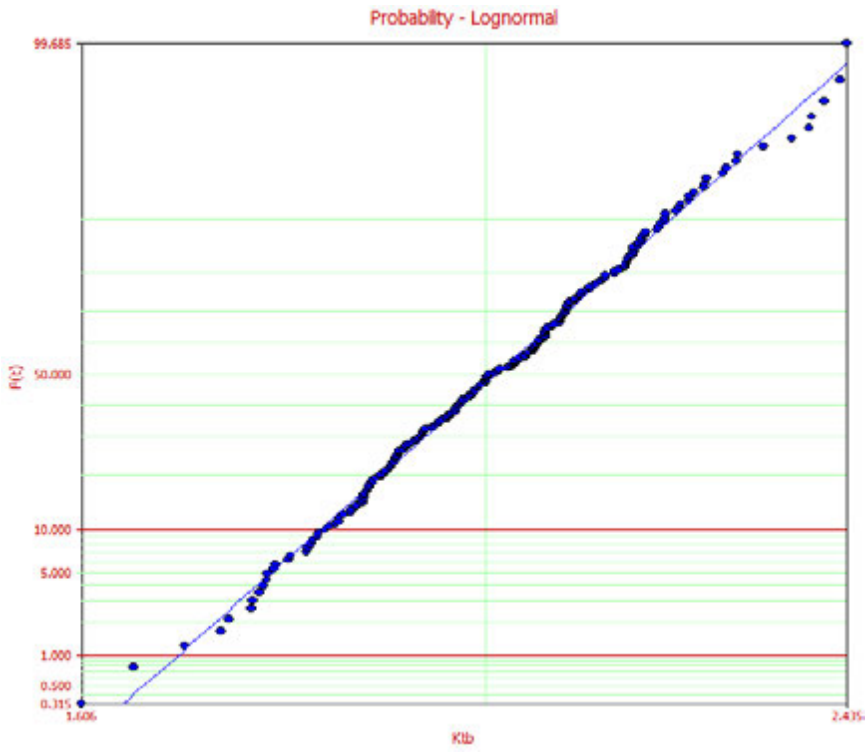

Figure 64) Probability plot of the Monte Carlo Simulation of the Kt.

Table 4) Descriptive statistics for the Kt distribution.

	Distribution type	Mean	Standard Dev.
Kt bending	Log-normal	2.0176	0.0743

One hypothesis put forward in this investigation is that the stress concentration Kt is not solely dependent upon geometry but is also dependent on the length of the high stress region referred to as the hot spot. Per the sampling procedure laid out in this dissertation, weld geometry measurements were taken every 5 mm. Since the hot spot length is greater than the sampling size of 5 mm, it is believed that using the full distribution of Kt directly would lead to under predicted lives since the probability of having a high Kt would increase with the length of the hot spot stress. (More detailed analysis is presented in section 7. 4 Discussion.)

To investigate this effect, the Kt distribution was sampled multiple times using a Monte Carlo simulation. The number of iterations used in the Monte Carlo simulation correlates to the hot spot length. For example, if the length of the hot spot is 50 mm, then the likelihood of having a high Kt value along the weld toe increases. The white region arrowed in Figure 65 shows the length of the hot spot stress. For a hot spot stress of 50 mm, 10 iterations of the Monte Carlo simulation would be used to simulate the Kt distribution along the hot spot length. The maximum value within the 10-iteration output from the Monte Carlo simulation was taken as the maximum Kt expected for the length of the 50 mm hot spot. The Monte Carlo simulation was repeated 200 times to ensure enough samples for a good statistical fit, and the maximum value of Kt found from these 200 simulations was used to fit the distribution.

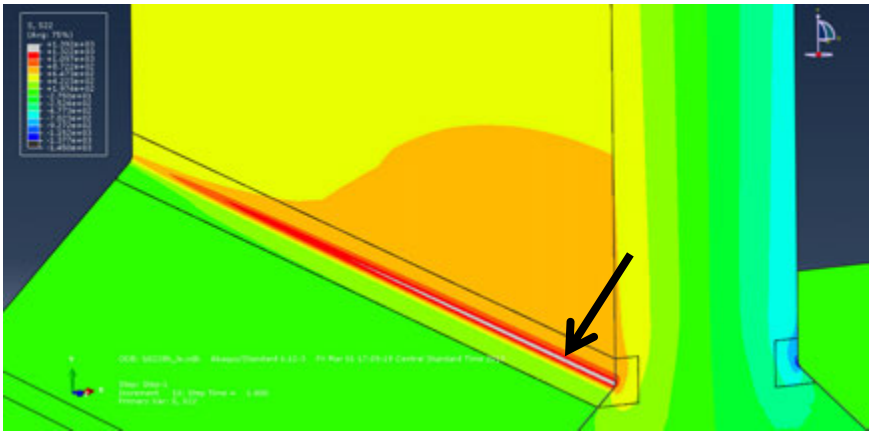

Figure 65) The white region, marked by the black arrow, in the FEA model highlights the length of the hot spot region. The hot spot stress is defined at 95% of the peak stress.

The log-normal probability plot of the worst case Kt (i.e. maximum value) for a 50 mm hot spot is shown in Figure 66. The log-normal distribution is again an adequate fit to the data, with slight deviations occurring at values less than 2% probability of failure on the low end and greater than 99% probability of failure on the high end. In other words, the probability

distribution is underestimating the predicted stress concentration Kt on both the low and high ends. The descriptive statistics of the distribution of the worst-case value of Kt for a 50 mm hot spot is shown in Table 5.

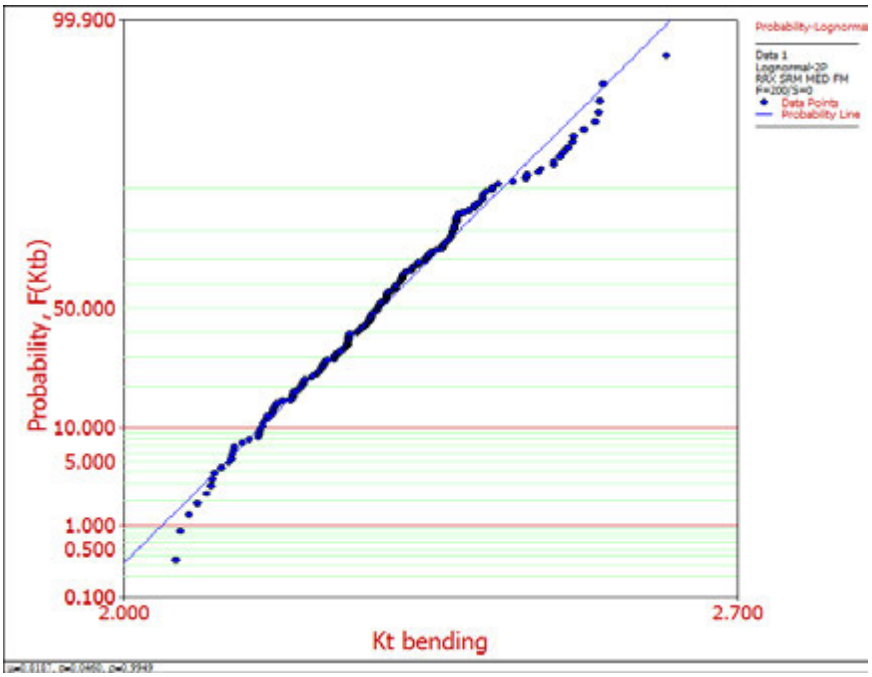

Figure 66) Log-normal probability plot of the case Kt values

Table 5) Table showing the worst-case Kt distribution based on a 50 mm hot sport length.

	Distribution type	Mean	Standard Dev.
Kt bending	Log-normal	2.267	0.0460

The distribution of the 50 mm hot spot worst case Kt was used to calculate the new probability of failure for each of the load levels. The distribution of Kt, along with the weld hot spot length, can then be used to calculate the distribution of the peak stress.

Calculation of Weld Hot Spot Stress:

Figure 67 shows the plot of the linear elastic stress distribution through the thickness for a 2980N load from the FEA model in the principle stress direction. The principle stress is perpendicular to the weld toe which is the direction that causes mode I loading on the weld toe. The trend line shown is plotted for the stress between 25% and 75% of the measured thickness, the region Goyal found to be independent of the weld stress concentration factor (94). The weld hotspot stress is the intercept of the yellow trend line, which is 195 MPa

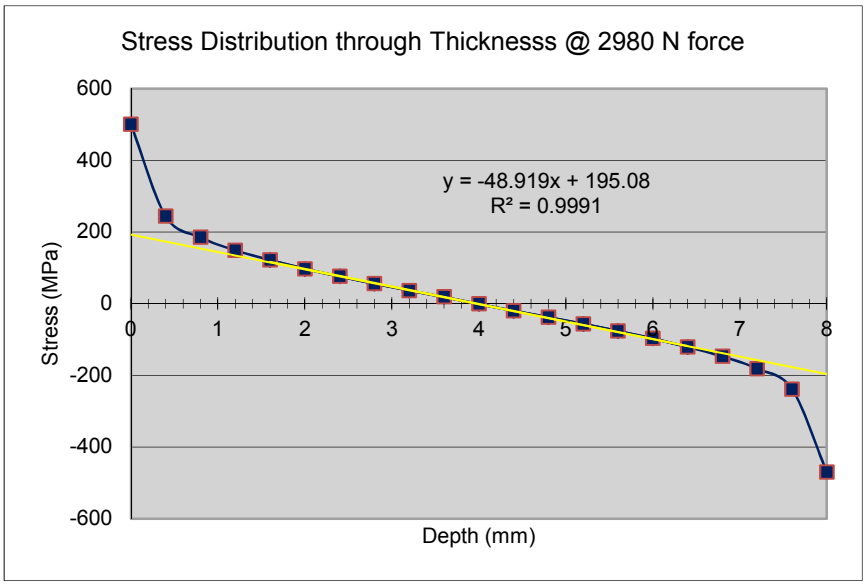

Figure 67) Example of stress distribution and hot spot calculation for 2980 N load.

Since the FEA model used to calculate the hot spot stress is linear elastic, the elastic stress can be directly scaled to the lower input loads. The scaled hot spot stresses based on the load levels are shown in Table 6. These values, along with Kt, will be used to determine the peak stress distribution.

Table 6) Hot spot stress calculated for the tested load levels

Load (N)	Hot Spot Stress (MPa)
2980	195.1
2669	174.7
2224	145.6

Material Properties:

The variation in the material properties come from the variation in the experimental strain life fatigue test data. Even when great lengths are taken to ensure reproducibility in testing fatigue samples variation still occurs.

This section will examine the results of the fatigue testing and the calculation of the fatigue material properties. Strain life fatigue data will be addressed first, followed by a description of how data was fir to the strain life curve. Finally, the manner by which the fatigue properties were acquired and scaled to account for the difference between the T-weld material and the material used in the experimental strain life testing will be discussed in the next section.

Strain life fatigue data:

As mentioned previously, the material used in the T-welded samples was of a different thickness and from a different heat than the material used for the experimental fatigue strain life testing. The procedure for testing to obtain the strain life properties is provided in ASTM E606, and only a brief overview of the procedure is provided here. When tested under strain control conditions samples are pulled in tension to a designated strain level then placed under compression to the negative amount of the same strain. The stress/strain response is measured at

a predetermined interval based on the expected life of the sample, and the number of cycles until failure is recorded.

The parameters needed to fit the strain life curve are the total strain, the stress amplitude, modulus of elasticity and the number of cycles. The test values for this material are shown in Table 7. The total strain is designated in the test set up, since the test is run in strain control, and the number of cycles is recorded upon failure. The modulus and the stress are calculated from the half-life hysteresis loop while the stress is the stress that was applied to reach the designated strain level. The modulus of elasticity (E) is calculated from the linear region of the unloading portion of the hysteresis loop. While the modulus of elasticity in theory is a material constant, in reality there is always test measurement variation. The modulus is used to calculate the elastic strain, which is used to fit the elastic portion of the stain life curve. The average modulus calculated from the individual tests is used to calculate the elastic strain. The plastic strain, which is used to fit the plastic portion of the strain life curve, is the difference of the total strain and the elastic strain.

Table 7) Material Property Fatigue Test Data

Strain (mm/mm)	Stress (MPa)	Reversals (2Nf)	Modulus at Half-life (GPa)
0.0045	375.8	22510	198.4
0.004	365.5	30216	200.4
0.004	360.3	31370	196.8
0.0035	346.3	37200	201.9
0.0032	343.1	47752	203.4
0.003	332.6	64330	203.1
0.003	335.9	83786	198.6
0.0027	319.6	85608	208.2
0.0025	320.7	114328	203.9
0.0024	317.7	135130	207.6
0.0023	315.4	172890	204.0
0.0022	310.9	251900	211.0
0.002	304.3	341486	212.7
0.002	302.6	551244	208.3
0.0019	295.5	1070224	217.1
0.0018	285.9	1982238	206.4
0.0018	281.4	3026720	210.6
0.0015	267.7	5000000	192.2

Fitting the data to strain life curve

The strain life curve parameters, also referred to as the Manson-Coffin parameters, are shown in Figure 68. The pink line is the fit for the elastic portion of the curve and the blue line is the fit for the plastic portion of the curve. The dashed lines on either side of the lines mark the 95% confidence interval for the curve.

All of the test data is presented on the graph, but only the filled circles are used in the fitting. There are several reasons for the exclusion of data. Firstly, the run out samples where the sample did not failed after 2.5 million cycles are not included in the fitting because they artificially flatten the slope of the elastic portion of the curve. Points of this nature are highlighted by the green circle in Figure 68b. Secondly; the points on the plastic curve that have a plastic strain less than the error of the extensometer are excluded due to uncertainty in the data.

These include the points highlighted in red in Figure 68. Thirdly, data was excluded where the sample failed in a manner inconsistent with the test criteria, such as happens when failure initiates outside the gauge section. This data is always suspect since it is assumed a significant flaw had to have existed otherwise failure should have initiated in the gauge length. The points highlighted in light blue designate these points. Finally, points that appeared as outliers from the general trend of the data were excluded. These points are highlighted by dark blue in Figure 68b.

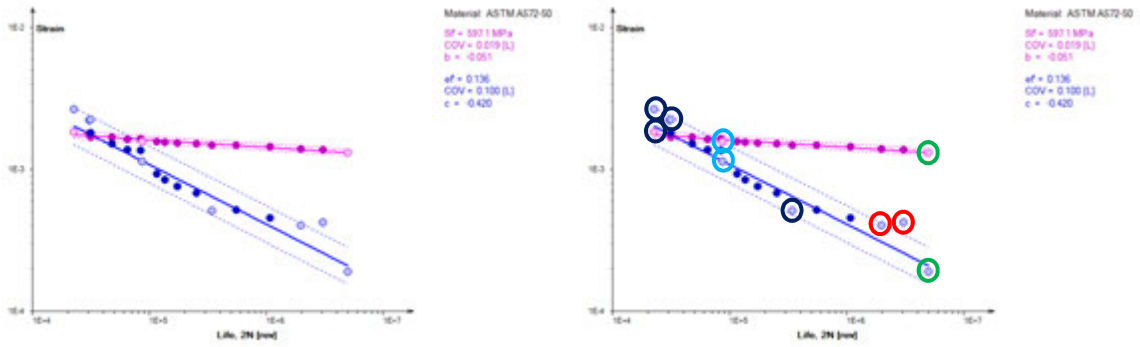

Figure 68) Manson-Coffin fitting parameters

The same points that were excluded from the Manson-Coffin parameters were also excluded from the cyclic stress strain curve fit. The cyclic stress strain curve fit to calculate the Ramberg-Osgood parameters is shown in Figure 69.

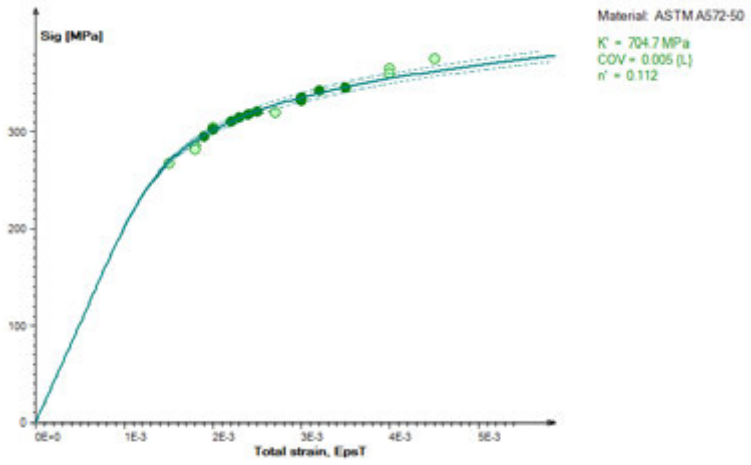

Figure 69) Cyclic stress strain curve showing the Ramberg-Osgood parameter fitting

Scaling material properties:

Table 8 provides the monotonic strength data for the material used for the T-welds as compared to the material used in the experimental strain life fatigue testing. This data was measured from samples cut from each of these sets of sample materials and the monotonic properties measured using a uniaxial tension test. As seen from Table 8, the material used for the strain life testing has a higher strength than the material used in the T-weld samples, therefore, material properties for the T-weld samples were scaled down using the method described in the section 7.2 Experimental procedure. The results are shown in Table 9.

Table 8) Monotonic properties of both the material used in the T-weld and the material used in the strain life testing.

Property	T-weld Material	Strain Life Material
Yield Strength (0.2%) (MPa)	360	419
Ultimate Strength (MPa)	462	529

Table 9) As tested and scaled strain life material properties

Fatigue Parameters	Original Properties	Scaled Material Properties	COV
sigma f' (MPa)	597.1	521.5	0.019*
b	-0.051	-0.051	
ef'	0.136	0.136	0.100*
c	-0.420	-0.42	
K' (Mpa)	704.7	615.4	0.016*
n'	0.112	0.112	

* indicates log-normal distribution

Residual Stress

The simulated residual stresses were not used in this portion of the analysis. It was found that residual stress state had changed in the part after they had been cut into the fatigue samples. The changes are due to the stiffness change from the change in geometry. For this reason the measured residual stress state was used in the life predictions. These values are shown in Section 6.2 and shown in Table 2

A total of 10 measurements were used to determine the residual stress distribution. Ideally a larger number of measurements is preferred for an accurate statistical sampling, but the total number was limited due to the time intensive neutron diffraction method used to measure the stress.

Both the initial residual stress and stress after cycling were considered. The cumulative density functions (CDF) of both the initial stress and the stress after 100 cycles are shown in Figure 70. The CDF shows the probability that a value will be less than or equal to the residual stress value depicted on the X-axis. The red line on the chart shows the calculated value for the CDF whereas the blue bars are the actual test results. Deviation from the normal distribution function used for the CDF and the actual data occurs where the red line deviates from the blue bars. These graphs show that the normal distribution probability function models the residual

stress distribution fairly well, although more data points are needed to fully classify the distribution. The descriptive statistics of both these distributions are shown in Table 10.

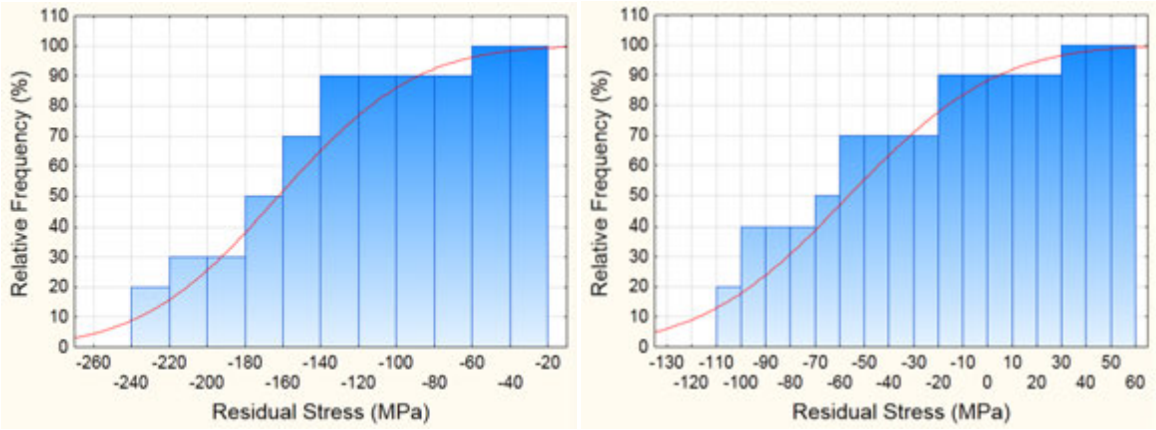

Figure 70) Cumulative density function of the a) residual stress at 0 cycles and b) residual stress at 100 cycles.

Table 10) Descriptive statistics for residual stress distribution

Sample	Mean	Max	Min	Standard Deviation
0 Cycle RS (MPa)	-162.3	-239.8	-43.5	57.5
100 Cycle RS (MPa)	-56.2	-105.9	39.2	47.6

The distribution of the residual stresses can now be used to determine the fatigue life distribution. It should be noted that measurement error associated with neutron diffraction was not accounted for in the distribution of the residual stress. As shown in Section 5.3 the measurement error for the neutron measurements was +/- 23 MPa. The error associated in the measurement would not affect the distribution in significant way since the errors are associated with individual results rather than being directly applied to the mean and standard deviation. For this reason they were not included in this section of the analysis.

Fatigue Life Predictions:

The predicted fatigue life distributions from the Monte Carlo simulations where the distributions of the Kt, the strain life material properties, and the residual stresses are used are shown in Figures 71 through 73 for 2890 N, 2669N and 2224 N loads, respectively, the loads used in the experimental fatigue testing. The life prediction data from the Monte Carlo simulations is presented on a probability of failure plot as a log normal distribution. The probability of failure is the statistical likelihood of a failure occurring at a given number of cycles. For each figure, the graph shown in a) on the left gives the predicted probability of failure for a Kt that corresponds to a hot spot length of 5 mm, while the graph shown in b) on the right corresponds to a hot spot length of 50 mm. Three sets of data are shown plotted in each case, corresponding to i) assuming there is no residual stress, ii) with the "0 cycle" stress which is the measured starting residual stress, and iii) with the residual stress measured after 100 cycles after redistribution of the stress has occurred. Note that the residual stress data used in these predictions is presented in Table 2 in Section 6.3. The results of the three loads will be discussed in turn.

2980 N load level: The predictions for this load level are shown in Figure 71**.** For the 5 mm hot spot Kt the minimum fatigue life is predicted for the condition with no residual stress . This is expected since the residual stress present was measured to be compressive, which is known to increase fatigue life. It is interesting to see that the prediction for the 100 cycle life distribution, which has a more positive residual stress (less compression), does not always have a shorter life than the 0 cycle residual stress which has much more compressive stress. The deviation is not limited to just the tail end where deviation could be explained by errors, but occurs at a probability of failure of 40%.

The predictions using the 50 mm hot spot Kt (Figure 71b) show less spread in life between the three stress states than Figure 71a. The predictions using the 100 cycle and 0 cycle (i.e. as-measured) residual stress state are very close. The 0 cycle condition, where the maximum compressive stress is used, predicts longer lives in all probabilities of failure. In this case it is interesting that the "no RS" and the "100 cycle RS" curves cross.

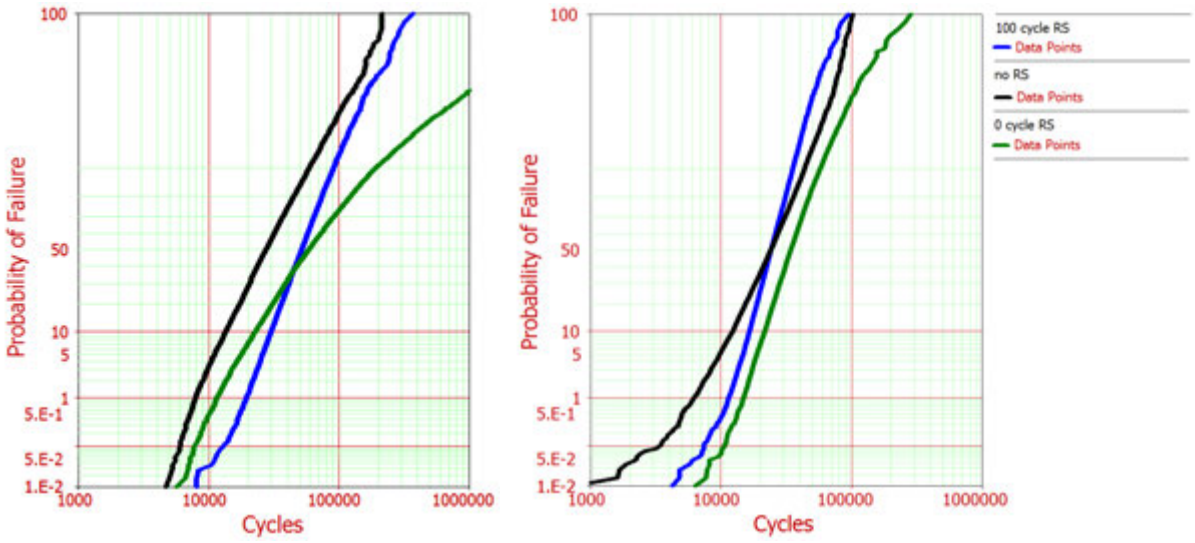

a) b)

Figure 71) Probability of failure plot at 2980 N for Kt of a) a 5 mm hot spot; b) a 50 mm hot spot.

2669 N load level: The 5 mm hot spot Kt graph shown in Figure 72a shows results similar to the 2980 N load level with the "No RS" prediction giving the shortest life. A transition is again seen between the "100 cycle" and "0 cycle" residual stresses, a conservative estimate being that it occurs at a probability of failure of approximately 30%. This is a much lower probability of failure than the 40% predicted at a 2980 N load.

The Kt for a 50 mm hotspot, Figure 72b, shows only a slight difference between the “no residual stress” and “100 cycle” residual stress situations at the higher probabilities of failure, although the deviation is greater at the lower probabilities of failure. At this load level the “0 cycle” residual stress prediction is much further to the right than for the 2980 load, which indicates that using the measured compressive residual stress distribution has a larger effect on the life at this lower load level.

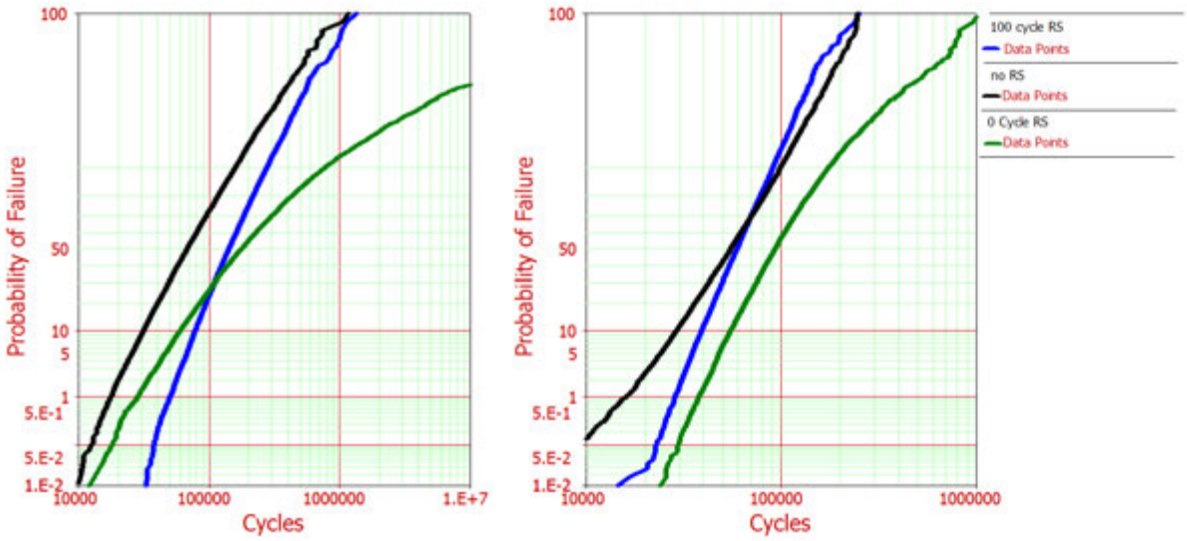

a. b.

Figure 72) Probability of failure plot at 2669 N for Kt of a) a 5 mm hot spot; b) a 50 mm hot spot.

2224 N load level: Observation of the 2224 N load level results shown in Figure 73 reveals a large degree of separation between the life predictions curves when considering the residual stress state using the 5 mm hot spot size Kt. This would indicate that residual stress has a larger effect at lower applied stress and Kt levels. The slopes of the ”No RS” and “100 cycle RS” are very similar, although the “100 cycle” residual stress curve is shifted to the right of the

"0 cycle" residual stress predictions. At very low probabilities of failure the "0 cycle" residual stress starts to approach the "100 cycle" residual stress, but these probabilities of failure are very low.

When comparing the results with the higher Kt from the 50 mm hot spot length for "100 cycle" residual stress and "no RS" it can be seen that the predictions have very similar curve shapes at probabilities of failure between 10 and 90%, although the "no RS" curve is always to the left of the 100 cycle residual stress curve. More significant deviations in slope occur at either end of this range. The "0 cycle" residual stress prediction is much further to the right of the other two curves and, as for the 5 mm hot spot data, shows a much greater curvature in predicted performance.

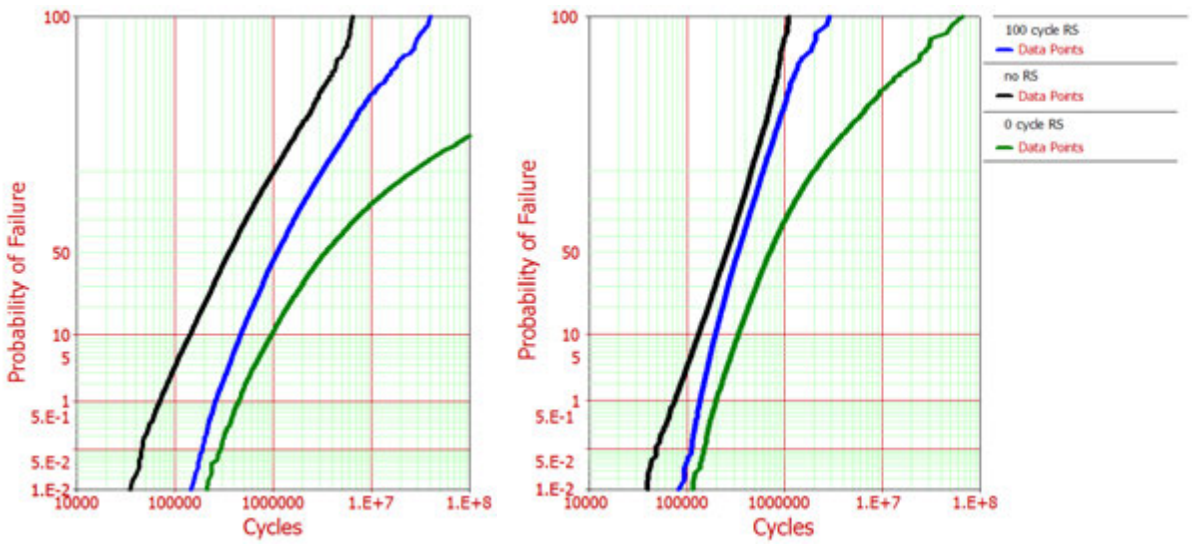

a. b.

Figure 73) Probability of failure plot at 2224 N for Kt of a) a 5 mm hot spot; b) a 50 mm hot spot.

Fatigue Testing Results:

With the life predictions from Figure 71 through Figure 73 in hand it is now time to compare the predicted values to those obtained from actual experimental tests. For this experiment twenty-one T-welded samples were tested at the three different loads of 2224, 2669 and 2980 N. The fatigue samples, as described in Section 3.2, Fatigue Testing and Measurements, were cycled until a crack was detected visually. The intent was to catch the crack when it first appeared, but this did not work out as planned. The high stress concentration coupled with a less then optimum detection method resulted in a high variability in the first recorded crack length. To overcome this, the number of cycles was recorded when the crack reached 100 mm in length in order to provide a consistent measure between results. This length was detected through setting displacement limits on the stroke of the actuator used to provide the input load. As the crack grows the compliance of the sample changes and a greater actuator stroke is needed to reach the same load. This was a good way of ensuring a consistent crack size at the end of life.

Figure 74 shows the results for the load vs. number of cycles required to reach a crack size of 100 mm in length for the T-weld fatigue testing. The data shows a wide variation in life at each of the load levels of up to 10 times from minimum to maximum life. The individual fatigue test lives are provided in Tables 11- 13.

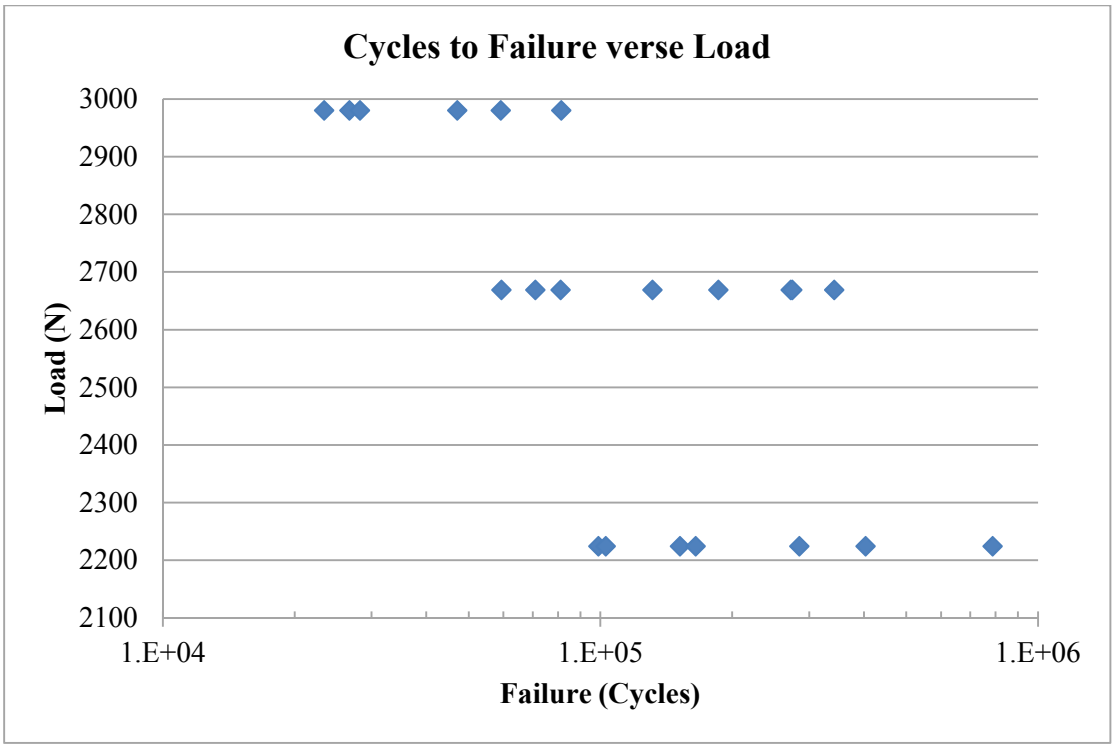

Figure 74) Load vs. number of cycles for a 100 mm crack.

Table 11) Test results and probability of failure of the test samples for 2980 N load level.

Sample	Load (N)	cycles to failure
20-3	2980	23,387
26-2	2980	26,724
20-1	2980	28,221
26-3	2980	47,130
17-3	2980	59,242
1-3	2980	81,414

Table 12) Test results and probability of the test samples for 2669 N load level.

Sample	Load (N)	cycles to failure
12-3	2669	59,427
25-1	2669	71,070
19-3	2669	81,116
22-1	2669	131,502
13-3	2669	186,015
7-2	2669	272,270
29-3	2669	274,803
19-1	2669	342,390

Table 13) Test results and probability of the test samples for 2224 N load level.

Sample	Load (N)	cycles to failure
14-2	2224	98,937
11-2	2224	102,875
14-3	2224	152,067
26-1	2224	165,127
19-2	2224	284,849
28-1	2224	403,777
11-3	2224	787,707

Deterministic life prediction comparison results

When predicting fatigue life it is common to predict a single life value for life of the component. The following analysis presented in this section uses single values for material properties, stress concentrations and residual stresses. As stated previously the goal of this

dissertation is to predict the life distribution, i.e. the entire range of values that might be expected. However, to begin, a comparison of a single value, deterministic life prediction to the experimental data will be discussed in detail in this section. The ***mean value of the input variables*** is the most common method of applying this type of fatigue analysis. For this reason it is critical to understand how the deterministic prediction method compares to the actual experimental test data since in practice this method is the most common.

The first comparison is to look at the life predictions using the mean values for the input parameters of Kt, strain life properties and the residual stress. This data is presented in Table 14. The percent difference in Table 14 compares percent deviation of the predicted life to the average experimental test life. The closer the deviation is to 0 the better; a positive number indicates that the predicted life is longer than the experimental test life (classified as non-conservative estimates), and a negative number indicates that the prediction gives lives that are shorter than the test life (i.e. conservative).

Since the distribution functions for the input parameters of Kt, strain life properties, and residual stress are not all normally distributed around the mean value, it is not surprising that life prediction of Table 14 using mean values of the input variables do not match the 50% probability of failure. For this reason the average life from the predictions were also evaluated against the median test life. Table 15 shows the comparison of the average experimental test life to the predicted life corresponding to a 50% probability of failure. The same evaluation criteria explained for the average values is used for the median values.

The results for each load level are summerized in turn in the next sections.

Table 14) Comparison of the fatigue life predictions with the mean values for the input variables versus the average fatigue life of the experimental samples. The closest predictions are highlighted in yellow.

	Load			***Percent difference***		
	2224 N	**2669 N**	**2980 N**	**2224 N**	**2669 N**	**2980 N**
Average Cycles to Failure	285,048	177,324	44,353			
50 mm hot spot with 0 cycles residual stress	441,488	66,437	25,125	55%	-63%	-43%
50 mm hot spot with 100 cycle residual stress	241,698	45,738	18,728	-15%	-74%	-58%
50 mm hot spot with no residual stress	170,193	36,310	15,382	-40%	-80%	-65%
5 mm hot spot with 0 cycles residual stress	2,104,632	199,655	64,303	638%	13%	45%
5 mm hot spot with residual stress 100 cycles	881,203	121,799	44,025	209%	-31%	-1%
5 mm hot spot with no residual stress	535,965	90,960	35,109	88%	-49%	-21%

Table 15) Comparison of the median fatigue life from the predicted distribution and the average experimental test life. The closest predictions are highlighted in yellow.

	Load			***Percent difference***		
	2224 N	**2669 N**	**2980 N**	**2224 N**	**2669 N**	**2980 N**
Average Cycles to Failure	285,048	177,324	44,353			
50 mm hot spot with 0 cycle residual stress	706,675	92,846	34,181	148%	-48%	-23%
50 mm hot spot with 100 cycle residual stress	334,171	59,223	24,112	17%	-67%	-46%
50 mm hot spot with no residual stress	255,034	54,863	23,955	-11%	-69%	-46%
5 mm hot spot with 0 cycle residual stress	3,399,853	175,938	58,591	1093%	-1%	32%
5 mm hot spot with 100 cycle residual stress	1,096,194	141,746	51,791	285%	-20%	17%
5 mm hot spot with no residual stress	354,644	67,845	27,521	24%	-62%	-38%

2224 N load samples

Analysis of Table 14 shows that for the 2224 N load the most accurate life predictions are made using the Kt for a hot spot of 50 mm and a low residual stress as seen after 100 cycles and/or the simulation with no residual stress. The lower Kt for the 5 mm hot spot over estimates the life, which is never desirable when predicting reliability. Comparing the results in Table 14 also show that fatigue life in the high cycle region, or in other words, the lower stress region, is more sensitive to the residual stress state. At the lower Kt of the 5 mm hot spot size the life predictions are impacted dramatically by the different residual stress conditions. This shows that the higher values of Kt for the larger hot spot length are needed for accurate predictions.

Clearly, the compressive residual stress coupled with the lower Kt has a dramatic effect on the life prediction.

When looking at the median value data from the predicted life distribution (Table 15) the 50 mm hot spot with 100 cycle residual stress is now slightly non-conservative and the 50 mm hot spot with no residual stress is closest a -11% deviation. The lower Kt with the 5 mm hot spot stress results in prediction that are very conservative.

2669 N load samples

When looking at the 2669 N load level the life predictions obtained using mean input parameters the best correlation to experimental data are for the lower stress concentration Kt of the 5 mm hot spot length and the high residual compressive stress at the original stress condition. In this case the values of the life prediction are not heavily dependent on the residual stresses state. The difference between the prediction with the high compressive stress at "0 cycles" and the residual stress at "100 cycles" is a swing of 31% on the conservative side for the residual stress at "100 cycles" to 13% on the non-conservative side for the residual stress for the at "0 cycles". When this is compared to the median life, the life prediction using "100 cycle" residual stress are within 20% of the experimental values on the conservative side and within 1% on the conservative side of the test life when using the no residual stress.

2980 N load samples

When looking at the 2980 N load level the life predictions with the best correlation to experimental values when using the mean properties for the input parameters for residual stress, Kt and material properties with lower stress concentration of the 5 mm hot spot length and the

lower residual stress after “100 cycles” when comparing mean input parameters. The life prediction with the highly compressive initial residual stress and the lower Kt of the 5 mm hot spot stress length over estimate the life by 45%, while the prediction using the “100 cycle” residual stress was within 1% of the actual value. For the median life prediction compared to the experimental average life the estimations are non-conservative by 17%, i.e. the result is an overestimation of life when using the 5 mm hot spot with 100 cycle residual stress and a 38% underestimation when using the residual stress present 5 mm hot spot with no residual stress

Establishment of baseline in deterministic life predictions

As seen from Figure 74 there is always considerable scatter in experimental fatigue test results. It is difficult to compare these results without understanding the amount of expected deviation between the fatigue life prediction and the test data. To provide this baseline for subsequent discussions it is reasonable to look to the individual tests used to fit the strain life curve, which was presented in Table 7. Firstly, the fatigue life of each of the test specimens from the strain life curve is predicted using the strain life technique. The results of the prediction are then compared to the actual experimental test life to obtain a percent deviation. The results of deviation in predicted life verse actual test life are shown in Table 16. Although not all of these results were used in the material property fit, the data does show that even with very controlled conditions experimental fatigue life tests can vary between an over prediction of 74% to an under prediction of 58%.

Table 16) The percent difference for the test results from the strain life material property testing.

Strain Level (mm/mm)	Stress Level (MPa)	Predicted Life (cycles)	Test Life (Cycles)	Percent Difference
0.0045	375.8	6085	11255	-46%
0.004	365.5	9452	15108	-37%
0.004	360.3	9452	15685	-40%
0.0035	346.3	16160	18600	-13%
0.0032	343.1	24820	23876	4%
0.003	332.6	31770	32165	-1%
0.003	335.9	31770	41893	-24%
0.0027	319.6	54810	42804	28%
0.0025	320.7	78190	57164	37%
0.0024	317.7	97750	67565	45%
0.0023	315.4	124200	86445	44%
0.0022	310.9	161800	125950	28%
0.002	304.3	297600	170743	74%
0.002	302.6	297600	275622	8%
0.0019	295.5	424800	535112	-21%
0.0018	285.9	635100	991119	-36%
0.0018	281.4	635100	1513360	-58%

Probabilistic life prediction results

While comparison of single-value life predictions is instructive, the goal of this dissertation has been to compare the predicted fatigue life distribution to the experimental test life distribution. This is attempted in Figures 75 through 77, where the experimental results were plotted on the same set of axes used for the life prediction distributions. As a reminder, the predictions determined using the 5 mm hot spot Kt are shown on the left side of each figure noted by “a” and the 50 mm hot spot Kt is shown in the right side of each figure noted as “b”. The actual experimental results are denoted in pink.

At the 2224 N load the test data for the 5 mm hotspot length falls to the left of all the life predictions. When looking at the 50 mm hot spot length the life prediction lies between the no

residual stress and 100 cycle residual stress life distribution predictions. At the 2669 N load level the test distribution matches very well with the 100 cycle residual stress distribution with the 5 mm hot spot length Kt. The 50 mm hot spot length provides predicted distributions that are conservative in all cases. When looking at the 2980 N load level the predicted distributions match fairly well with both the 5 mm and 50 mm hot spot length Kt. The lower Kt of the 5 mm hot spot length and the 100 cycle residual stress match very well, but the prediction are non-conservative where the 50 mm hot spot length with the 0 cycle residual stress match very well and are conservative in nature.

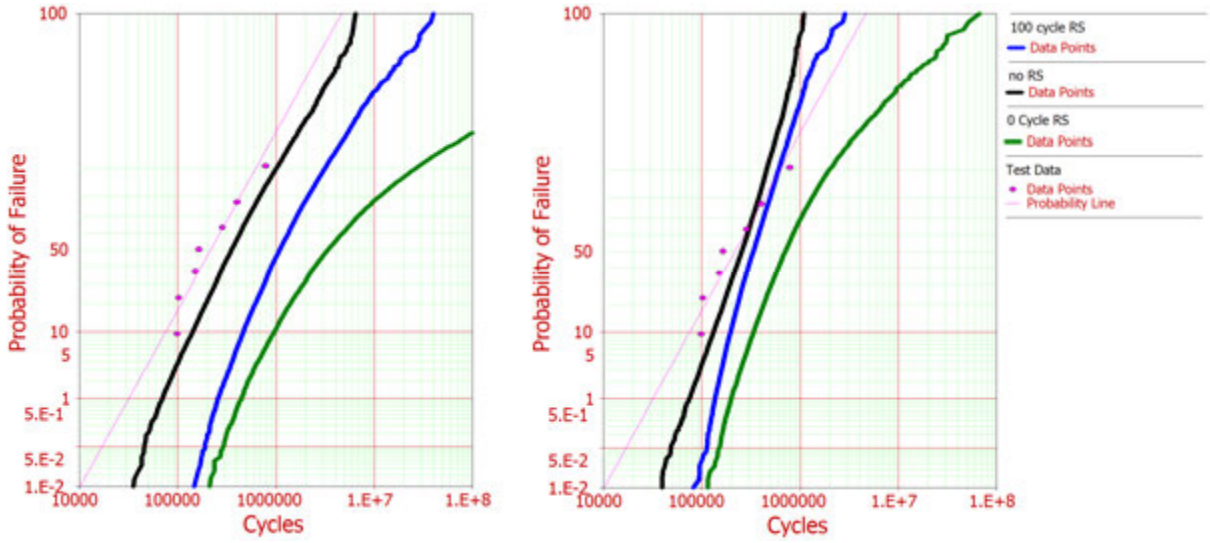

a) b)

Figure 75) Probability of failure plot at 2224 N for Kt of a) a 5 mm hot spot; b) a 50 mm hot spot.

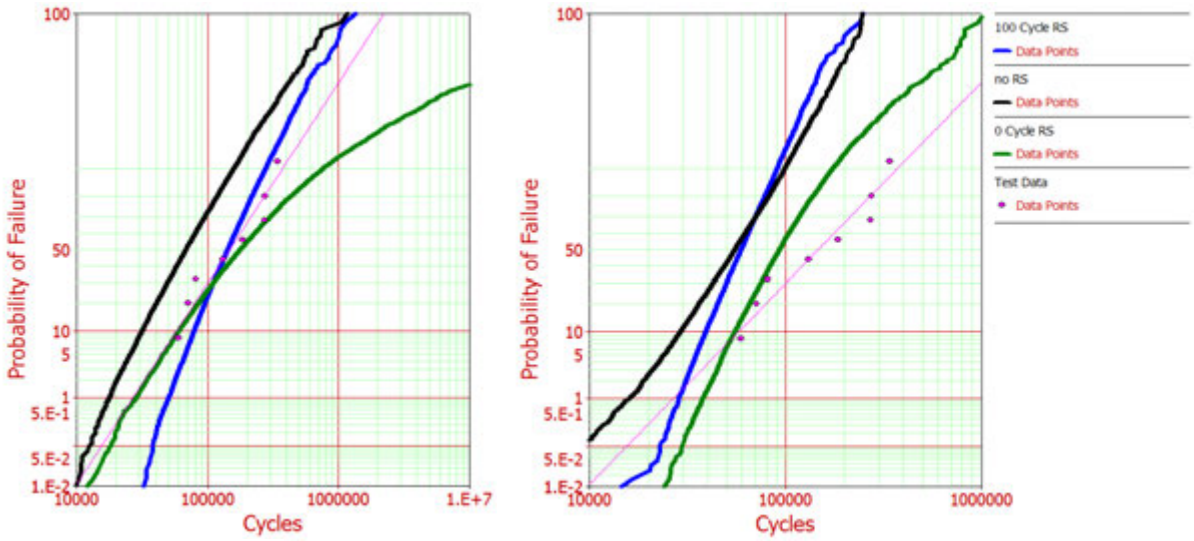

a) b)

Figure 76) Probability of failure plot at 2669 N for Kt of a) a 5 mm hot spot; b) a 50 mm hot spot.

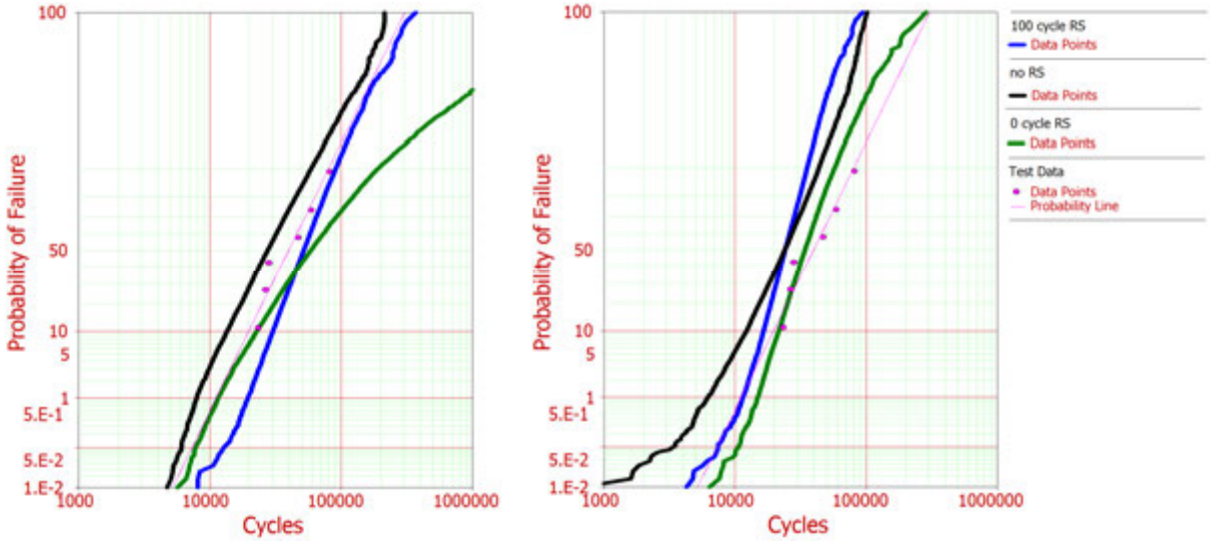

a) b)

Figure 77) Probability of failure plot at 2980 N for Kt of a) a 5 mm hot spot; b) a 50 mm hot spot.

7.4 Discussion

As stated in the introduction, the goal of this chapter is to predict the fatigue life distribution for a welded joint by incorporating the statistical distribution of the input parameters. The process and experimental procedures discussed in chapters 2 and 3 have demonstrated the complexity of this process. Distributions for all the input parameters were determined as accurately as possible through measurement and statistical assessment of the results. This allowed life predictions to be made. The results of these predictions will now be discussed, both in terms of how well the predictions matched experimental data and how the choices made during specific stages involving experimental measurement and data acquisition are believed to have affected the accuracy of the results. The latter discussion primarily concerns the impact the selection of hot spot length has on the Kt.

Hot Spot Length and Stress Concentration Distribution:

As shown in Figure 62, the weld toe angle and radius have very little correlation. This allows each to be treated as independent variables in the Monte Carlo simulations to calculate the distribution of the stress concentration. The simulated stress concentration distribution, as shown in Figure 64, fits a log normal distribution very well although the fit is non-conservative (i.e. gives lower predicted Kt values than the measured distribution) on both the low and high ends of the probability curve. This means that for the majority of the data, a log normal distribution could be used with satisfactory results expected. However, the estimated life length at low and high probabilities of failure is not only inaccurate but worse, non-conservative. This is a concern when considering part design, where from a consumer satisfaction / safety standpoint because it is better to under predict fatigue life than over predict the life.

FEA analysis of the weld used in this series of experiments shows that the high stress region (i.e. the hot spot) extends across the weld line as shown in Figure 78. The stress contour in Figure 78 shows that the high stress does not extend fully across the sample; it is limited to a portion of the full length. As presented in the results section of this chapter, the hot spot length affects the likelihood of having a worst case Kt (determined by the weld geometry) in the high stress region. Clearly, the longer the hot spot length the higher the probability of having a high Kt at a critical location. Since the distribution for the weld Kt was measured with a repeating spacing of 5 mm, a single sampling of the Kt distribution would represent a hot spot length of 5 mm, which is not the case for the T-weld sample geometry used, as revealed by FEA. One question this presents is "how should the hot spot length be defined?"

A possible solution is to define the hot spot length that needs to be considered as a percentage of the peak stress. For example, FEA analyses will typically produce simulations of various shadings showing stress levels as a function of location of the modeled part. Although images such as these qualitatively reveal the high peak stress regions, they do not pinpoint those regions where the stress is high enough to actually cause fatigue damage. It is entirely possible that a highly stressed region exists in a part of the weld with little local stress concentration, while a high local stress concentration exists in a lower stressed region that can lead to fatigue. In other words, when stress concentration is considered the region that must be considered will be lower than the peak stress. One is then left with the problem of determining what percentage of the peak stress needs to be considered. Clearly, as the percentage of the peak stress that must be considered increases the physical size of the hot spot as predicted by FEA will decrease.

To decide on the definition of what peak stress to use the difference the region at the weld toe predicted by the FEA as having a peak value for stress is taken as a starting point, then the percentage of this region that really should be included in the analysis is considered. As the percentage included is lowered the length of the hot spot stress is increased. The FEA shown as an example in Figure 78 was prepared using the weld geometry of a 0.5 mm radius, 45° weld angle, and input load of 2980 N. This simulation is used as an example and is not representative of the stresses used in the life predictions. Because the simulation used a fine mesh 3D model the peak stress that must be considered can be directly shown without having to use the stress concentration as with the previous FEA model. The peak stress from the fine mesh linear elastic model is 1392 MPa and the region that exists at or above 95% of this peak stress is shown in white. If the hot spot length is defined as being the region where the stress is at or greater than 90% of the peak stress, then one need only consider the length along the weld line where the stress was above 1252 MPa. This is done in Figure 79, which also shows a comparison of hot spot length that is 85% or greater of the peak stress. For the definitions used in Figure 78 and 79, the length of the hot spot ranges from a minimum of approximately 53.2 mm in length (95% or greater of the peak stress) up to a maximum of 74.2 (85% or greater).

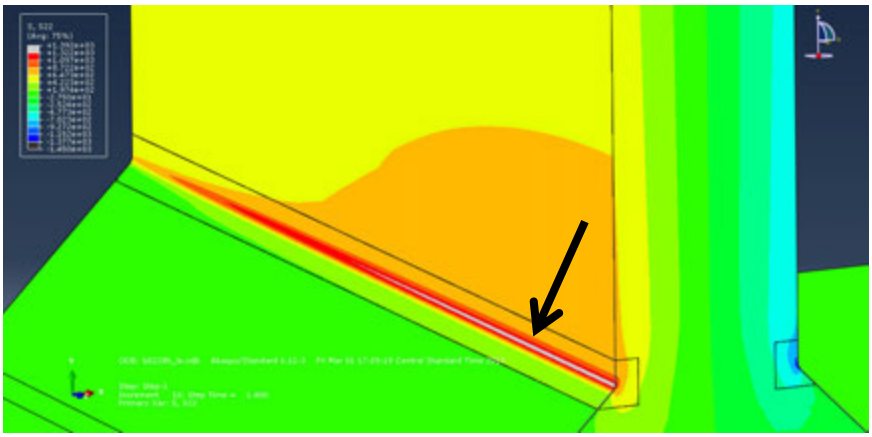

Figure 78) FEA analysis showing the region that is within 5% of the peak stress. The peak stress region (in white) is indicated by the black arrow.

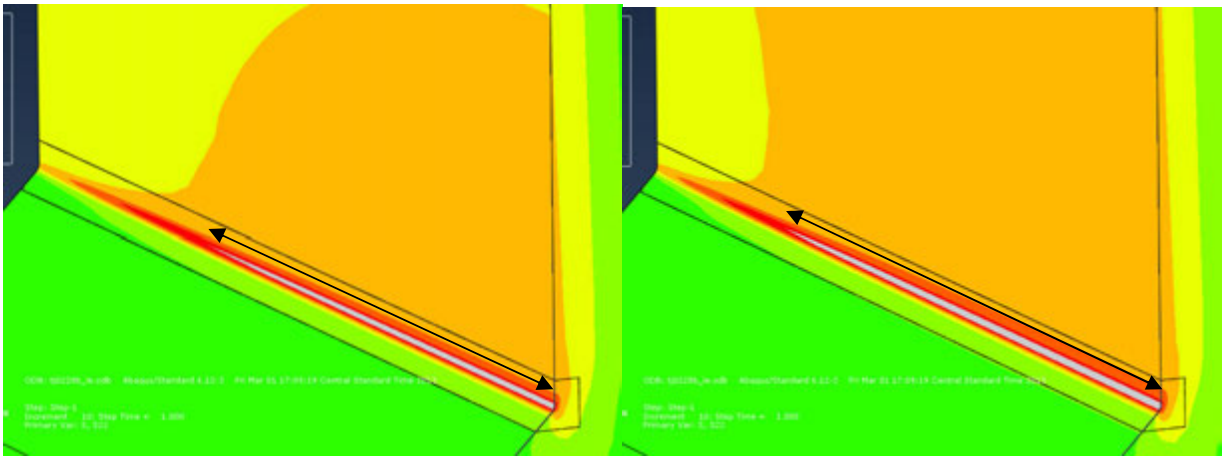

a) b)

Figure 79) FEA analysis showing difference in the length of the hot spot stress as a function of the definition of percent of peak stress. A) 90% B) 85%.

Clearly, the length of the hot spot can vary considerably depending upon how one wishes to define it in terms of the peak stress. The wider range of stress considered the larger the area that must be considered when calculating the Kt. In order to have an accurate Kt value and therefore a fatigue life prediction the length of the hot spot stress needs to be considered.

The procedure described in Section 7.2 Experimental Procedure was used in an attempt to account for the stress concentration dependence on the hot spot length by estimating Kt using a Monte Carlo Simulation run multiple times then looking at the distribution of the maximum Kt within each set of iterations. The results of an analysis to look at how the worst case Kt changes with the length of hot spot are shown in Figure 80.

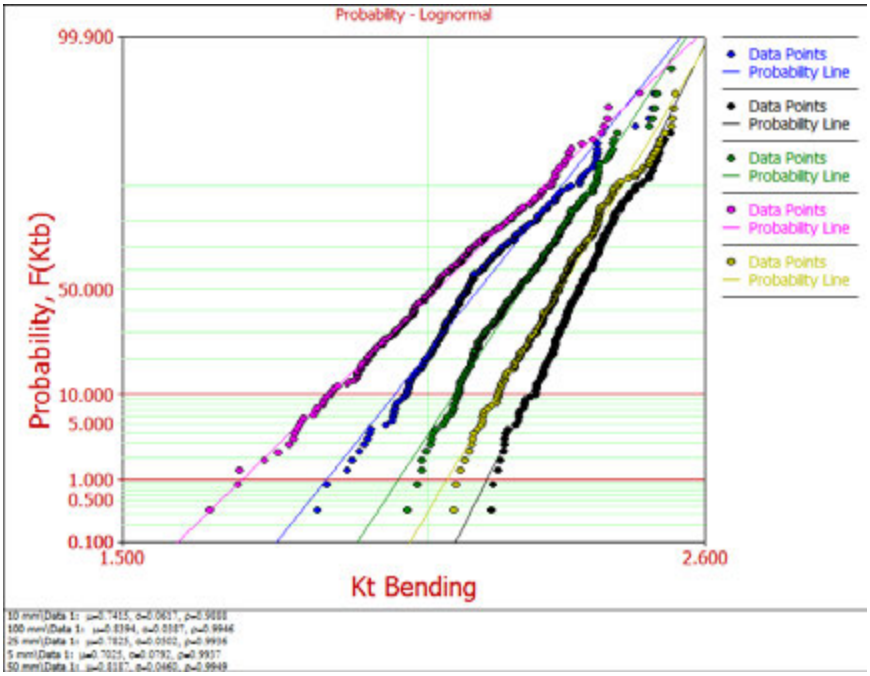

Figure 80) Log-normal probability plots for a hot spot of varying length of 5 (pink line), 10 (blue), 25 (green), 50 (yellow) and 100 mm (black).

Table 17) Descriptive statistics of the Kt distribution at a function of the length of the hot spot.

Hot spot length (mm)	Average Kt	Standard Deviation of Kt
5	2.018	0.0792
10	2.099	0.0617
25	2.187	0.0502
50	2.267	0.0460
100	2.315	0.0387

The probability plots of Figure 80 show that variation in hot spot length is manifested primarily by a change in slope of the curve. As the hot spot stress length is increased variation in Kt is reduced. This indicates even though the variation in the worst case Kt is reduced the mean of the worst case Kt is increased. The consequence of this in life predictions is that as the hot spot length is increased both mean predicted life and total predicted variation in life is reduced.

To demonstrate this, life predictions at the three different load levels that only include the variation in the Kt are shown in Figures 81 through 83. In these plots the slope of the curve indicates the variation in predicted life; the steeper the slope the less variation the distribution has. For example, the slope of the 5 mm hot spot length is less than the slope of the 100 mm curve. Therefore, the 5 mm hot spot length has a higher variation in predicted life than the 100 mm hot spot length. These plots show that the variation in the estimated life increases as the hot spot length is decreased at all loading levels.

Figure 81) Predicted fatigue life distribution as the hot spot length changes at 2224N load.

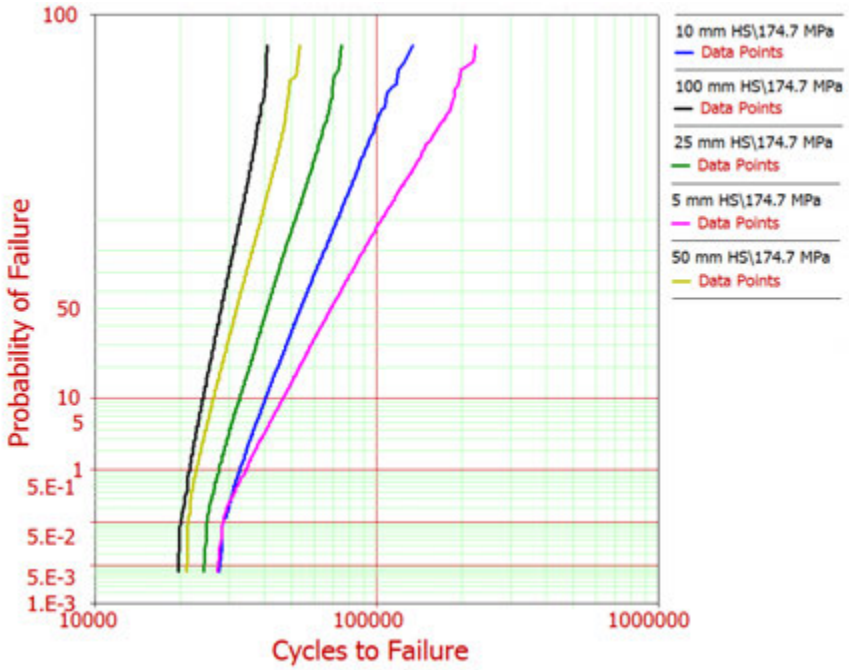

Figure 82) Predicted fatigue life distribution as the hot spot length changes at 2669N load.

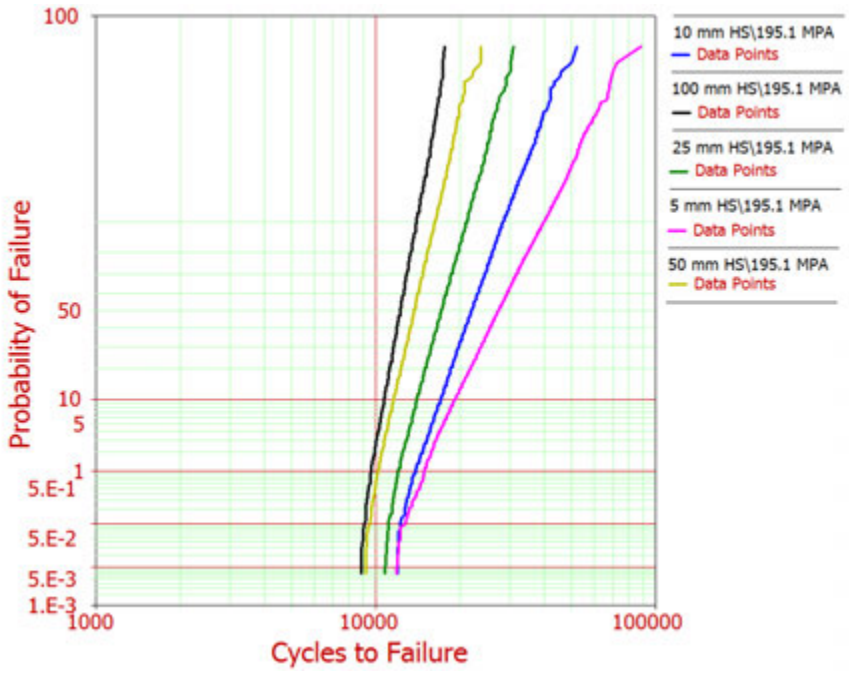

Figure 83) Predicted fatigue life distribution as the hot spot length changes at 2980N load.

Examination of the above figures also shows that the predicted life is relatively insensitive to hot spot length when the length is greater than 50 mm. This is evidenced by examining the difference in predicted life at the 50% probability of failure for the three load levels. As expected the 2224 N load has the highest difference, with the 50 mm Kt being only 16 % larger than the life prediction made with 100 mm Kt. The 2224 N load level is used as a comparison because in all cases it will have the highest amount of variation in the life predictions. The fact that there is only a 16% difference in the fatigue life prediction between the Kt with a 50 mm hot spot and the Kt with a 100 mm hot spot at the load level that has the most variation, shows that above a hot spot length of 50 mm Kt is insensitive to length. When comparing this result to the T-weld discussed here it would be reasonable to conclude that the hot spot stress can be defined the length that exhibits 95% of the peak stress.

In summary, hot spot length clearly makes a difference in life predictions and a method is suggested to account for this but just exactly what percentage of peak stress to use is open to question. In order to fully use the hot spot length further work is required to gain a more in depth understanding on how best to relate hot spot length to Kt.

Fatigue life predictions:

The predicted fatigue life distribution is a function of the residual stress distribution, the stress concentration distribution, and the materials properties distribution. Each of these needs to be assessed to understand the best way to use the data to predict fatigue life distribution. Decisions need to be made as how to use the measured distributions for the best fatigue life predictions and applying those in the life predictions to best predict the life in all ranges. The discussion below will evaluate the use of these distributions by comparing them to the test data.

Deterministic life prediction comparison

In order to have a robust life prediction method what is desired is a standard methodology that provides a slightly conservative estimation of fatigue life that is independent of the loading level. For the data of this dissertation the best results between predicted and experimentally determined life distributions comes when the median predicted values are chosen. The median value of the predicted lives is what would be expected for a large population. The life prediction using the mean values for the Kt and material properties will not be accurate since Kt and the material properties have a log normal distribution around the mean. There are two sets of predicted life data that match the experimental test results the best. The first data set is the Kt for the 50 mm hot spot stress length where the initial residual stress present in the weld has been relaxed after 100 load cycles. When comparing the median life prediction numbers to the experimental test data this condition provides a life prediction that is 17% on the non-conservative side 67% on the conservative side, and 46% on the conservative side for life prediction in the 2224N, 2669N, and 2980 N loads, respectively. The second data set is the 5 mm hot spot length Kt with no residual stress. When comparing the median life prediction numbers to the test data this condition provides a life prediction that is 24% non-conservative side, 62% conservative, and 38% conservative for the loads of 2224N, 2669N and 2980 N, respectively. Both of these sets fall within the variation in the strain life fatigue data that is show in Table 16.

A comparison of all the median value life prediction results is shown in Figures 84 and 85. In general, the life predictions that matched the experimental data the best were those made with lower residual compressive stresses. This indicates that near zero residual stress values can

be used in life predictions to obtain accurate results. If one wants the best life prediction, the data would suggest using the lower Kt from the 5 mm hot spot length and no residual stress**.** For a conservative life prediction at all the load levels one should use a larger Kt and no residual stress. **These results would indicate that stress concentration has a larger role to play in fatigue life predictions than actual absolute residual stress for deterministic life predictions.**

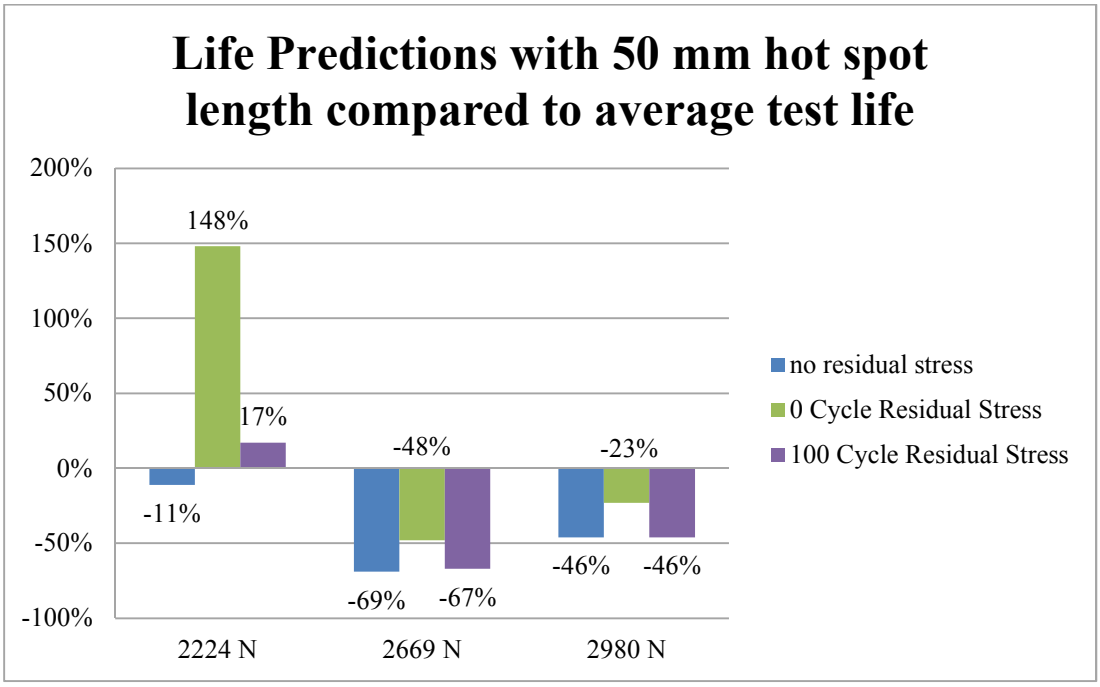

Figure 84) Graphical representation of the life prediction compared to the test life for the Kt derived for a 50 mm hot spot length.

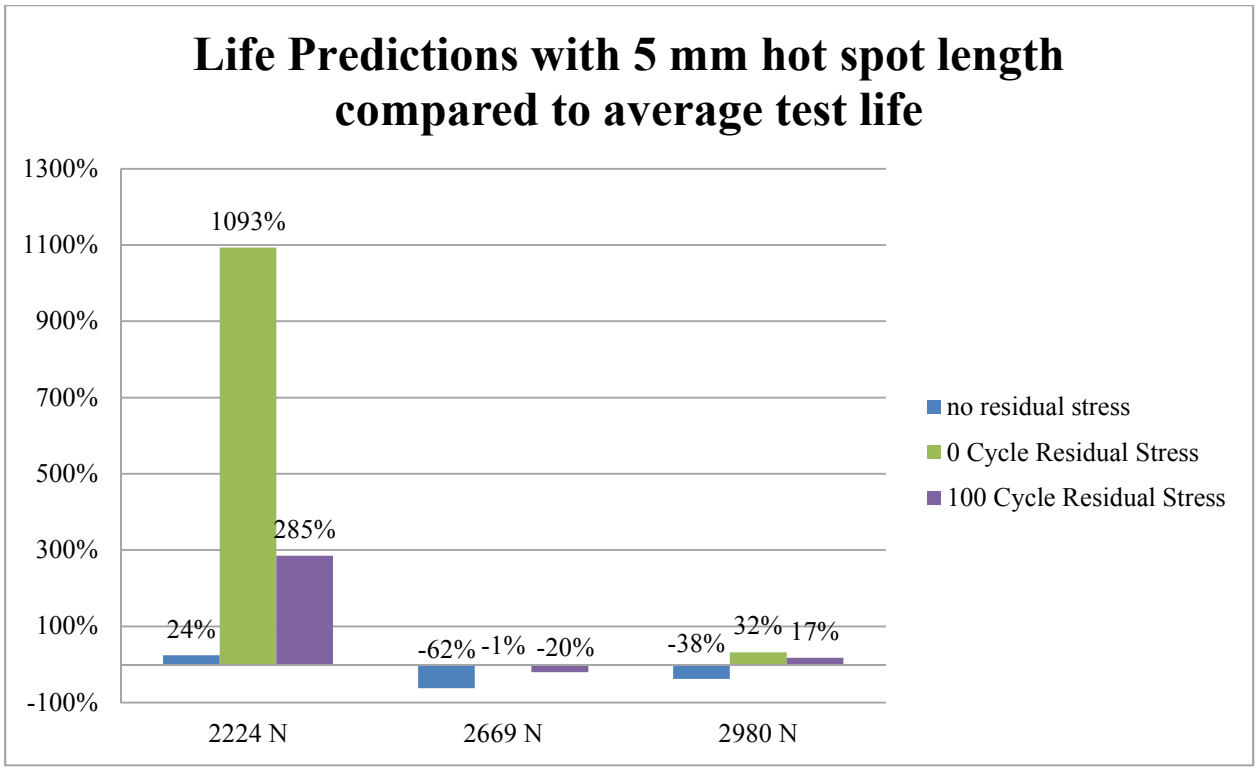

Figure 85) Graphical representation of the life prediction compared to the test life for the Kt derived for a 5 mm hot spot length.

It is clear that for the 2224 N load case the highly compressive stresses of the initial stress state provide overly conservative predictions. It is equally clear that the higher load levels were not as sensitive to the initial compressive residual stresses. To illustrate this, the cyclic stress strain response of the conditions detailed in Section 2.3.4 Elasto-plastic Stress Strain Response can be used to evaluate the stress/strain response. From the Mason-Coffin equation, Equation 12, the total damage is determined by the strain amplitude, $\frac{\Delta\varepsilon}{2}$. Even though fully reversed R = -1 loading was used, the residual stress produces a mean stress in the hysteresis loop. The mean stress can be accounted for using the Smith-Watson-Topper mean stress correction (54).

Figure 86 shows the hysteresis loop calculated using Equations 9 through 11 for the high 2980 N and low 2224 N load level both with the 5 mm hot spot length mean Kt and a residual stress of -100 MPa. When comparing the two load levels of 2980 N and 2224 N the mean stress of the hysteresis loops are very similar. The sample loaded at 2980 N having a mean stress of -24 MPa while the sample loaded at 2224 N has a mean stress of -34 MPa. The mean stress does not match the residual stress due to plasticity. When comparing the strain amplitude, $\frac{\Delta\varepsilon}{2}$, there is a large difference between the two with the 2980 N load at 2697 με and 2224 N load at 1678 με.

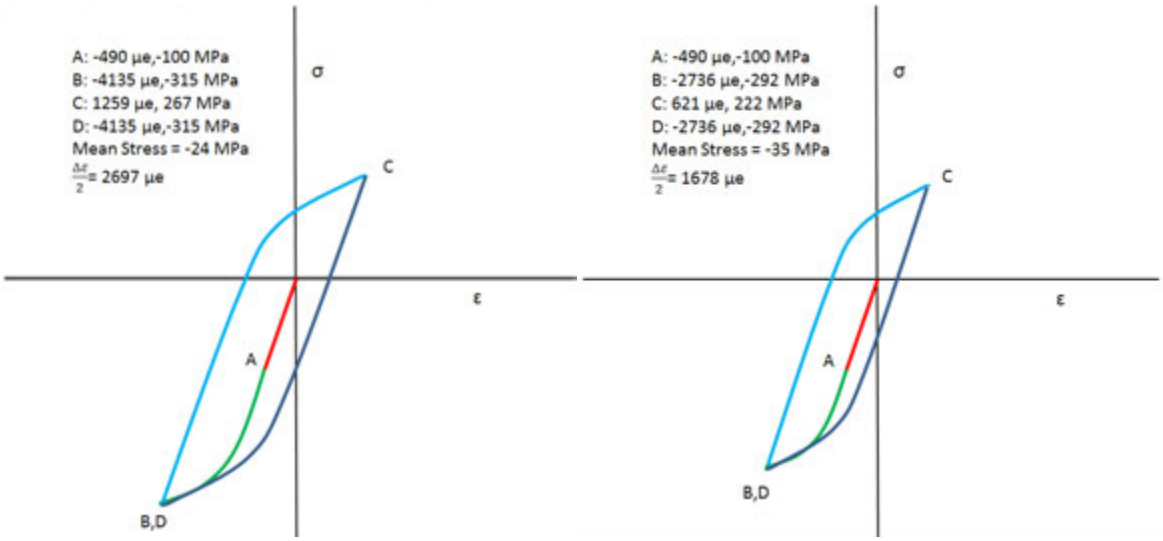

a. b.

Figure 86) Hysteresis loop showing the stress strain response for a) 2980 N load and b) 2224 N load with a -100 MPa residual stress.

To sum it up, the initial residual stress state drives the mean stress, but when plasticity is concerned the mean stress is not the same as the residual stress. The mean stress which is driven by the residual stress and loading has a large impact on the fatigue life by the nature of the

fatigue life curve. Figure 87 illustrates this point. When the strains are high, as the case in the high loading situation, the lower strain from the residual stresses does not have a big impact in the final predicted number of cycles (or reversals as shown in Figure 87). However, at the lower strain amplitudes, in the low load situation, the change sample change in the strain amplitude has a very large effect on the life prediction. This demonstrates the impact the stress has at the different loading conditions.

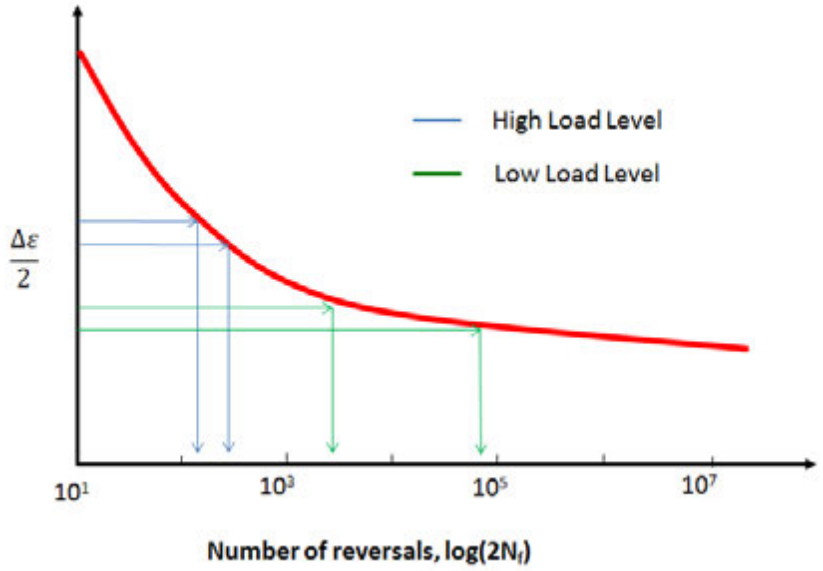

Figure 87) Sketch of the Manson Coffin curve and how slight differences in loading can cause large change in the fatigue life

Probabilistic life prediction comparison

The previous section focused on the single life prediction using the mean values for the input parameters. This section will evaluate how the ***distribution of predicted life*** matches the experimental data. The predicted distributions compared to the test life distributions are shown in Figure 75 through Figure 77. The ideal situation would be that a single set of variables could be used for the life prediction. The best life prediction should be near the test data or slightly conservative. The results will be evaluated using these criteria.

The life prediction distributions that best fit the criteria of being near the test results to slightly conservative would be the no residual stress to 100 cycle residual stress with the 50 mm hot spot Kt. The predicted distribution for the no residual stress and 100 cycle residual stress do not show much difference between the two curves. The test data matches the 100 cycle residual stress after the 50% percent probability of failure. Below the 50% probability of failure the no residual stress curve matches well.

At this low stress value the test data has significant amount of scatter. It is reasonable to believe that the scatter in this data is due to the distribution of the stress concentration at the weld toe. This load level is very sensitive to the Kt. Figure 81 shows that at a 50 mm hotspot stress the 50 % probability of failure would be 200,000 cycles and for the Kt at 5 mm hot spot it is 490,000 cycles; a difference in life of almost 2.5 times with the difference in the Kt. This demonstrates the sensitivity of the life prediction has at the lower load to Kt. This load level would be the most sensitive to the hotspot length.

It is also reasonable to believe that the crack along the length of the hotspot will not initiate at a single spot, but will initiate at multiple spots near close to the same number of cycles. At the lower load level the initiation of the multiple cracks will occur at a wider range of cycles where the crack will appear. This will results in a wider scatter in the fatigue results and possibly lower fatigue lives in the test than the predicted lives.

The 2669 N load results show that the distribution of life is predicted very well with the Kt for a 5 mm hot spot length and the “100 cycle” residual stress distribution, although the predicted life distribution overestimates the life at the lower probabilities of failure and underestimates the life at higher probabilities. It is interesting to see that the prediction made using the “0 cycle” residual stress shows a lower life than the “100 cycle” residual stress at

probabilities of failure below 22%. This is unexpected since when looking at the mean values the lower residual stress of the "0 cycle" state should have a significantly longer life. This difference is believed due to the wider residual stress distribution in the "0 cycle" samples.

The 2980 N load level is best modeled using the lower Kt of the 5 mm hot spot length and no residual stress. The test data does lie in between the no residual stress and 100 cycles residual stress life distributions predicted with the 5 mm hot spot stress. This may indicate that further relaxation of the residual stresses could occur to push the 100 cycle residual stress further to the left. The 50 mm hot spot length life prediction shows that the predictions are all conservative.

To summarize low load level of 2224 N had much shorter test lives that predicted values. It is believe that this is the case due to multiple cracks initiating along the length of the weld in the hot spot zone and appearing to be a much larger crack. The life predictions are non-conservative and larger Kt is needed to predict the lives. The 2669 N load it best modeled using the 100 cycle residual stress level and the lower Kt from the 5 mm hot spot length. This is an indication that less residual stress relaxation occurs at the lower stress level. Finally for the 2980 N load level the test data falls in between the life distribution predictions for the no residual stress state and the 100 cycle residual stress state. When predicting the fatigue life distribution for conservative results it is best to disregard the residual stress at the medium and high load levels and use the 5 mm hot spot Kt. The low load level had unexpectedly low test lives, which require higher Kt for a 50 mm hot spot length for the life predictions.

The unexpectedly low test values at the low load level shows that a better understanding of the role the Kt factor has at the lower load levels is needed for more accurate life predictions. Without this understanding the prediction will be non-conservative. At the other load levels it

appears that the redistributed residual stresses with the lower Kt level are needed. The redistribution of the residual stress as a function of the number of cycles would also increase the accuracy of the life predictions.

The wide spread in experimental fatigue data and the limited number of samples tested at the three selected load levels unfortunately limits the certainty with which one can make recommendations regarding best practice. Additional testing to provide a greatly expanded experimental set of data would provide a sounder basis for making statistical statements and would greatly help to answer the question concerning the interplay between applied load, residual stress, and Kt.

7.5 Conclusion

This chapter proposes a methodology for calculating the estimated distribution of fatigue life using the hot spot stress method, measured residual stresses, the distribution of Kt from weld measurements, and the distribution of material properties from testing. From the results the following conclusions can be drawn:

- Prediction of the median test life of the welded samples can be accomplished within the percent error of a smooth specimen test used for strain life testing.
- The distribution of the fatigue lives can be predicted using the methods presented with reasonable success.
- The predicted life distribution for the higher load levels match better when the distribution of the redistributed residual stress is used rather than the measured initial residual stress.
- The predicted life distribution for the higher load levels of 2669N and 2980N do not match well when accounting for the length of the hot spot. This is at odds with the

results for the lower 2224N load, which matches well when the initial residual stress distribution is used and the distribution of Kt that accounts for the length of the hotspot is used.

- Neglecting the residual stress and using the 5 mm hot spot Kt provided the most accurate fatigue life predictions for both the single life prediction and the prediction of the fatigue life distribution.
- Using the higher value of the 50 mm hot spot Kt with no residual stress provided less accurate, but conservative fatigue life predictions.
- Further testing would be necessary to have more confidence that the predicted distribution matches the test sample distribution.

CHAPTER 8: GENERAL CONCLUSIONS

The goal of this dissertation was to improve life predictions of welded structures by validating the use of current welding simulation predictions and developing computational methods that would address the numerous sources of variability in the input parameters used in fatigue life prediction methods. Three questions were stated which, if answered, would significantly advance efforts toward the attainment of the stated goal.

Question 1 examined "Can welding simulation provide enough accuracy in residual stress predictions to be used to replace measurement of residual stresses in fatigue life predictions of welded structures?" This was addressed using distortion measurements and residual stress measurements obtained using neutron diffraction to validate welding simulation predictions on standard T-welds. Current methods available for distortion prediction match experimental results within the sample-to-sample error in testing. The same is true of residual stress predictions. In the critical location the deviation of the predicted residual stress was with in the sample-to-sample variation. This shows that computational welding simulation can be used to predict the residual stress with the accuracy needed for fatigue life simulation.

Question 2 asked "Does cyclic loading change the residual stress state and negate the initial residual stresses used in fatigue life predictions?" Cyclic loading does redistribute the stresses within the sample. The drop is significant in the initial cycles and the stress stabilizes to a nominal value. This drop in stress is hypothesized to be due to the plasticity that occurs upon loading. Welds are particularly susceptible due to concentration of the stress at the weld toe. The results of comparing the fatigue life predictions to the test data showed that the redistributed residual stress state should be used when making fatigue life predictions.

Finally question 3 was "Can the distribution of fatigue life be predicted by accounting for the variability of the input parameters like residual stress, material strength, local weld toe geometry, and material properties?" A process was proposed in this dissertation to capture this distribution of life by accounting for the distribution of the input variables. The process was examined at three load levels and it was found that the distribution in fatigue life can be predicted with mixed results. Prediction of the life distribution at a high and medium load level showed excellent correlation to the fatigue life distribution when using the 5 mm hot spot stress Kt and no residual stress, while the predicted fatigue life distribution of the low load level predicted a non-conservative fatigue life distribution unless the higher 50 mm hot spot Kt is used. Even then the life prediction is non-conservative below a 50% probability of failure.

Future work

During this work many lessons were learned and opportunities for further research identified. Perhaps one of the most critical areas is obtaining a better understanding of the size effect of the hot spot stress length. This dissertation would indicate that there is little effect; it is believed that this topic area deserves further study. For example, the lower stress level had better life predictions using the higher Kt value from the larger hot spot stress distribution while the other load levels had higher errors when this approach was tried. This is an opportunity for further research.

The other area for further study would be to obtain a more statistically meaningful test life distribution by increasing the population of test samples. This would provide a better fatigue life distribution for subsequent comparisons.

The third area of research suggested from this work would be to use welding simulation and the welding input parameters to predict the residual stress distribution of the samples. This data, coupled with a better model for stress relaxation as a function of cyclic loading, might provide a distribution of residual stresses for model testing and verification without extensive and expensive measurements.

In conclusion, while this dissertation has provided an underlying methodology for life prediction distribution more work needs to be done to better refine the input parameter distributions investigated and the techniques employed to introduce the variability associated with them into life predictions.

BIBLIOGRAPHY

1. **El-Zein, M and Glinka, G.** *Internal Report, 2002.* s.l. : Deere and Company, 2002.

2. **Fatigue Design and Evaluation Committee .** Weld Project. *Fatigue Design and Evaluation Committee* . [Online] [Cited: 2012 1-May.] www.fatigue.org.

3. **Cary, Howard B.** *Modern Welding Technology.* Columbus : Prentice Hall, 1989.

4. **Linnert, George E.** *Welding Metallurgy.* Miami : American Welding Society, 1994.

5. **Street, J A.** *Pulsed Arc Welding.* Cambridge : Abington, 1990.

6. **Wahab, M A, Painter, M J and Davies, M H.** The prediction of temperature distribution and weld pool geometry in the gas metal arc process. *Journal of Materials Processing Technology.* 1998, Vol. 77.

7. **Albert, W A J.** Uber Treisbseile am Harz Archiv fut Mineralogie, Georgnosie. *Berhbau und Huttenkunde.* Vol. 10.

8. **Borgnakke, C and Sonntag, R E.** *Fundamentals of Thermodynamics.* Hoboken : John Wiley & Sons, 2008.

9. *On the causes of the unexpected breakage of the journals of railway axles, and on the means of preventing such accidents by observing the law of continuity in their construction.* **Rankine, W J M.** London : Institution of Civil Engineers, Minutes of Proceedings, 1842.

10. **Rankine, W J M.** On the causes of the unexpected breakage of the journals of railway axles and the mean of preventing such accidents by observing the law of continuity in their construction. *Intitution of Civil Engineering, Minutes of Proceedings.* 1842 , Vol. 2.

11. **Braithwaite, F.** On the fatigue and consequent fracture of metals. *Insitute of Civil Engineers, Minutes of Proceedings.* 1854, Vol. 13.

12. **Schultz, W.** A History of Fatigue. *Engineering Fracture Mechanics.* 1996, Vol. 54, 2.

13. **Basquin, O H.** The exponential law of endurance testss. *Annual Meeting, ASTM* . 1910 , Vol. 10.

14. *Metal Fatigue in Engineering.* **Fuchs, H O, et al., et al.** Hoboken : John Wiley & Sons, 2000.

15. **Coffin, L F.** The problem of thermal stress fatigue in austenitic steels at elevated temperatures. [book auth.] E01.01. *ASTM STP No. 165.* s.l. : ASTM, 1954.

16. *Behaviour of materials under conditions of thermal stress.* **Manson, S S.** Ann Arbor : University of Michigan Engineering Research Institute, 1953.

17. **Coffin, L F.** A study of the effects of cyclic thermal stress on a ductile metal. *Transaction of American Society of Mechanical Engineers.* 1954, Vol. 76, 931.

18. **Griffith, A A.** The phenomena of rupture and flow in solids. *Philosphical Transcations of the Royal Society.* 1920 , Vol. 221A, 163.

19. **Irwin, G.** Analysis of stresses and strains near the end of a crack traversing a plate. *Journal of Applied Mechanics.* Vol. 24.

20. **Paris, P C, Gomez, M P and Anderson, W E.** A rational analytic theory of fatigue. *The Trend in Engineering.* 1961 , Vol. 13.

21. **Palmgren, A.** Die Lebensdauer von Kugellagern. *VDI Zeitschrifft.* 1924 , Vol. 68.

22. **Miner, M A.** Cumulative damage in fatigue. *Journal of Applied Mechanics.* 1945 , Vol. 12.

23. **Goodman, J.** *Mechanics Applied to Engineering.* London : Green & Company, 1899.

24. **Smith, K N, Watson, P and Topper, T H.** A stress-strain function for the fatigue of metals. *Journal of Materials.* 1970 , Vol. 5, 4.

25. **Morrow, J.** Fatigue Design Handbook. [book auth.] J A Graham and J F Millan. Warrendale : Society of Automotive Engineers, 1968.

26. **Manson, S S and Halford, G R.** Practical implementation of the double linear damage rule and damage curve approach for treating cumulative fatigue damage. *International Journal of Fatigue.* 1981, Vol. 17, 2.

27. **Mallery, Timothy J.** CHAPTER VI.THE VERSAILLES ACCIDENT. *Catskill Archive.* [Online] Timothy J. Mallery. [Cited: 2012 3-October.] http://catskillarchive.com/rrextra/WKBKCH06.Html.

28. **Withey, P A.** Fatigue failure of the de Havilland comet I. *Engineering Failure Analysis.* 1997 , Vol. 4, 2.

29. **Kelkara, A D, Tateb, J S and Bolicka, R.** Structural integrity of aerospace textile composites under fatigue loading. *Materials Science and Engineering: B.* 2006, Vol. 132, 1-2.

30. **ASTM International.** Standard Terminmology Relating to Fatigue and Fracture Testing. *ASTM E1823-11.* West Conshohoken : s.n., 2011.

31. **Dieter, G.** *Mechanical Metallurgy.* New York : McGraw Hill, 1986.

32. **Forsyth, P J E.** *The Physical Basis of Metal Fatigue.* New York : Elsevier, 1969.

33. **Olivier, R and Ritter, D.** *Catalogue of S-N curves of welded joints in steel.* Dusseldorf : Welding Research International, 1979. Vol 1-5 Report number 56.

34. **Hobbacher, A.** *Recomentation for fatigue strength of welded components.* Cambridge : Abington Publishers, 1996.

35. *Working Group Reports.* **International Institute of Welding Comission XIII.** Denver : s.n., 2012.

36. **Fricke, Wolfgang.** Fatigue analysis of welded joints: state of development. *Marine Structures.* 2003, Vol. 16.

37. **Lawrence, F V.** *Estimating the fatigue crack initiation life in welds.* Philidephia : ASTM, 1978. STP 648.

38. **Radaj, D.** *Design and analysis of fatigue-resistant welded structures.* Cambridge : Abington Publishers, 1990.

39. **Kottgen, V B, Olivier, R and Seeger, T.** *Fatigue analysis of welded connections based on local stresses.* s.l. : International Institute of Welding, 1991. XIII-1408-91.

40. **Verreman, Y and Nie, B.** Early development of fatigue cracking at manual fillet welds. *Fatigue and Fracture of Engineering Materials and Structures.* 1996, Vol. 19.

41. **Atzori, B, Lazzarin, P and Tovo, R.** From a local stress approach to fracture mechanics: a comprehensive evaluation of the fatigue strength of welded joints. *Fatigue and Fracture of Engineering Materials and Structures.* 1999 , Vol. 22.

42. **Paris, P C and Erdogan, F.** A Critical Analysis of Crack Propagation Laws. *The Journal of Basic Engineering - Trans.ASME.* 1963.

43. **Barsom, J M and Rolfe, S T.** *Fracture and Fatigue Control in Structures.* West Conshohocken : ASTM, 1999.

44. **Glinka, G.** *Fatigue and Fracture Short Course.* [Power Point] St. Petersburg ,ON : SAFFD, 2006 .

45. **Bathe, Klaus-Jurgen.** *Finite Element Procedure.* Englewood Cliffs : Prentice Hall, 1996.

46. **Dong, P.** A structural stress definition and numerical implementation for fatigue analysis of welded joints. *International Journal of Fatigue.* 2001 , Vol. 23.

47. **Chattopadhyay, A.** *The GR3 Method for the Stress Analysis of Weldments.* Waterloo : University of Waterloo, 2009.

48. **Monahan, C.C.** *Early Fatigue Cracks Growth at Welds.* Southampton : Computational Mechanics Publications, 1995.

49. **Brennana, F P, Peletiesa, P and Hellierb, A K.** Predicting weldtoestressconcentration factors for T and skewed T-joint plate connections. *International Journal of Fatigue.* 2000 , Vol. 22, 7.

50. *Stress Concentration in Tubular Joints.* **Kuang, J G, Potvin, A B and Leick, R D.** Houston : Offshore Technology Conference, 1975.

51. **Woghirena, C O and Brennanb, F P.** Weld toe stress concentrations in multi-planar stiffened tubular KK joints. *International Journal of Fatigue.* 2009 , Vol. 31, 1.

52. **Iida, K and Uemura, T.** *Stress Concentration Factor Formulas Widely used in Japan, Document IIW XIII-1530-94.* s.l. : The International Welding, 1994.

53. **Neuber, H.** Theory of stress concentration for shear strained prismatic bodies with arbitrary non-linear stress strain law. *Journal of Applied Mechanics.* 1961 , Vol. 26, 4.

54. **Bannantine, Julie, Comer, Jess and Handrock, James.** *Fundamentals of Metal Fatigue Analysis.* Englewood Cliffs : Prentice Hall, Inc., 1990.

55. **Ramberg, W and Osgood, W R.** *Description of stress-strain curves by three parameters.* Washington DC : National Advisory Committee For Aeronautics, 1943.

56. *Standard Practice for Strain-Controlled Fatigue Testing.* **Committee E08.05.** West Conshohocken : ASTM International , 2004. E606-04e1.

57. **Seeger and Boller.** *Material Data for Cyclic Loading Volume 42A.* s.l. : Elesvier Science, 1987.

58. **Withers, P J and Bhadesh, H K D H.** Residual stress Part 2- Nature and origins. *Materials Science and Technology.* 2007 , Vol. 17.

59. **Withers, P J and Bhadeshia, H K D H.** Residual stress Part 1- Measurement techniques. *Materials Science and Technology.* 2001 , Vol. 17.

60. **Downing, N.** *Mechanical Behavior of Materials.* Englewood Cliffs : Prentice Hall, 1993.

61. **Tsai, C L and Kim, D S.** Understanding residual stress distortion in welds: an overview. [book auth.] Z Feng. *Processes and mechanism of welding residual stress and distortions.* Cambridge : Woodhead, 2005.

62. **Pilipenko, A.** *Computer simulation of residual stress and distortion of thick plated in multielectrode submerged arc welding.* Lulea : Lulea University of Technology, 2001.

63. **Park, M J, et al., et al.** ‘Residual stress measurement on welded specimen by neutron diffraction. *Journal of Material Processing Technology.* 2004 , Vols. 155-156.

64. **Tsai, C L and Kim, D S.** Understanding residual stress and distortion in welds: overview. [book auth.] Z Feng. *Process and mechanisms of welding residual stress and distortion.* Cambridge : Woodhead, 2005.

65. **Goldak, J A and Akhlaghi, M.** *Computational Welding Mechanics.* New York : Springer, 2005.

66. **Lindgren, L E.** Finite Element Modeling and Simulation of Welding Part 1: Incresed Complexity. *Journal of Thermal Stresses.* 2001 , Vol. 24.

67. **Wahab, M A, Painter, M J and Davies, M H.** The prediction of temperature distribution and weld pool geometry in the gas metal arc process. *Journal of Materials Processing Technology.* 1998 , Vol. 77.

68. **Grong, O.** *Metallurgical Modeling of Welding.* Cambridge : Institute of Materials, 1997.

69. **Goldak, J.** *Weld Analysis: Best Practices.* 2007.

70. **Inoue, T.** Thermal-metallurgial-mechanical interactions during welding. [book auth.] Zhili Feng. *Processes and mechanisms of welding residual stresses and distortion.* Cambridge : Woodhead, 2005.

71. **Schmidt, , T, Tyson, J and Galanulis, K.** Full-Field Dynamic Displacement and Strain Measurement.

72. **Bailey, W B.** *Design of a Detector Array for Neutron Residual Stress Measurement at Oak Ridge National Laboratory’s High Flux Isotope Reactor.* Columbia : MS Thesis - University of South Carolina, 2005.

73. **Tang, F and Hubbard, C R.** *Calibration of NRSF2 Instrument at HFIR* . s.l. : ORNL/TM-2006/541, 2006.

74. **An, K and Hubbard, C R.** *User Manual of NRSF2-VIEW and NRSF2-CALIBRATE.* s.l. : ORNL/TM-2005/530, 2006.

75. **An, K, Wright, M C and Hubbard, C R.** *User Manual of NRSF2-MAP.* s.l. : ORNL/TM-2005/531, 2006.

76. **James, J A, et al., et al.** A virtual laboratory for neutron and synchrotron strain scanning. *Physica B.* 2004 , Vol. 350, E743-6.

77. **James, J A and Edwards, L.** Application of robot kinematics methods to the simulation and control of neutron beam line positioning systems. *Nuclear Instruments and Methods in Physics Research A.* 2007 , 571.

78. **Bunn, J, Schmidlin, J and Hubbard, C R.** *Residual Stress Sample Alignment Laboratory Guideline.* s.l. : ORNL/TM-2008/159, 2008.

79. *Analytical and experimental validation of residual stresses using state-of-the-art techniques.* **Johnson, Eric, et al., et al.** Calaway Gardens : ASM International, 2008.

80. *Predicting Distortion and Residual stress in Complex Welded Structures by Designers.* **Goldak , J, et al., et al.** Callaway Gardens Resort : ASM International.

81. **Watt, D, et al., et al.** Modeling Microstructural Development in Weld Heat-Affected Zones. *Acta Met.* 1988, Vol. 36.

82. **Henwood, C, et al., et al.** Coupled Transient Heat Transfer-Microstructure Weld Computations. *Acta Met.* 1988, Vol. 36.

83. **Goyal, R, et al., et al.** *A Model Equation for Cenvection Coefficents for Thermal Analysis of Welded Structures.* Metals Park : ASM International, 2009.

84. **Cullity, B D.** *Elements of X-Ray Diffraction, 2nd ed.* Reading : Addison-Wesley, 1978.

85. **Noyan, I C and Cohen, J B.** *Residual Stress, Measurement by Diffraction and Interpretation.* New York : Springer-Verlag, 1987.

86. **Goldak, John, et al., et al.** *Validation of VrHeatTreat Software.* s.l. : http://www.goldaktec.com/pdf/ValidationHeatTreat.pdf, 2007.

87. **Wick A, A, Schulze , V and Vohringer, O.** Effects of warm peening on fatigue life and relaxation behavior of residual stresses in AISI 4140 steel. *Materials Science and Engineering A.* 2000, Vol. 293.

88. **Torres, M and Voorwald, H.** An evaluation of shot peening, residual stress and stress relaxation on fatigue life of 4340 steel. *International Journal of Fatigue.* 2002, Vol. 24.

89. **Zhuanga, W Z and Halford, G R.** Investigation of residual stress relaxation under cyclic load. *International Journal of Fatigue.* 2001, Vol. 23.

90. **Han, S, Lee, T and Shin, B.** Residual stress relaxation of welded steel components under cyclic load. *Steel research.* 2002, Vol. 9, 73.

91. **Lawrence , F V and Yung, J Y.** *Estimating the effects of residual stress on the fatigue life of notched components.* s.l. : Fracture Control Program - University of Illinois, 1986. Report no 124.

92. **Qian, Zhongyuan, Chumbley, Scott and Johnson, Eric.** The Residual Stress Relaxation Behavior of Weldments During Cyclic Loading. *Analysis of residual stress relaxation behaviors.* 2012 .

93. **Hertzberg, Richard W.** *Deformation and Fracture Mechanics of Engineering Materials.* New York : John Wiley and Sons, 1976.

94. **El-Zein, M, Goyal, R and Glinka, G.** *METHOD FOR THE PREDICTION OF FATIGUE LIFE FOR WELDED STRUCTURES. 20120259593* USA, April 7, 2011. 703/1.

95. **Little, R E and Ekvall, J C.** *Statistical Analysis of Fatigue Data: STP 744.* Philadelphia : ASTM, 1981.

ACKNOWLEDGEMENTS

I would like to first thank Dr. Scott Chumbley who has stuck with me during this process. He never gave up on me. He has been a good friend and mentor over the years. Also I would like to thank my manager, Dr. Mohamad El-Zein, for his encouragement and allowing me the flexibility to complete this while still working. This would not have been possible without his patience. Thanks to Alice Popescu-Gatlan who provided the final bit of motivation for me to get this completed. Dr. Gregory Glinka who taught me most everything I know about fatigue and Dr. John Goldak for helping me out with the welding simulation. Thanks to Rakesh Goyal and Dr. Kuen Tat Teh who help me out with all my modeling needs. My thanks go to Dr. Tom Watkins and Dr. Amit Shyam from Oak Ridge National Laboratory who stayed late nights scattering neutrons with me.

Most of all I would like to thank my wife Kim Johnson for her endurance to the end. She put up with many evenings and weekends away. I love you honey and could not have done this without your loving support.

Research at the 2nd Generation Neutron Residual Stress Mapping Facility at the High Flux Isotope Reactor was partially sponsored by the U.S. Department of Energy, Office of Energy Efficiency and Renewable Energy, Vehicle Technologies Program, through the Oak Ridge National Laboratory's High Temperature Materials Laboratory User Program and by the Scientific User Facilities Division, Office of Basic Energy Sciences, U.S. Department of Energy.